2017

Synthetic exploration of halide perovskites and germanium semiconductors

Long Men
Iowa State University

Synthetic exploration of halide perovskites and germanium semiconductors

by

Long Men

A dissertation submitted to the graduate faculty

in partial fulfillment of the requirements for the degree of

DOCTOR OF PHILOSOPHY

Major: Chemistry

Program of Study Committee:
Javier Vela, Major Professor
Emily Smith
Jacob Petrich
Gordon Miller
Wenyu Huang

The student author, whose presentation of the scholarship herein was approved by the program of study committee, is solely responsible for the content of this dissertation. The Graduate College will ensure this dissertation is globally accessible and will not permit alterations after a degree is conferred.

Iowa State University

Ames, Iowa

2018

TABLE OF CONTENTS

Page

ACKNOWLEDGMENTS

First, I would like to thank my major advisor, Dr. Javier Vela, for his encouragements, supports and instructions throughout my PhD work. I am learning how to be a critical researcher with his education. I would also like to thank Drs. Emily Smith and Jacob Petrich for collaborations in the 'Chemical Analysis of Nanodomains' project. I would also like to thank my committee members, Drs. Gordon Miller and Wenyu Huang, for their support.

Next, I would like to thank my Mom and my grandma, who have been so supportive and understanding throughout these years I am abroad. I wish I could be around to take care of you when you need me.

In addition, I need to thank the Vela group, past and present. Individually, I want to especially thank Himashi Andaraarachchi for being such a great friend through the years. I want to thank Dr. Yijun Guo for training me to make core/shell nanocrystals and Dr. Feng Zhu for instructions in the synthesis of perovskite nanocrystals. I want to thank Bryan Rosales and Miles White (Arthur) for valuable discussions and comments on my research projects. I also need to thank many collaborators outside of the Vela group. Namely, I would like to thank Dr. Ujjal Bhattacharjee, Daniel Freppon, Brett Boote and many more for many collaborations in Nanodomain team. I also would like to thank Dr. Liang Luo, Dr. Jigang Wang and Zhaoyu Liu for the collaborations in perovskite terahertz measurements. I also would like to thank staff scientists in Ames Laboratory and chemical instrument facilities for their professional training on advanced chemical analysis instruments. Especially, I want to thank Drs. Lin Zhou and Kewei Sun for TEM training.

Finally, I would also like to thank my friends and especially basketball buddies that accompany me during these years. I also need to thank some very special friends throughout theses past four years, Qiaochu Zhu, Zhiyuan Qi and many more.

ABSTRACT

Halide perovskites and germanium semiconductors are promising materials for many optical applications such as solar cells and LEDs due to their unique photophysical properties. Compositional substitution and dimensional manipulation can enhance physical or chemical properties of perovskite and germanium semiconductors which in turn promotes their performance in optoelectronic devices. In this thesis, we report the synthetic exploration of composition-control and dimensionality-control of organometal halide perovskite crystals by tuning halide-incorporation and exploiting bulky alkylammonium cations as capping ligands. We also demonstrate a systematic synthesis of all the series of mixed halide perovskite polycrystals and their low dimensional analogues. By optimizing synthetic conditions, we are able to inhibit the appearance of a reversible photoinduced PL peak derived from surface traps.

We also synthesize lead-free perovskites for the environmental concerns. Lead is a heavy metal element and its potential toxicity raises concerns for environmental compatibility. To address this problem, we developed a synthetic route to antimony perovskites and germanium perovskites. Surface-bound $(CH_3)_3Sb_2I_9$ layers restrict the growth of $CH_3NH_3PbI_3$, resulting in $CH_3NH_3PbI_3$ nanocrystals. Compared to the bulk perovskites, the antimony-capped nanocrystals show stronger photoluminescence. With a direct bandgap of 1.6 eV and a corner-sharing octahedral network crystal structure that are comparable to $CH_3NH_3PbI_3$, $CsGeI_3$ is potentially promising for photovoltaic applications. To manipulate the optoelectronic properties, we doped high-spin, divalent manganese ions (Mn^{2+}) into the octahedral Ge^{2+} sites of $CsGeI_3$. Electron paramagnetic resonance (EPR) helps us better understand the local ion environment and composition of both $CsGeI_3$ and its doped analogue ($CsGe_{1-x}Mn_xI_3$). Our results expand the lead-free halide perovskite

family and set the stage for their application beyond photovoltaics to spintronics and magnetic data storage.

Finally, we fabricated and characterized $Ge_{1-x}Sn_x$ alloy nanocrystals and $Ge_{1-x}Sn_x$ core/shell nanocrystals. Germanium has an indirect bandgap of 0.66 eV, which is too narrow for ideal solar cell light harvester materials and limits their absorption efficiency. By tin incorporation and quantum confinement effect, we could enhance their efficiency of solar absorption and in turn their quantum yield. We synthesized $Ge_{1-x}Sn_x$ and $Ge_{1-x}Sn_x$/CdS core/shells in solution phase. Inclusion of tin is confirmed by X-ray diffraction and Raman peak shift. Tin alone does not result in enhanced photoluminescence intensity, however, adding an epitaxial CdS shell onto the $Ge_{1-x}Sn_x$ nanocrystals does enhance the photoluminescence up to 15× over Ge/CdS nanocrystals with a pure Ge core. More effective passivation of surface defects—and a consequent decrease in surface oxidation—by the CdS shell as a result of improved epitaxy (smaller lattice mismatch) is the most likely explanation for the increased photoluminescence observed for the $Ge_{1-x}Sn_x$/CdS materials. With enhanced photoluminescence in the near-infrared, $Ge_{1-x}Sn_x$ core/shell nanocrystals might be useful alternatives to other materials for energy capture and conversion applications and as imaging probes.

CHAPTER 1. INTRODUCTION

General Introduction

With increasing need for energy in modern society, humans are always in the pursuit for clean and sustainable energy. Solar energy is one of the most important clean energy sources. Solar energy is basically unlimited: the total solar energy absorbed by Earth in one hour is more than the energy used by humans in one year.[1] If humans can utilize solar energy efficiently, oil crisis will be relieved. Solar energy is also a clean energy. Unlike fossil fuel, when solar energy is converted to electricity or chemical energy, no pollution or greenhouse gas will be generated. Compared to other clean energy sources such as nuclear energy, solar energy is safer and easier to obtain. People can easily install a solar panel on their roofs and enjoy the heat and electricity powered by solar light.

Currently the most common material for solar panels is high purity silicon. The best record for single junction silicon solar cells is 25%.[2] Efforts have been made to push the efficiency even better for decades, but there is a theoretical limit for silicon solar cells, which is 32%. This efficiency limit is known as Shockley–Queisser limit (Figure 1).[3] When searching for the best photovoltaic materials, we are looking for the semiconductors with small bandgap that can allow the materials to absorb a large portion of solar light. But a small bandgap also brings small output voltage that limits the power of the solar cells. Due to these two opposite effects, the best photovoltaic material should have a bandgap around 1.34 eV. The bandgap of silicon is 1.1 eV which is relatively smaller than the ideal bandgap. Also, due to the indirect nature of silicon's bandgap, silicon has a relatively low absorption coefficient, which limits their absorption efficiency for sunlight and thus constrains the solar cell efficiency. Another factor that limits silicon solar cells is the purity of silicon. Impurity can lower the efficiency, so silicon single crystal is preferred in solar panels due to their high purity. Even though the energy harvesting process is clean, the fabrication

process of high purity silicon costs lots of energy and generates toxic gases that pollute our environment. To address the problems and limits silicon solar cells have, researchers are seeking new materials to substitute silicon as sunlight harvesting materials.

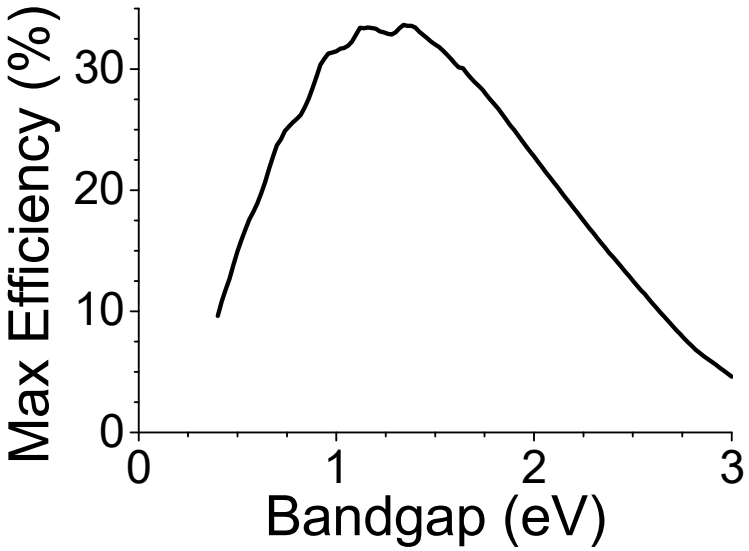

Figure 1. The Shockley-Queisser limit for the efficiency of a solar cell, without concentration of solar radiation.[3]

Perovskites, named after a Russian mineralogist Lev Perovski, have garnered great interest for their outstanding performance in solar cells. Perovskites have a general composition of ABX_3 such as $CaTiO_3$. For solar cells halide perovskites, especially methylammonium lead iodide perovskites $CH_3NH_3PbI_3$ (Figure 2),[4] are widely used due to their suitable bandgap, long carrier diffusion length and defect tolerant properties.[5-8] The efficiency for perovskite solar cells was only 3.8% in 2009,[9] but it only took 8 years to push the efficiency up to 22% (Figure 3).[10] Compared to silicon semiconductors, perovskites with a direct bandgap of 1.5 eV are more suitable as photovoltaic materials. Even compared to other newly emerging light harvesting materials, such as dye sensitized solar cells or organic photovoltaic materials, perovskite solar cells also demonstrate unprecedented rate of progress in power conversion efficiency.

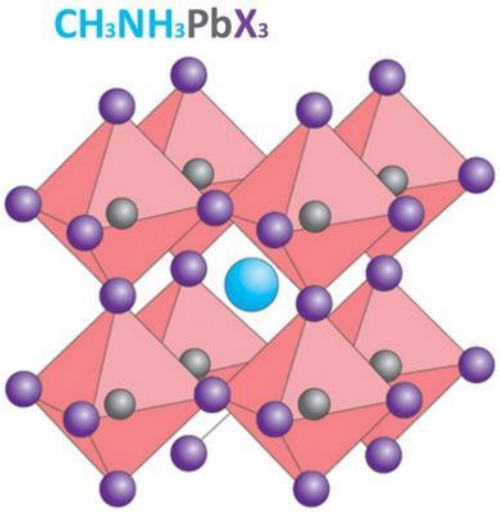

Figure 2. perovskite crystal structure where $CH_3NH_3^+$ cation occupies the center of the unit cells, $[PbI_6]^{4-}$ forms octahedra and occupies the corners of the unit cells.[4]

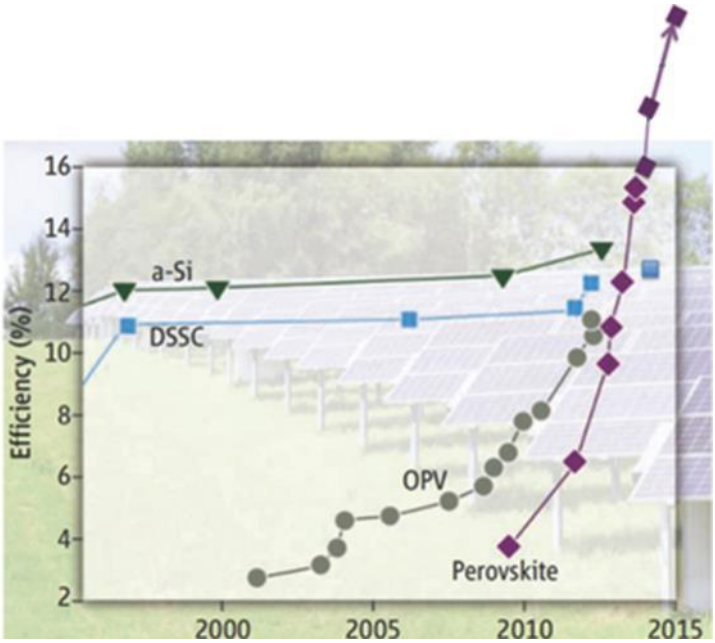

Figure 3. Illustration of the rapid increase in perovskite cell efficiencies. The increase achieved in the past four years is particularly notable. The cells have already achieved documented efficiencies >20%, which represents an unprecedented rate of progress compared to any other solar technology.[10]

Not only can perovskites be used in solar cells, they also show great potential in light-emitting devices due to their high quantum yields.[11-16] Due to the versatility of their

composition, which means a variety of metal/organic cations and halide anions can form perovskite structure, their emission energy can actually be tuned by composition and the photoluminescence spectra can cover the whole visible light region. A detailed study on composition-tunable perovskites is discussed in Chapter 2. Recently $CsPbX_3$ (X = Cl, Br and I) nanocrystals have been synthesized and their photoluminescence properties are even better than their organic analogues.[17] With high quantum yields, narrow emission line-widths and long PL lifetime, their application in LED, laser generators and the next generation colorful display will be promising.

One thing that may limit perovskite solar cells from commercialization is lead element (Pb) in perovskites. The element lead is a toxic, heavy metal that attacks the nervous and reproductive systems in humans and also raises concerns for environmental compatibility.[18-20] To address this problem, we performed the synthesis and characterization on antimony-based and germanium-based perovskites, which are discussed in Chapter 3 and 4.

Another light harvesting material with good potential for use solar cells is germanium. Even though germanium has an indirect bandgap like silicon, it is reported the indirect bandgap can be converted into direct bandgap by strain or doping (Figure 4).[21-27] With a converted direct bandgap, germanium will have a higher absorption coefficient and be more promising as an alternative for silicon solar cells. In Chapter 5, we discuss the synthesis and characterization of doping Sn into Ge nanocrystals and coat the $Ge_{1-x}Sn_x$ cores with CdS shells. Due to the lattice mismatch between $Ge_{1-x}Sn_x$ and CdS, CdS should exert a tensile strain on Ge lattice and might convert the indirect bandgap of $Ge_{1-x}Sn_x$ to direct bandgap. Our group previously reported Ge/CdS core/shell nanocrystals have a much better PL intensity than the bare Ge.[28] Here, we extend our synthetic exploration to $Ge_{1-x}Sn_x$ /CdS and study how tin incorporation may affect optical properties of Ge nanocrystals.

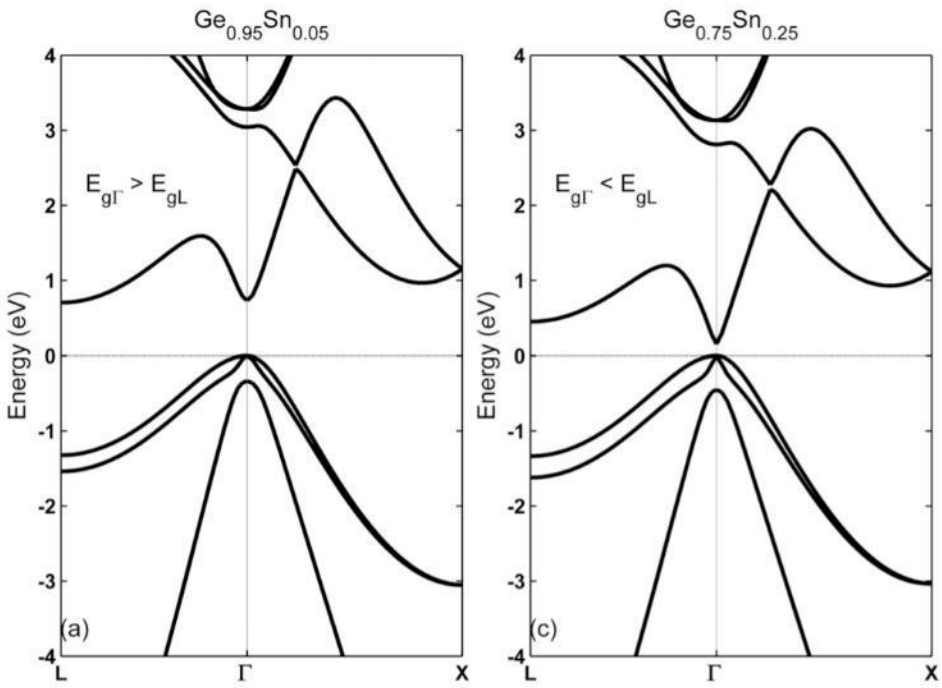

Figure 4. Calculated band structure for GeSn with 5% Sn and 25% Sn.[23]

Thesis Organization

This thesis consists of two parts. The first part discusses the synthesis of halide perovskites, including lead perovskites in Chapter 2, antimony perovskites in Chapter 3 and germanium perovskites in Chapter 4. Chapter 5 is the second part where we investigated $Ge_{1-x}Sn_x$ /CdS core/shell nanocrystals and their enhanced photoluminescence.

Chapter 2 discusses the systematic synthesis of mixed halide perovskites and their abnormal photoluminescence behavior during illumination. In Chapter 3 we report antimony perovskites as capping agents for lead perovskites. In Chapter 4 we describe the soft chemistry, dimensionality control of germanium perovskites and manganese incorporation in germanium perovskites. Chapter 5 is dedicated to the synthesis of $Ge_{1-x}Sn_x$ /CdS core/shell heterostructures and their enhanced photoluminescence properties. This was done in collaboration with Drs. Emily Smith and Jacob Petrich and their group in Iowa State University.

References

1. Morton, O. Solar Energy: A New Day Dawning? Silicon Valley Sunrise. *Nature* **2016**, *443*, 19–22.

2. National Renewable Energy Laboratory. Best Research-Cell Efficiencies Chart. https://www.nrel.gov/pv/assets/images/efficiency_chart.jpg (accessed on July 19, 2017)

3. Shockley, W.; Queisser, H.J. Detailed Balance Limit of Efficiency of P-N Junction Solar Cells. *J. Appl. Phys.* **1961**, *32*, 510–519.

4. Green, M. A.; Ho-Baillie, A.; Snaith, H. J. The Emergence of Perovskite Solar Cells. *Nature Photon.* **2014,** *8*, 506–514.

5. Zhou, H.; Chen, Q.; Li, G.; Luo, S.; Song, T.-b.; Duan, H.-S.; Hong, Z.; You, J.; Liu, Y.; Yang, Y. Interface Engineering of Highly Efficient Perovskite Solar Cells. *Science* **2014**, *345*, 542–546.

6. Shi, D.; Adinolfi, V.; Comin, R.; Yuan, M.; Alarousu, E.; Buin, A.; Chen, Y.; Hoogland, S.; Rothenberger, A.; Katsiev, K.; Losovyj, Y.; Zhang, X.; Dowben, P. A.; Mohammed, O. F.; Sargent, E. H.; Bakr, O. M. Low Trap-state Density and Long Carrier Diffusion in Organolead Trihalide Perovskite Single Crystals. *Science* **2015**, *347*, 519–522.

7. Kazim, S.; Nazeeruddin, M. K.; Grätzel, M.; Ahmad, S. Perovskite as Light Harvester: A Game Changer in Photovoltaics. *Angew. Chem. Int. Ed.* **2014**, *53*, 2812–2824.

8. Dong, Q.; Fang, Y.; Shao, Y.; Mulligan, P.; Qiu, J.; Cao, L.; Huang, J. Electron-Hole Diffusion Lengths > 175 μm in Solution-Grown $CH_3NH_3PbI_3$ Single Crystals. *Science* **2015,** *347*, 967–970.

9. Kojima, A.; Teshima, K.; Shirai, Y.; Miyasaka, T. Organometal Halide Perovskites as Visible-Light Sensitizers for Photovoltaic Cells. *J. Am. Chem. Soc.* **2009**, *131*, 6050–6051.

10. Berry, J.; Buonassisi, T.; Egger, D. A.; Hodes, G.; Kronik, L.; Loo, Y. L.; Lubomirsky, I.; Marder, S. R.; Mastai, Y.; Miller, J. S.; Mitzi, D. B. Hybrid Organic–Inorganic Perovskites (HOIPs): Opportunities and Challenges. *Adv. Mater.* **2015**, *27*, 5102–5112.

11. Deschler, F.; Price, M.; Pathak, S.; Klintberg, L. E.; Jarausch, D.-D.; Higler, R.; Hüttner, S.; Leijtens, T.; Stranks, S. D.; Snaith, H. J.; Atatüre, M.; Phillips, R. T.; Friend, R. H. High Photoluminescence Efficiency and Optically Pumped Lasing in Solution-Processed Mixed Halide Perovskite Semiconductors. *J. Phys. Chem. Lett.* **2014,** *5*, 1421–1426.

12. Schmidt, L. C.; Pertegás, A.; González-Carrero, S.; Malinkiewicz, O.; Agouram, S.; Mínguez Espallargas, G.; Bolink, H. J.; Galian, R. E.; Pérez-Prieto, J. Nontemplate Synthesis of $CH_3NH_3PbBr_3$ Perovskite Nanoparticles. *J. Am. Chem. Soc.* **2014,** *136*, 850–853.

13. Tan, Z.-K.; Moghaddam, R. S.; Lai, M. L.; Docampo, P.; Higler, R.; Deschler, F.; Price, M.; Sadhanala, A.; Pazos, L. M.; Credgington, D.; Hanusch, F.; Bein, T.; Snaith, H. J.; Friend, R. H. Bright light-Emitting Diodes Based on Organometal Halide Perovskite. *Nat. Nanotechnol.* **2014,** *9*, 687–692.

14. Zhang, F.; Zhong, H.; Chen, C.; Wu, X.-g.; Hu, X.; Huang, H.; Han, J.; Zou, B.; Dong, Y. Brightly Luminescent and Color-Tunable Colloidal $CH_3NH_3PbX_3$ (X = Br, I, Cl) Quantum Dots: Potential Alternatives for Display Technology. *ACS Nano* **2015,** *9*, 4533–4542.

15. Sichert, J. A.; Tong, Y.; Mutz, N.; Vollmer, M.; Fischer, S.; Milowska, K. Z.; García Cortadella, R.; Nickel, B.; Cardenas-Daw, C.; Stolarczyk, J. K.; Urban, A. S.; Feldmann, J. Quantum Size Effect in Organometal Halide Perovskite Nanoplatelets. *Nano Lett.* **2015,** *15*, 6521–6527.

16. Pathak, S.; Sakai, N.; Wisnivesky Rocca Rivarola, F.; Stranks, S. D.; Liu, J.; Eperon, G.; Ducati, C.; Wojciechowski, K.; Griffiths, J. T.; Haghighirad, A. A. Perovskite Crystals for Tuneable White Light Emission. *Chem. Mater.*, **2015**, *27*, 8066–8075.

17. Protesescu, L.; Yakunin, S.; Bodnarchuk, M. I.; Krieg, F.; Caputo, R.; Hendon, C. H.; Yang, R. X.; Walsh, A.; Kovalenko, M. V. Nanocrystals of Cesium Lead Halide Perovskites ($CsPbX_3$, X= Cl, Br, and I): Novel Optoelectronic Materials Showing Bright Emission with Wide Color Gamut. *Nano Lett.* **2015**, *15*, 3692–3696.

18. Gidlow, D. A. Lead Toxicity. *Occup. Med.* **2004**, *52*, 76–81.

19. Babayigit, A; Ethirajan, A.; Muller, M.; Conings, B. Toxicity of Organometal Halide Perovskite Solar Cells. *Nat. Mater*. **2016**, *15*, 247–251.

20. Serrano-Lujan, L.; Espinosa, N.; Larsen-Olsen, T. T.; Abad, J.; Urbina, A.; Krebs, F. C. Tin- and Lead-Based Perovskite Solar Cells under Scrutiny: An Environmental Perspective. *Adv. Energy Mater.* **2015**, *5*, 1501119-1–1501119-5.

21. Esteves, R. J. A.; Ho, M. Q.; Arachchige, I. U., Nanocrystalline Group IV Alloy Semiconductors: Synthesis and Characterization of $Ge_{1-x}Sn_x$ Quantum Dots for Tunable Bandgaps. *Chem. Mater.* **2015,** 27, 1559–1568.

22. Cheng, R.; Wang, W.; Gong, X.; Sun, L.; Guo, P.; Hu, H.; Shen, Z.; Han, G.; Yeo, Y.-C., Relaxed and Strained Patterned Germanium-Tin Structures: A Raman Scattering Study. *J. Solid State Sci.* **2013,** 2, 138–145.

23. Gupta, S.; Magyari-Köpe, B.; Nishi, Y.; Saraswat, K. C., Achieving Direct Band Gap in Germanium Through Integration of Sn Alloying and External Strain. *J. Appl. Phys.* **2013,** 113, 073707-1–073707-7.

24. Lin, H.; Chen, R.; Huo, Y.; Kamins, T. I.; Harris, J. S., Raman Study of Strained $Ge_{1-x}Sn_x$ Alloys. *Appl. Phys. Lett.* **2011,** 98, 261917-1–261917-3.

25. Gallagher, J. D.; Senaratne, C. L.; Kouvetakis, J.; Menendez, J., Compositional Dependence of the Bowing Parameter for the Direct and Indirect Band Gaps in $Ge_{1-y}Sn_y$ Alloys. *Appl. Phys. Lett.* **2014,** 105, 142102-1–142102-5.

26. Senaratne, C. L.; Gallagher, J. D.; Xu, C.; Sims, P.; Menendez, J.; Kouvetakis, J., Doping of Direct Gap $Ge_{1-y}Sn_y$ Alloys to Attain Electroluminescence and Enhanced Photoluminescence. *ECS Trans.* **2015,** 69, 157–164.

27. Stange, D.; Wirths, S.; Von Den Driesch, N.; Mussler, G.; Stoica, T.; Ikonic, Z.; Hartmann, J.; Mantl, S.; Grützmacher, D.; Buca, D., Optical Transitions in Direct-Bandgap $Ge_{1-x}Sn_x$ Alloys. *ACS Photonics* **2015,** 2, 1539–1545.

28. Guo, Y.; Rowland, C. E.; Schaller, R. D.; Vela, J., Near-Infrared Photoluminescence Enhancement in Ge/CdS and Ge/ZnS Core/Shell Nanocrystals: Utilizing IV/II-VI Semiconductor Epitaxy. *ACS Nano* **2014,** 8, 8334–8343.

CHAPTER 2. MIXED HALIDE ORGANOLEAD PEROVSKITES: DIMENSIONALITY CONTROL AND ROLE OF EXCESS PRECURSOR ON PHOTOLUMINESCENCE STABILITY

Long Men, Daniel J. Freppon, Ujjal Bhattacharjee, Feng Zhu, Bryan A. Rosales, Jacob W. Petrich, Emily A. Smith, Javier Vela

Abstract

Organometal halide perovskites of general composition $CH_3NH_3PbX_3$ (X = I, Br, Cl) have drawn great attention as photovoltaic materials as well as fluorophores due to their low cost and unique photophysical properties. Compositional substitution and dimensional manipulation can enhance the stability of perovskite crystals against moisture, heat and light, which in turn promotes their performance in optoelectronic devices. In this study, we combine composition-control with dimensionality-control of organometal halide perovskite crystals by tuning halide incorporation and exploiting bulky alkylammonium cations as capping ligands. We demonstrate a systematic synthesis of all the series of mixed halide perovskite polycrystals and their low dimensional analogues. Both structural and optical properties exhibit a non-linear relationship between synthetic loadings *vs.* compositions, which to our knowledge has not been reported yet. We speculate this non-linear behavior is caused by the differences in structure phases, halide radii, precursor reactivities, lattice entropies and precursor solubilities. Also, by optimizing synthetic conditions, we are able to inhibit the appearance of a reversible photoinduced PL peak derived from surface traps.

Introduction

Organolead halide perovskites of general composition $RPbX_3$ (R = organic monocation such as $CH_3NH_3^+$, X = I, Br, Cl) have drawn great attention as both photovoltaic materials[1-8] and fluorophores.[9-14] The certified power conversion efficiency of perovskite solar cells surged from 3.8% to over 20% in the last five years.[15-19] Broad light

absorption and long carrier diffusion lengths make perovskites ideal light harvesters.[20] Because of their composition-tunable bandgap and high photoluminescence quantum yield, perovskites are also of interest as light-emitting materials.[21] In spite of these many advantages, organometal perovskites suffer from instability against moisture, heat and light.[22, 23] A deeper understanding of the fundamental physical and chemical behavior of perovskites could help in mitigating these instability issues, thus enabling their implementation and deployment into useful energy technologies.

Efforts to improve the physical and chemical properties of perovskites are focused on tuning their composition or dimensionality.[24, 25] Compositional flexibility makes these materials very interesting from both a fundamental and applied perspectives. Substituting $CH_3NH_3^+$ with other cations such as formamidinium ($HN=CHNH_3^+$) or cesium (Cs^+) leads to superior devices with enhanced short-circuit current or increased thermal stability, respectively.[26-28] Dimensionality controls may be useful in tuning the bandgap energies of some perovskite materials via quantum confinement. Partial substitution with long alkylammonium cations leads to low dimensional perovskites,[29] some of which exhibit enhanced moisture stability.[30] Halide substitution also leads to enhanced stability, as $CH_3NH_3PbI_3$ solar cells doped with Br show long-lasting resistance against humidity.[31, 32] $CH_3NH_3PbBr_3$ displays lower sensitivity to concentrated sun-light compared to $CH_3NH_3PbI_3$.[33] Halide incorporation or "doping" has been widely exploited in enhancing the power conversion efficiency of perovskite solar cells.[34, 35] Because of the different optical properties of different compositions, for example $CH_3NH_3PbCl_3$ (3.1 eV, 400 nm), $CH_3NH_3PbBr_3$ (2.3 eV, 540 nm) and $CH_3NH_3PbI_3$ (1.5 eV, 820 nm),[36] compositional variation leads to mixed perovskites whose bandgap and emission energies cover the entire visible spectrum.[37, 38]

A few reports describe the unusual photophysical behavior of organometal halide perovskites, and specifically their reversible shift in PL_{max} under thermal *vs.* photochemical conditions.[39-41] Often attributed to the formation of different halide-rich surface clusters, these structural defects may account for the notorious photocurrent hysteresis[42] and decreased quantum efficiency[43] that characterizes perovskite semiconductors and devices. Calculations reveal the unusual defect physics of $CH_3NH_3PbX_3$: dominant intrinsic defects create only shallow levels,[44-47] which partially explain the long electron-hole diffusion length and high open-circuit voltage in solar cells.[48] Because they are caused by surface defects, these unusual photophysics may become even more prominent in low dimensional perovskites.[49]

Trap states in perovskites. $CH_3NH_3PbI_3$ and $CH_3NH_3PbI_{3-x}Cl_x$ emit intensively and the peak is broad. The nature of the radiative decay channels and the spectral broadening mechanisms most likely result from phonon coupling effects and defects or trap states.[50] The trap states, possibly caused by electron−phonon coupling, are enhanced at surfaces/interfaces where the perovskite crystal structure is most susceptible to deformation, which are even more significant in 2D perovskites.[51] Elemental defects like Pb, I, and CH_3NH_3 vacancies can also form shallow trap states and reduce carrier lifetime.[52] Both Pb cations and I anions exhibit strong covalency, which leads to the formation of Pb dimers and I trimers in intrinsic defects and is responsible for deep transition levels which can serve as recombination centers harmful for solar cells.[53] Synthesis condition plays an important role in the formation of trap states: perovskites grown under iodine-rich conditions are likely to have a high density of deep electronic traps (recombination centers) and the formation of key defects (Pb atom substituted by I) which causes short diffusion lengths and poor photovoltaic performance.[54]

Additives. Supramolecular halogen bond complexation can passivate the under-coordinated iodine ions, which can reduce trap sites near the perovskite surface;[55] whereas Lewis bases are used to passivate under-coordinated Pb atoms and treated perovskites demonstrate reduced nonradiative electron hole recombination and longer PL lifetimes.[56] Other interface engineering, such as adding fullerene layers, has also proven to be an effect way to passivate the charge trap states and get rid of photocurrent hysteresis.[57, 58]

Here, by tuning halide-incorporation and exploiting bulky alkylammonium cations as capping ligands, we combine composition-control with dimensionality-control. Building on our previous work, we demonstrate a systematic synthesis of all the series of mixed halide perovskite polycrystals and their low dimensional forms. We also study their structural and optical properties, which exhibit a non-linear relationship between synthetic loadings *vs.* compositions. To our knowledge it has not been reported yet. We attribute this bowing behavior to the differences in structure phases, halide radii, precursor reactivities, lattice entropies and precursor solubilities. Also, by optimizing synthetic conditions, we are able to inhibit the appearance of a reversible 'blue' PL peak derived from surface traps.

Experimental Section

Materials. Lead(II) iodide (99%), lead(II) bromide (⩾ 98%), methylamine (33 wt% in ethanol), N, N-dimethylformamide (DMF) (anhydrous, 99.8%) and n-octylamine (99%) were purchased from Sigma-Aldrich. Hydroiodic acid (ACS, 55-58%), hydrobromic acid (ACS, 47.0-49.0%) and oleic acid (tech., 90%) from Alfa-Aesar; acetonitrile (99.9%) and toluene (99.9%) from Fisher; diethyl ether from Baker. All chemicals were used as received unless specified otherwise.

Synthesis. *Ammonium Halides*. Hydrogen halides were prepared by a modified literature procedure.[52] Briefly, hydroiodic acid (10 mL, 0.075 mol), hydrobromic acid (8.6 mL, 0.075 mol), or hydrochloric acid (6.2 mL, 0.075 mol) was added to a solution of excess

methylamine (24 mL, 0.192 mol) in ethanol (100 mL) at 0 °C, and the mixture stirred at this temperature for 2 h. The sample was concentrated under vacuum, and the resulting powder dried under dynamic vacuum at 60 °C for 12 h and recrystallized from ethanol. *n*-Octylammonium iodide ($CH_3(CH_2)_7NH_3I$), *n*-octylammonium bromide ($CH_3(CH_2)_7NH_3Br$), and *n*-octylammonium chloride ($CH_3(CH_2)_7NH_3Cl$) were washed repeatedly with diethyl ether and dried under dynamic vacuum before use.

Bulk (polycrystalline) $CH_3NH_3Pb(Cl_xBr_{1-x})_3$. Cl Solution. $PbCl_2$ (11.1 mg, 0.04 mmol) and CH_3NH_3Cl (2.8 mg, 0.04 mmol) were dissolved in DMF (1 mL). Br Solution. $PbBr_2$ (14.7 mg, 0.04 mmol) and CH_3NH_3Br (4.6 mg, 0.04 mmol) were dissolved in DMF (1 mL). Solutions *Cl* and *Br* were mixed in different proportions or relative halide loadings to a total volume of 100 µL, followed by the rapid addition of toluene (10 mL) while stirring in air. After 24 h stirring at room temperature (R.T., 294 K), solids were isolated by centrifugation (10 min at 4000 rpm). The solids were washed once by dissolution in toluene (5 mL) and re-centrifugation. *Low-dimensional (nano)* $CH_3NH_3Pb(Cl_xBr_{1-x})_3$. *Cl Solution*. $PbCl_2$ (11.1 mg, 0.04 mmol), CH_3NH_3Cl (1.4 mg, 0.02 mmol) and $CH_3(CH_2)_7NH_3Cl$ (3.3 mg, 0.02 mmol) were dissolved in DMF (1 mL). *Br Solution*. $PbBr_2$ (14.7 mg, 0.04 mmol), CH_3NH_3Br (2.3 mg, 0.02 mmol) and $CH_3(CH_2)_7NH_3Br$ (4.2 mg, 0.02 mmol) were dissolved in DMF (1 mL). After 24 h stirring at room temperature (R.T., 294 K), solids were isolated and purified as specified above for the bulk samples.

Bulk (polycrystalline) $CH_3NH_3Pb(Br_xI_{1-x})_3$. *Br Solution*. $PbBr_2$ (2.9 mg, 0.008 mmol) and CH_3NH_3Br (2.6 mg, 0. 024 mmol) were dissolved in a mixture of acetonitrile (20mL) and DMF (0.2 mL). *I Solution*. PbI_2 (3.7 mg, 0.008 mmol) and CH_3NH_3I (3.8 mg, 0. 024 mmol) were dissolved in a mixture of acetonitrile (20 mL) and DMF (200 µL). Solutions *Br* and *I* were mixed in different proportions or relative halide loadings to a total volume of 4 mL, followed by the rapid addition of toluene (15 mL) while stirring in air.

After 24 h stirring at R.T., solids were isolated by centrifugation (10 min at 4000 rpm). The solids were washed once by dissolution in toluene (5 mL) and re-centrifugation. Low-dimensional (nano) $CH_3NH_3Pb(Br_xI_{1-x})_3$. *Br Solution*. $PbBr_2$ (2.9 mg, 0.008 mmol), CH_3NH_3Br (1.3 mg, 0.012 mmol) and $CH_3(CH_2)_7NH_3Br$ (2.5 mg, 0.012 mmol) were dissolved in a mixture of acetonitrile (20 mL) and DMF (0.2 mL). *I Solution*. PbI_2 (3.7 mg, 0.008 mmol), CH_3NH_3I (1.9 mg, 0.012 mmol) and $CH_3(CH_2)_7NH_3I$ (3.1 mg, 0.012 mmol) were dissolved in a mixture of acetonitrile (20 mL) and DMF (200 µL). After 24 h stirring at room temperature (R.T., 294 K), solids were isolated and purified as specified above for the bulk samples. Dry samples were stored in glovebox (O_2 level = 0.1 ppm; H_2O level= 0.1 ppm).

Structural Characterization. *Powder X-Ray Diffraction (XRD)*. XRD data were measured on Rigaku Ultima IV (40 kV, 44 mA) using Cu Kα radiation. Samples were drop casted from toluene onto a background-less quartz sample holder in air. XRD was collected on fresh samples due to the sensitivity of perovskites against moisture. Usually the synthesis and characterization occur at the same day. *Transmission Electron Microscopy (TEM)*. TEM was conducted using a FEI Technai G2 F20 field emission TEM operating at up to 200 kV with a point-to-point resolution of less than 0.25 nm and a line-to-line resolution of less than 0.10 nm. Samples were prepared by placing 2 or 3 drops of dilute toluene solutions onto carbon-coated copper grids. *Size and Morphology Analysis.* Particle dimensions were measured manually or with ImageJ or both. Typically, >100 particles were counted in each case. Uncertainties in all measurements are reported as standard deviations.

Optical Characterization. *Optical Extinction*. Optical Extinction (absorption plus scattering) spectra in solution phase were measured with a photodiode-array Agilent 8453 UV/Vis spectrophotometer. Solvent absorption was recorded and subtracted from all

spectra. *Diffuse Reflectance*. Diffuse reflectance spectra of solid films were measured with a SL1 Tungsten Halogen lamp (vis-IR), a SL3 Deuterium Lamp (UV), and a BLACK-Comet C-SR-100 Spectrometer. Samples were prepared by drop-casting toluene solutions onto a glass slide. *Photoluminescence (PL). Steady-State PL Measurements.* Steady-state PL spectra were measured with a Horiba-Jobin Yvon Nanolog scanning spectrofluorometer equipped with a photomultiplier detector. Relative PL quantum yields (QYs) were measured following literature procedures, using either Rhodamine 590 or Rhodamine 640 dye as standard. Absorption and PL emission spectra were measured as triplicates and the average QYs recorded.

Results and Discussion

General Synthesis and Size Control. We prepare polycrystalline (bulk) organolead halide perovskites by dissolving PbX_2 (*a* in Scheme 1) and CH_3NH_3X (*b*) precursors (X = I, Br or Cl) in a polar solvent such as dimethyl formamide (DMF, ε = 38.25) or acetonitrile (ε = 36.64) or both, followed by quick injection of this mixed precursor solution into a less polar solvent such as toluene (ε = 2.379).[59] DMF as the precursor solvent is initially investigated due to its good solubility; however, only the series of $CH_3NH_3PbCl_xBr_{3-x}$ crushes out in toluene whereas the series of $CH_3NH_3PbBr_xI_{3-x}$ precursors forms some amorphous loosely held aggregates. Organometal perovskites have limited solubility in acetonitrile, and previously it has been used for synthesizing $CH_3NH_3PbI_3$ nanowires by our group. In the case of $CH_3NH_3PbBr_xI_{3-x}$, when an acetonitrile and DMF co-solvent is used, perovskite crystals precipitate in toluene. It is worth mentioning the lead perovskites are quite stable in dry air, usually lasting one week before decomposition. But to make sure the samples remain as perovskite structures, we synthesize and characterize the samples on the same day.

To grow perovskite nanoparticles, CH_3NH_3X is equally replaced by a second, larger alkyl ammonium halide such as n-$C_8H_{17}NH_3X$ ($c = b$, Scheme 1), which allows decreasing the particle size from bulk to nano. The large n-$C_8H_{17}NH_3^+$ (octyl) cation introduced in this way does not fit within the perovskite lattice, thus acting as a crystal-size limiting, surface-generating agent.[29] Nanoparticles of organometal halide perovskites thus produced likely contain methyl ammonium cations within their inorganic core, and a smaller amount of octyl ammonium groups on their particle surface ($z << 1$, Scheme 1).

Scheme 1. Synthesis of mixed-halide organolead perovskites of different dimensionality (bulk *vs.* nano).

$$ay\ PbX_2 + a(1-y)\ PbX'_2 + by\ CH_3NH_3X + b(1-y)\ CH_3NH_3X' + cy\ (\text{n-}C_8H_{17}NH_3X) + c(1-y)\ (\text{n-}C_8H_{17}NH_3X') \xrightarrow[(2)\ \text{Toluene}]{(1)\ CH_3CN\ \text{and/or DMF}} (CH_3NH_3)_{1-z}(\text{n-}C_8H_{17}NH_3)_zPb(X_yX'_{1-y})_3$$

Bulk: $a = 1;\ b = 1,\ 3;\ c = 0;\ z = 0;\ 0 \le y \le 1$
Nano: $a = 1;\ b = 0.5, 1.5;\ c = 0.5, 1.5;\ 0 < z << 1;\ 0 \le y \le 1$

Composition Control and Excess Precursors. To systematically synthesize mixed-halide (Br-I or Cl-Br) perovskites, we kept all conditions the same (see Experimental), including the precursors, solvents, total ion concentrations, and injection rate. In the case of Cl-Br perovskites, we use equimolar amounts of ammonium and lead halides ($b + c$ = a, Scheme 1). In the particular case of Br-I perovskites, the PbI_2 precursor fails to completely dissolve in the co-solvent unless an excess of ammonium halide precursors is present ($b + c$ = 3a, Scheme 1); having some excess ammonium halides also prevents the formation of crystalline byproducts and impurities. However, a very large excess of ammonium halides irreversibly affects the optical properties of the resulting perovskites, as discussed below.

Structural Analysis. Powder X-ray diffraction (XRD) shows that each of the bulk and nano mixed-halide perovskite samples contains a set of crystalline peaks (Figure 1 and Figure S1-S4). The diffraction peaks gradually shift from $CH_3NH_3PbCl_3$, to $CH_3NH_3PbBr_3$, to

$CH_3NH_3PbI_3$ as the synthetic loading of less electronegative halide is increased, indicating some degree of solid solution. As noted previously, perovskite nanocrystals show a significant degree of preferred orientation, specifically along the <110> for $CH_3NH_3PbI_3$ and <001> for other mixed-halide perovskites (Figure 1b). In addition, $CH_3NH_3PbCl_3$ nanocrystals display some diffraction peaks outside of the reported (standard) perovskite pattern. A plot of cubic (or pseudocubic in the case of X = I) lattice parameter *a*, determined experimentally from the powder XRD data, against synthetic halide loading reveals a nearly linear relationship for the Cl-Br series, but significant bowing behavior for the Br-I series (Figure 1c). The curvature of the Br-I plot strongly indicates the favorable formation of Br-rich (I-poor) perovskite phases (Figure 1c).[60]

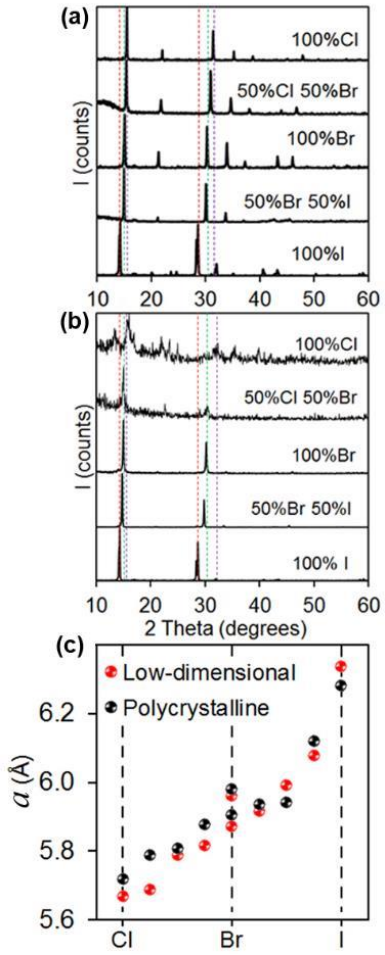

Figure 1. Powder XRD of polycrystalline (bulk) (a) and low-dimensional (nano) (b) mixed halide perovskites. The red, green and purple dashed lines correspond to the strongest,

(110) and (001) diffraction peaks in the standard patterns of iodide, bromide and chloride perovskites. (c) Lattice parameter *a* as a function of synthetic halide loading.

To account for the linear (Cl-Br) *vs.* bowing (Br-I) behavior observed in the loading-dependent lattice parameter plots mentioned above, we consider Hume-Rothery rules.[61] According to these rules, substitutional solid solutions form when (1) two compounds share similar crystal structures, (2) their ions have similar charge and electronegativity and (3) the radius difference between them is less than 15%. The organolead bromide and chloride perovskites share similar cubic crystal structures, while the iodide perovskite has a tetragonal structure (Figure 2).[62] The elemental electronegativities (χ_P) and monoanionic radii between halide pairs are well under 15% for the Cl-Br and Br-I systems (but well over for the Cl-I system, which is of technical importance for solar cell development.[63] but was not explored here) (Table 1). Based on these rules, binary solid solution is feasible across the whole composition range for chloride-bromide (Cl-Br) perovskites, is somewhat limited due to the different parent crystal structures for bromide-iodide (Br-I) perovskites, and is likely difficult for the chloride-iodide (Cl-I) perovskites (Figure 2 and Table 1).[64] We also assess the relative stabilities of different halide perovskites based on lattice energies (U_L),[65, 66] which show the bromide is *ca.* 130 kJ/mol more thermodynamically stable than the iodide according to U_L(Table 2). This may also throw light upon the Br-preferred tendency in Br-I perovskite series.

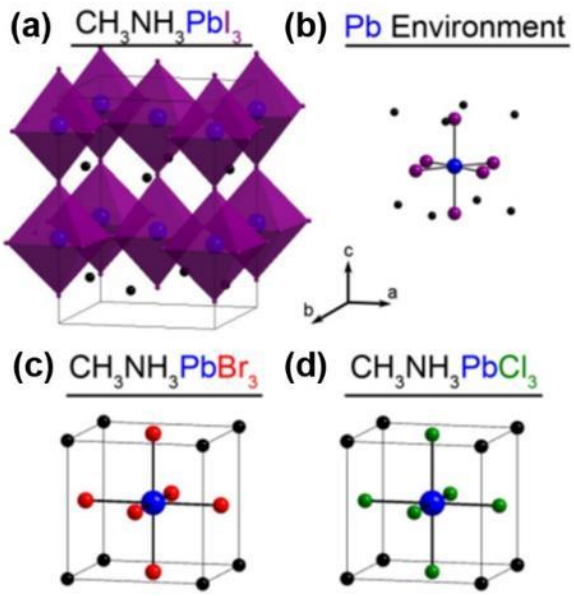

Figure 2. (a) Tetragonal unit cell of the organolead iodide perovskite $CH_3NH_3PbI_3$. (b) Octahedral hexahalolead(II) coordination geometry of organolead halide perovskites. Cubic unit cells of organolead (c) bromide $CH_3NH_3PbBr_3$ and (d) chloride $CH_3NH_3PbCl_3$ perovskites.

Table 1. Structural parameters of $CH_3NH_3PbX_3$ perovskites.

X	χ_P^X	r^{X-} (pm)	Δr^{Cl} (%)[a]	Δr^{Br} (%)[b]	a(Å)	Δa_{Cl} (%)[d]	Δa_{Br} (%)[e]	U_L (kJ/mol)
Cl	2.66	181	0	-7.2	5.6694	0	-4.5	-2464
Br	2.96	195	7.7	0	5.9345	4.7	0	-2374
I	3.16	216	19	11	6.3115, 6.3161[c]	11	6.4	-2244

[a]Radius mismatch $\Delta r^{Cl} = 100 \times [(r^{X-} - r^{Cl-})/r^{Cl-}]$. [b]Radius mismatch $\Delta r^{Br} = 100 \times [(r^{X-} - r^{Br-})/r^{Br-}]$. [c]Tetragonal system ($a$, c).[d] Lattice mismatch (Δl) = $100 \times [(a_x - a_{Cl})/a_{Cl}]$. [e]Lattice mismatch ($\Delta l$) = $100 \times [(a_x - a_{Br})/a_{Br}]$.

Except the differences in crystal structures and ionic radii, precursor reactivities and ease of forming solid solutions may also account for the non-linear behaviors. CH_3NH_3X salts dissociate differently in DMF depending on the specific halide (Scheme 2). For iodide, the preferred products are $CH_3NH_3^+$ and I^-, the conjugate base of HI, which is a strong acid in DMF and leads to a large conductivity (Scheme 2a, Figure 3 when $[PbX_2]_T = 0$). For

bromide, and even more for chloride, the preferred products are CH_3NH_2 along with HBr or HCl, respectively, both of which are weaker acids in DMF and leads to a smaller conductivity (Scheme 2b, Figure 3 when $[PbX_2]_T = 0$).[67] Thus, CH_3NH_3I is expected to be the most reactive ammonium halide precursor in DMF, generating free and readily available I^- needed for perovskite formation that should be easily precipitated upon addition of a nonpolar solvent such as toluene.

Scheme 2. Pathways of CH_3NH_3X dissociation in DMF.

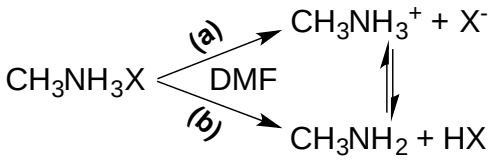

To probe PbX_2 precursor reactivity, we measured their specific conductivities (κ) in DMF with both the presence and absence of a set amount of the corresponding CH_3NH_3X (Figure 3). As expected in pure DMF, the conductivity increases linearly with PbX_2 concentration. A steeper increase for the iodide case suggests that dissociation is slightly higher for PbI_2 than for $PbBr_2$ and $PbCl_2$. In contrast, with the presence of 50 mM CH_3NH_3X in DMF, the conductivity actually decreases upon addition of PbI_2, slowly increases upon addition of $PbBr_2$, and more rapidly increases upon addition of $PbCl_2$. Because conductivity is proportional to the number of ions in solution, this data strongly suggests that PbI_2 and CH_3NH_3I interact most strongly, likely forming various PbI_n^{2-n} complexes that result in fewer ions in solution and a lower conductivity.[68-72] Thus, while CH_3NH_3I produces the most ions in DMF, these strongly interact with PbI_2 to form soluble, less ionic species that stabilize the precursors in solution and lead to the inability of PbI_2 to precipitate out of DMF, especially when high concentrations are used.

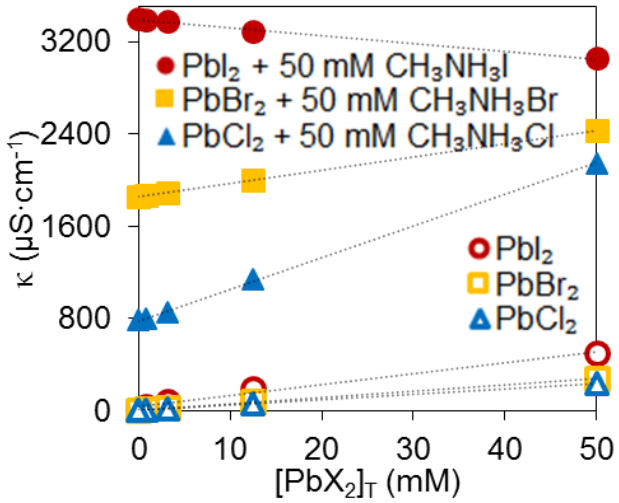

Figure 3. Specific conductivity (κ) *vs.* PbX_2 concentration with (solid) or without (hollow) 50 mM CH_3NH_3X.

Further structural analysis of the low dimensional mixed-halide perovskites by transmission electron microscopy (TEM) reveals that these samples are primarily made of dot-shaped particles with an average size of 7-10 nm (Figure 4). The Br-rich (≥ 75% Br-loading) perovskites also contain a small, minor morphology, nanosheets, which make up *ca.* 10-20% of particles in these samples (Figure S5-S7). As previously reported by our group, perovskite nanosheets are unstable under the TEM electron beam. The presence of nanosheets is a second contributing factor for the preferred orientation behavior observed by powder XRD for perovskite nanocrystals.

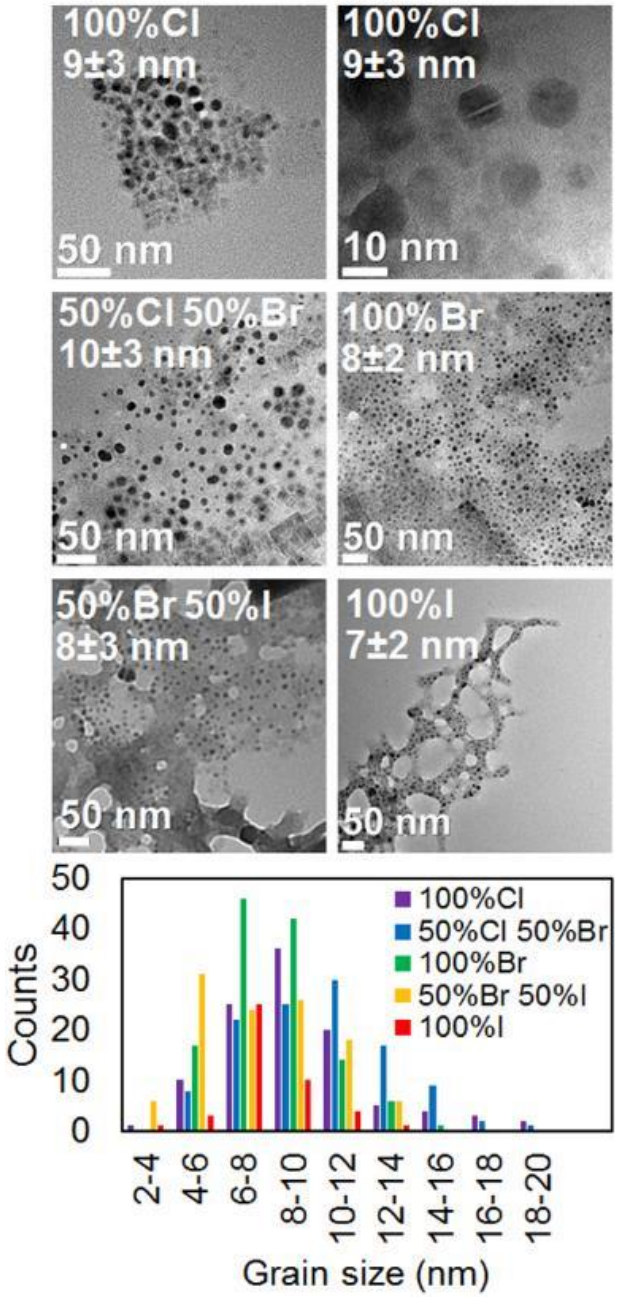

Figure 4. Representative TEM images and particle size histograms of mixed-halide organolead halide perovskite nanocrystals.

Optical Properties. As observed for the powder XRD patterns (above), the optical absorption edges of the mixed-halide organometal perovskites gradually shift from 400 nm to 760 nm on going from $CH_3NH_3PbCl_3$, to $CH_3NH_3PbBr_3$, to $CH_3NH_3PbI_3$, confirming that the bandgaps of these materials are compositionally-tunable (Figures 5 and 6).[73,74]

Under ambient light, the sample colors progressively change from milky white to dark brown as the synthetic loading of the less electronegative halide is increased.

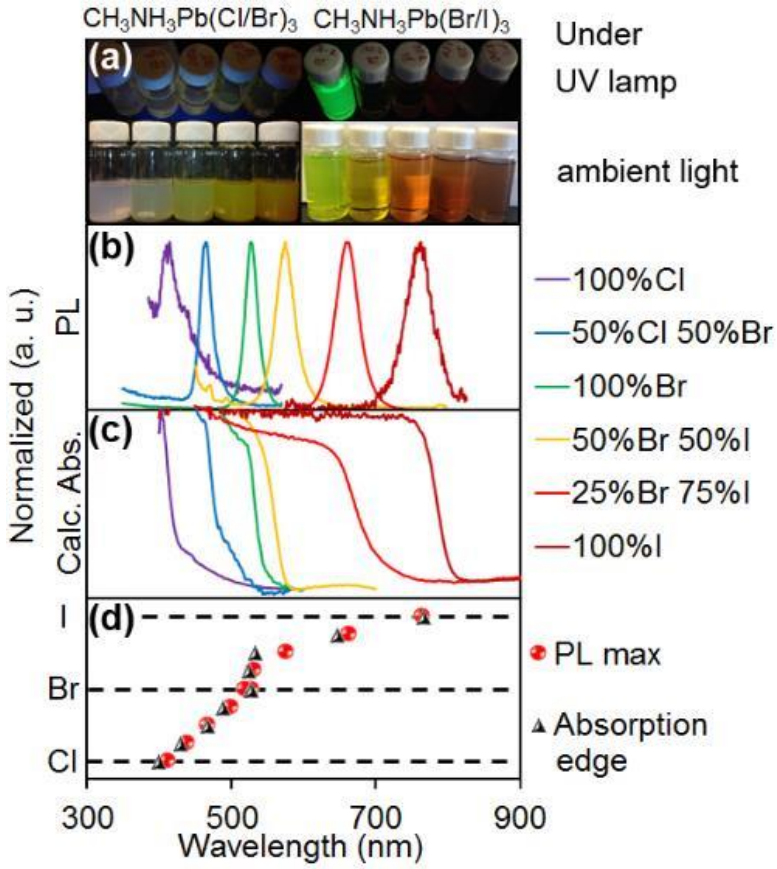

Figure 5. Ensemble optical properties of polycrystalline (bulk) organometal mixed-halide perovskites $CH_3NH_3PbX_3$ (X=Cl, Br, I): (a) Samples under UV (top panel) and ambient light (second panel); (b) emission spectra (λ_{exc} = 300 nm for $CH_3NH_3Pb(Cl/Br)_3$, 430 nm for $CH_3NH_3Pb(Br/I)_3$); (c) diffuse reflectance spectra; (d) PL maxima and absorption edge as a function of halide loading.

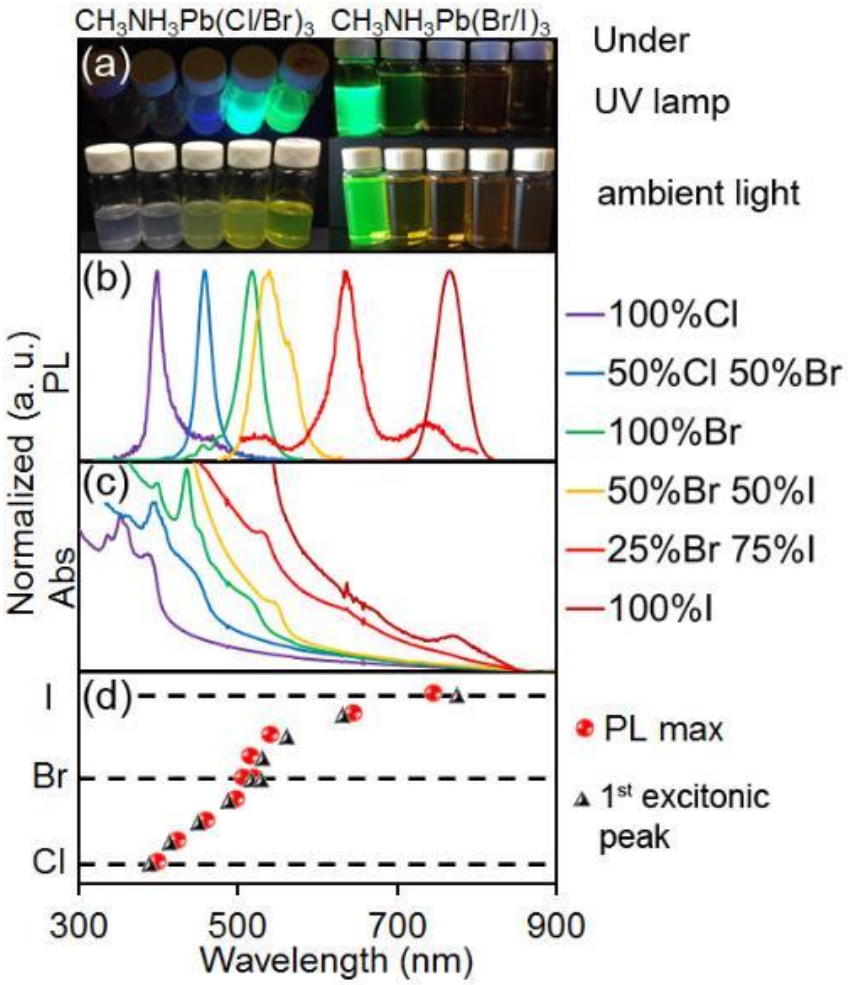

Figure 6. Ensemble optical properties of low-dimensional (nano) organometal mixed-halide perovskites $CH_3NH_3PbX_3$ (X=Cl, Br, I): (a) Samples in toluene under UV lamp (top panel) and ambient light (second panel); (b) emission spectra (λ_{exc} = 300 nm for $CH_3NH_3Pb(Cl/Br)_3$, 430 nm for $CH_3NH_3Pb(Br/I)_3$); (c) absorption spectra in toluene; (d) PL maxima and absorption edge as a function of halide loading.

All of the mixed-halide perovskites emit light under UV lamp irradiation. The low-dimensional (nanosized) mixed-halide perovskites are generally stronger photoluminescence (PL) emitters, with the pure $CH_3NH_3PbBr_3$ perovskite sample having the highest PL quantum yield (QY) of 44% (Table S2). The PL emission spectra of mixed-halide perovskites range across the whole visible spectral region from 400 nm to 760 nm (Figures 4 and 5). A plot of absorption edge (for bulk samples) or first excitonic peaks (for

nano samples) against synthetic halide loading reveals (in both types of samples) a nearly linear relationship for the Cl-Br series, but significant bowing behavior for the Br-I series (Figures 2c and 3c). The curvature of the Br-I plot strongly indicates the favorable formation of Br-rich (I-poor) perovskite phases, in agreement with our XRD observations above.

Conclusion

In summary, we combine composition-control with dimensionality-control of organometal halide perovskite crystals by tuning halide-incorporation and exploiting bulky alkylammonium cations as capping ligands. We demonstrate a systematic synthesis of all the series of mixed halide perovskite polycrystals and their low dimensional analogues. Both structural and optical properties exhibit a non-linear relationship between synthetic loadings *vs*. compositions, which to our knowledge has not been reported yet. We speculate this non-linear behavior is caused by the differences in structure phases, halide radii, precursor reactivities, lattice entropies and precursor solubilities. Also, by optimizing synthetic conditions, we are able to inhibit the appearance of a reversible photoinduced PL peak derived from surface traps.

Acknowledgement

This research is supported by the U.S. Department of Energy, Office of Basic Energy Sciences, Division of Chemical Sciences, Geo-sciences, and Biosciences through the Ames Laboratory. The Ames Laboratory is operated for the U.S. Department of Energy by Iowa State University under Contract No. DE-AC02-07CH11358. We thank M. A. White for graphics assistance.

References

(1) Grätzel, M. The Light and Shade of Perovskite Solar Cells. *Nature mater.* **2014,** *13*, 838–842.

(2) Green, M. A.; Ho-Baillie, A.; Snaith, H. J. The Emergence of Perovskite Solar Cells. *Nature Photon.* **2014,** *8*, 506–514.

(3) Park, N.-G. Organometal Perovskite Light Absorbers toward a 20% Efficiency Low-Cost Solid-State Mesoscopic Solar Cell. *J. Phys. Chem. Lett.* **2013,** *4*, 2423–2429.

(4) Kazim, S.; Nazeeruddin, M. K.; Grätzel, M.; Ahmad, S. Perovskite as Light Harvester: A Game Changer in Photovoltaics. *Angew. Chem. Int. Ed.* **2014,** *53*, 2812–2824.

(5) Gao, P.; Gratzel, M.; Nazeeruddin, M. K. Organohalide Lead Perovskites for Photovoltaic Applications. *Energy Environ. Sci.* **2014,** *7*, 2448–2463.

(6) Kamat, P. V. Evolution of Perovskite Photovoltaics and Decrease in Energy Payback Time. *J. Phys. Chem. Lett.* **2013,** *4*, 3733–3734.

(7) Bisquert, J. The Swift Surge of Perovskite Photovoltaics. *J. Phys. Chem. Lett.* **2013,** *4*, 2597–2598.

(8) Zhao, Y.; Zhu, K. Organic–Inorganic Hybrid Lead Halide Perovskites for Optoelectronic and Electronic Applications. *Chem. Soc. Rev.* **2016**.

(9) Deschler, F.; Price, M.; Pathak, S.; Klintberg, L. E.; Jarausch, D.-D.; Higler, R.; Hüttner, S.; Leijtens, T.; Stranks, S. D.; Snaith, H. J.; Atatüre, M.; Phillips, R. T.; Friend, R. H. High Photoluminescence Efficiency and Optically Pumped Lasing in Solution-Processed Mixed Halide Perovskite Semiconductors. *J. Phys. Chem. Lett.* **2014,** *5*, 1421–1426.

(10) Schmidt, L. C.; Pertegás, A.; González-Carrero, S.; Malinkiewicz, O.; Agouram, S.; Mínguez Espallargas, G.; Bolink, H. J.; Galian, R. E.; Pérez-Prieto, J. Nontemplate Synthesis of $CH_3NH_3PbBr_3$ Perovskite Nanoparticles. *J. Am. Chem. Soc.* **2014,** *136*, 850–853.

(11) Tan, Z.-K.; Moghaddam, R. S.; Lai, M. L.; Docampo, P.; Higler, R.; Deschler, F.; Price, M.; Sadhanala, A.; Pazos, L. M.; Credgington, D.; Hanusch, F.; Bein, T.; Snaith, H.

J.; Friend, R. H. Bright Light-Emitting Diodes Based on Organometal Halide Perovskite. *Nat. Nanotechnol.* **2014,** *9*, 687–692.

(12) Zhang, F.; Zhong, H.; Chen, C.; Wu, X.-G.; Hu, X.; Huang, H.; Han, J.; Zou, B.; Dong, Y. Brightly Luminescent and Color-Tunable Colloidal $CH_3NH_3PbX_3$ (X = Br, I, Cl) Quantum Dots: Potential Alternatives for Display Technology. *ACS Nano* **2015,** *9*, 4533–4542.

(13) Sichert, J. A.; Tong, Y.; Mutz, N.; Vollmer, M.; Fischer, S.; Milowska, K. Z.; García Cortadella, R.; Nickel, B.; Cardenas-Daw, C.; Stolarczyk, J. K.; Urban, A. S.; Feldmann, J. Quantum Size Effect in Organometal Halide Perovskite Nanoplatelets. *Nano Lett.* **2015,** *15*, 6521–6527.

(14) Pathak, S.; Sakai, N.; Wisnivesky Rocca Rivarola, F.; Stranks, S. D.; Liu, J.; Eperon, G.; Ducati, C.; Wojciechowski, K.; Griffiths, J. T.; Haghighirad, A. A. Perovskite Crystals for Tuneable White Light Emission. *Chem. Mater.*, **2015**, *27*, 8066–8075.

(15) Kojima, A.; Teshima, K.; Shirai, Y.; Miyasaka, T. Organometal Halide Perovskites as Visible-Light Sensitizers for Photovoltaic Cells. *J. Am. Chem. Soc.* **2009,** *131*, 6050–6051.

(16) Liu, M.; Johnston, M. B.; Snaith, H. J. Efficient Planar Heterojunction Perovskite Solar Cells by Vapour Deposition. *Nature* **2013,** *501*, 395–398.

(17) Burschka, J.; Pellet, N.; Moon, S.-J.; Humphry-Baker, R.; Gao, P.; Nazeeruddin, M. K.; Gratzel, M. Sequential Deposition as a Route to High-Performance Perovskite-Sensitized Solar Cells. *Nature* **2013,** *499*, 316–319.

(18) Zhou, H.; Chen, Q.; Li, G.; Luo, S.; Song, T.-B.; Duan, H.-S.; Hong, Z.; You, J.; Liu, Y.; Yang, Y. Interface Engineering of Highly Efficient Perovskite Solar Cells. *Science* **2014,** *345*, 542–546.

(19) Yang, W. S.; Noh, J. H.; Jeon, N. J.; Kim, Y. C.; Ryu, S.; Seo, J.; Seok, S. I. High-Performance Photovoltaic Perovskite Layers Fabricated through Intramolecular Exchange. *Science* **2015,** *348*, 1234–1237.

(20) Dong, Q.; Fang, Y.; Shao, Y.; Mulligan, P.; Qiu, J.; Cao, L.; Huang, J. Electron-Hole Diffusion Lengths > 175 μm in Solution-Grown $CH_3NH_3PbI_3$ Single Crystals. *Science* **2015,** *347*, 967–970.

(21) Protesescu, L.; Yakunin, S.; Bodnarchuk, M. I.; Krieg, F.; Caputo, R.; Hendon, C. H.; Yang, R. X.; Walsh, A.; Kovalenko, M. V. Nanocrystals of Cesium Lead Halide Perovskites ($CsPbX_3$, X= Cl, Br, and I): Novel Optoelectronic Materials Showing Bright Emission with Wide Color Gamut. *Nano Lett.* **2015**, *15*, 3692–3696.

(22) Christians, J. A.; Miranda Herrera, P. A.; Kamat, P. V. Transformation of the Excited State and Photovoltaic Efficiency of $CH_3NH_3PbI_3$ Perovskite upon Controlled Exposure to Humidified Air. *J. Am. Chem. Soc.* **2015,** *137*, 1530–1538.

(23) Conings, B.; Drijkoningen, J.; Gauquelin, N.; Babayigit, A.; D'Haen, J.; D'Olieslaeger, L.; Ethirajan, A.; Verbeeck, J.; Manca, J.; Mosconi, E. Intrinsic Thermal Instability of Methylammonium Lead Trihalide Perovskite. *Adv. Energy Mater.* **2015,** *5*, 1500477.

(24) Dou, L.; Wong, A. B.; Yu, Y.; Lai, M.; Kornienko, N.; Eaton, S. W.; Fu, A.; Bischak, C. G.; Ma, J.; Ding, T.; Ginsberg, N. S.; Wang, L.-W.; Alivisatos, A. P.; Yang, P. Atomically Thin Two-Dimensional Organic-Inorganic Hybrid Perovskites. *Science* **2015,** *349*, 1518–1521.

(25) Boix, P. P.; Agarwala, S.; Koh, T. M.; Mathews, N.; Mhaisalkar, S. G. Perovskite Solar Cells: Beyond Methylammonium Lead Iodide. *J. Phys. Chem. Lett.* **2015,** *6*, 898–907.

(26) Pellet, N.; Gao, P.; Gregori, G.; Yang, T. Y.; Nazeeruddin, M. K.; Maier, J.; Grätzel, M. Mixed-Organic-Cation Perovskite Photovoltaics for Enhanced Solar-Light Harvesting. *Angew. Chem. Int. Ed.* **2014,** *53*, 3151–3157.

(27) Stoumpos, C. C.; Malliakas, C. D.; Kanatzidis, M. G. Semiconducting Tin and Lead Iodide Perovskites with Organic Cations: Phase Transitions, High Mobilities, and Near-Infrared Photoluminescent Properties. *Inorg. Chem.* **2013,** *52*, 9019–9038.

(28) Eperon, G. E.; Stranks, S. D.; Menelaou, C.; Johnston, M. B.; Herz, L. M.; Snaith, H. J. Formamidinium Lead Trihalide: A Broadly Tunable Perovskite for Efficient Planar Heterojunction Solar Cells. *Energy Environ. Sci.* **2014,** *7*, 982–988.

(29) Zhu, F.; Men, L.; Guo, Y.; Zhu, Q.; Bhattacharjee, U.; Goodwin, P. M.; Petrich, J. W.; Smith, E. A.; Vela, J. Shape Evolution and Single Particle Luminescence of Organometal Halide Perovskite Nanocrystals. *ACS Nano* **2015,** *9*, 2948–2959.

(30) Smith, I. C.; Hoke, E. T.; Solis-Ibarra, D.; McGehee, M. D.; Karunadasa, H. I. A Layered Hybrid Perovskite Solar-Cell Absorber with Enhanced Moisture Stability. *Angew. Chem.* **2014,** *126*, 11414–11417.

(31) Noh, J. H.; Im, S. H.; Heo, J. H.; Mandal, T. N.; Seok, S. I. Chemical Management for Colorful, Efficient, and Stable Inorganic-Organic Hybrid Nanostructured Solar Cells. *Nano Lett.* **2013,** *13*, 1764–1769.

(32) Dimesso, L.; Dimamay, M.; Hamburger, M.; Jaegermann, W. Properties of $CH_3NH_3PbX_3$ (X= I, Br, Cl) Powders as Precursors for Organic/Inorganic Solar Cells. *Chem. Mater.* **2014,** *26*, 6762–6770.

(33) Misra, R. K.; Aharon, S.; Li, B.; Mogilyansky, D.; Visoly-Fisher, I.; Etgar, L.; Katz, E. A. Temperature- and Component-Dependent Degradation of Perovskite Photovoltaic Materials under Concentrated Sunlight. *J. Phys. Chem. Lett.* **2015,** *6*, 326–330.

(34) Kitazawa, N.; Watanabe, Y.; Nakamura, Y. Optical Properties of $CH_3NH_3PbX_3$ (X = Halogen) and Their Mixed-Halide Crystals. *J. Mater. Sci.* **2002,** *37*, 3585–3587.

(35) Suarez, B.; Gonzalez-Pedro, V.; Ripolles, T. S.; Sanchez, R. S.; Otero, L.; Mora-Sero, I. Recombination Study of Combined Halides (Cl, Br, I) Perovskite Solar Cells. *J. Phys. Chem. Lett.* **2014,** *5*, 1628–1635.

(36) Philippe, B.; Park, B.-W.; Lindblad, R.; Oscarsson, J.; Ahmadi, S.; Johansson, E. M. J.; Rensmo, H. Chemical and Electronic Structure Characterization of Lead Halide Perovskites and Stability Behavior under Different Exposures—A Photoelectron Spectroscopy Investigation. *Chem. Mater.* **2015,** *27*, 1720–1731.

(37) Jang, D. M.; Park, K.; Kim, D. H.; Park, J.; Shojaei, F.; Kang, H. S.; Ahn, J.-P.; Lee, J. W.; Song, J. K. Reversible Halide Exchange Reaction of Organometal Trihalide Perovskite Colloidal Nanocrystals for Full-Range Band Gap Tuning. *Nano Lett.* **2015,** *15*, 5191–5199.

(38) Zhang, M.; Yu, H.; Lyu, M.; Wang, Q.; Yun, J.-H.; Wang, L. Composition-Dependent Photoluminescence Intensity and Prolonged Recombination Lifetime of Perovskite $CH_3NH_3PbBr_{3-X}Cl_x$ Films. *Chem. Commun.* **2014,** *50*, 11727–11730.

(39) Hoke, E. T.; Slotcavage, D. J.; Dohner, E. R.; Bowring, A. R.; Karunadasa, H. I.; McGehee, M. D. Reversible Photo-Induced Trap Formation in Mixed-Halide Hybrid Perovskites for Photovoltaics. *Chem. Sci.* **2015,** *6*, 613–617.

(40) Sadhanala, A.; Deschler, F.; Thomas, T. H.; Dutton, S. E.; Goedel, K. C.; Hanusch, F. C.; Lai, M. L.; Steiner, U.; Bein, T.; Docampo, P.; Cahen, D.; Friend, R. H. Preparation of Single-Phase Films of $CH_3NH_3Pb(I_{1-x}Br_x)_3$ with Sharp Optical Band Edges. *J. Phys. Chem. Lett.* **2014,** *5*, 2501–2505.

(41) Gottesman, R.; Gouda, L.; Kalanoor, B. S.; Haltzi, E.; Tirosh, S.; Rosh-Hodesh, E.; Tischler, Y.; Zaban, A.; Quarti, C.; Mosconi, E.; De Angelis, F. Photoinduced Reversible

Structural Transformations in Free-Standing $CH_3NH_3PbI_3$ Perovskite Films. *J. Phys. Chem. Lett.* **2015,** *6*, 2332–2338.

(42) Shao, Y.; Xiao, Z.; Bi, C.; Yuan, Y.; Huang, J. Origin and Elimination of Photocurrent Hysteresis by Fullerene Passivation in $CH_3NH_3PbI_3$ Planar Heterojunction Solar Cells. *Nat. Commun.* **2014,** *5*, 5784.

(43) Stranks, S. D.; Burlakov, V. M.; Leijtens, T.; Ball, J. M.; Goriely, A.; Snaith, H. J. Recombination Kinetics in Organic-Inorganic Perovskites: Excitons, Free Charge, and Subgap States. *Phys. Rev.* **2014,** *2*, 034007–1–034007–6.

(44) Yin, W.-J.; Shi, T.; Yan, Y. Unusual Defect Physics in $CH_3NH_3PbI_3$ Perovskite Solar Cell Absorber. *Appl. Phys. Lett.* **2014,** *104*, 063903–1–063903–4.

(45) Agiorgousis, M. L.; Sun, Y.-Y.; Zeng, H.; Zhang, S. Strong Covalency-Induced Recombination Centers in Perovskite Solar Cell Material $CH_3NH_3PbI_3$. *J. Am. Chem. Soc.* **2014,** *136*, 14570–14575.

(46) Yin, W. J.; Shi, T.; Yan, Y. Unique Properties of Halide Perovskites as Possible Origins of the Superior Solar Cell Performance. *Adv. Mater.* **2014,** *26*, 4653–4658.

(47) Kim, J.; Lee, S.-H.; Lee, J. H.; Hong, K.-H. The Role of Intrinsic Defects in Methylammonium Lead Iodide Perovskite. *J. Phys. Chem. Lett.* **2014,** *5*, 1312–1317.

(48) Shi, T.; Yin, W.-J.; Hong, F.; Zhu, K.; Yan, Y. Unipolar Self-Doping Behavior in Perovskite $CH_3NH_3PbBr_3$. *Appl. Phys. Lett.* **2015,** *106*, 103902–1–103902–5.

(49) Wu, X.; Trinh, M. T.; Niesner, D.; Zhu, H.; Norman, Z.; Owen, J. S.; Yaffe, O.; Kudisch, B. J.; Zhu, X. Y. Trap States in Lead Iodide Perovskites. *J. Am. Chem. Soc.* **2015,** *137*, 2089–2096.

(50) Wehrenfennig, C.; Liu, M.; Snaith, H. J.; Johnston, M. B.; Herz, L. M. Homogeneous Emission Line Broadening in the Organo Lead Halide Perovskite $CH_3NH_3PbI_{3-x}Cl_x$. *J. Phys. Chem. Lett.* **2014,** *5*, 1300–1306.

(51) Wu, X.; Trinh, M. T.; Niesner, D.; Zhu, H.; Norman, Z.; Owen, J. S.; Yaffe, O.; Kudisch, B. J.; Zhu, X. Y. Trap States in Lead Iodide Perovskites. *J. Am. Chem. Soc.* **2015,** *137*, 2089–2096.

(52) Rosales, B. A.; Men, L.; Cady, S. D.; Hanrahan, M. P.; Rossini, A. J.; Vela, J. Persistent Dopants and Phase Segregation in Organolead Mixed-Halide Perovskites. *Chem. Mater.* **2016**, *28*, 6848−6859.

(53) Agiorgousis, M. L.; Sun, Y.-Y.; Zeng, H.; Zhang, S. Strong Covalency-Induced Recombination Centers in Perovskite Solar Cell Material $CH_3NH_3PbI_3$. *J. Am. Chem. Soc.* **2014,** *136*, 14570–14575.

(54) Buin, A.; Pietsch, P.; Xu, J.; Voznyy, O.; Ip, A. H.; Comin, R.; Sargent, E. H. Materials Processing Routes to Trap-Free Halide Perovskites. *Nano Lett.* **2014,** *14*, 6281–6286.

(55) Abate, A.; Saliba, M.; Hollman, D. J.; Stranks, S. D.; Wojciechowski, K.; Avolio, R.; Grancini, G.; Petrozza, A.; Snaith, H. J. Supramolecular Halogen Bond Passivation of Organic–Inorganic Halide Perovskite Solar Cells. *Nano Lett.* **2014,** *146*, 3247–3254

(56) Noel, N. K.; Abate, A.; Stranks, S. D.; Parrott, E. S.; Burlakov, V. M.; Goriely, A.; Snaith, H. J. Enhanced Photoluminescence and Solar Cell Performance via Lewis Base Passivation of Organic–Inorganic Lead Halide Perovskites. *ACS nano* **2014,** *8*, 9815–9821.

(57) Shao, Y.; Xiao, Z.; Bi, C.; Yuan, Y.; Huang, J. Origin and Elimination of Photocurrent Hysteresis by Fullerene Passivation in $CH_3NH_3PbI_3$ Planar Heterojunction Solar Cells. *Nat. Commun.* **2014,** *5*.

(58) Xu, J.; Buin, A.; Ip, A. H.; Li, W.; Voznyy, O.; Comin, R.; Yuan, M.; Jeon, S.; Ning, Z.; McDowell, J. J.; Kanjanaboos, P.; Sun, J.-P.; Lan, X.; Quan, L. N.; Kim, D. H.; Hill, I. G.; Maksymovych, P.; Sargent, E. H. Perovskite-Fullerene Hybrid Materials Suppress Hysteresis in Planar Diodes. *Nat. commun.***2015,** *6*.

(59) Payne, R. Incidence of Humps in the Double-Layer Capacity at the Mercury-Nonaqueous Solution Interface. *J. Phys.Chem.* **1967,** *71*, 1548–1549.

(60) Ruberu, T. P. A.; Vela, J. Expanding the One-Dimensional CdS-CdSe Composition Landscape: Axially Anisotropic $CdS_{1-x}Se_x$ Nanorods. *ACS Nano* **2011**, *5*, 5775–5784.

(61) Hume-Rothery, W. *The Structures of Alloys of Iron: An Elementary Introduction*. Elsevier: 2013.

(62) Zhu, H.; Fu, Y.; Meng, F.; Wu, X.; Gong, Z.; Ding, Q.; Gustafsson, M. V.; Trinh, M. T.; Jin, S.; Zhu, X. Y. Lead Halide Perovskite Nanowire Lasers with Low Lasing Thresholds and High Quality Factors. *Nat. Mater.* **2015,** *14*, 636–642.

(63) Lee, M. M.; Teuscher, J.; Miyasaka, T.; Murakami, T. N.; Snaith, H. J. Efficient Hybrid Solar Cells Based on Meso-Superstructured Organometal Halide Perovskites. *Science* **2012,** *338*, 643–647.

(64) Shannon, R. D.; Prewitt, C. T. Effective Ionic Radii in Oxides and Fluorides. *Acta Crystallogr. Sect. B.* **1969**, *25*, 925–946.

(65) Su, J.; Chen, D. P.; Lin, C. T. Growth of Large $CH_3NH_3PbX_3$ (X=I, Br) Single Crystals in Solution. *J. Cryst. Growth* **2015,** *422*, 75–79.

(66) Chi, L.; Swainson, I.; Cranswick, L.; Her, J.-H.; Stephens, P.; Knop, O. The Ordered Phase of Methylammonium Lead Chloride $CH_3ND_3PbCl_3$. *J. Solid State Chem.* **2005,** *178*, 1376–1385.

(67) Wang, Q.; Yun, J. H.; Zhang, M.; Chen, H.; Chen, Z. G.; Wang, L. Insight into the Liquid State of Organo-Lead Halide Perovskites and Their New Roles in Dye-Sensitized Solar Cells. *J. Mater. Chem. A* **2014**, *2*, 10355–10358.

(68) Williams, S. T.; Zuo, F.; Chueh, C. C.; Liao, C. Y.; Liang, P. W.; Jen, A. K. Y. Role of Chloride in the Morphological Evolution of Organo-Lead Halide Perovskite Thin Films. *ACS Nano* **2014**, *8*, 10640–10654.

(69) Persson, I.; Lyczko, K.; Lundberg, D.; Eriksson, L.; Płaczek, A. Coordination Chemistry Study of Hydrated and Solvated Lead(II) Ions in Solution and Solid State. *Inorg. Chem.* **2011**, *50*, 1058–1072.

(70) Wakamiya, A.; Endo, M.; Sasamori, T.; Tokitoh, N.; Ogomi, Y.; Hayase, S.; Murata, Y. Reproducible Frabrication of Efficient Perovskite-Based Solar Cells: X-Ray Crystallographic Studies on the Formation of $CH_3NH_3PbI_3$ Layers. *Chem. Lett.* **2014**, *43*, 711–713.

(71) Hao, F.; Stoumpos, C. C.; Liu, Z.; Chang, R. P. H.; Kanatzidis, M. G. Controllable Perovskite Crystallization at a Gas-Solid Interface for Hole Conductor-Free Solar Cells with Steady Power Conversion Efficiency over 10%. *J. Am. Chem. Soc.* **2014**, *136*, 16411–16419.

(72) Glasser, L. Lattice Energies of Crystals with Multiple Ions: A Generalized Kapustinskii Equation. *Inorg. Chem.* **1995**, *34*, 4935–4936.

(73) Gil-Escrig, L.; Miquel-Sempere, A.; Sessolo, M.; Bolink, H. J. Mixed Iodide-Bromide Methylammonium Lead Perovskite-Based Diodes for Light Emission and Photovoltaics. *J. Phys. Chem. Lett.* **2015,** *6*, 3743–3748.

(74) Stranks, S. D.; Snaith, H. J. Metal-Halide Perovskites for Photovoltaic and Light-Emitting Devices. *Nat. Nanotechnol.* **2015,** *10*, 391–402.

Supporting Information

Table S1. Polycrystalline mixed halide perovskites.

Loading	a (nm)	XRD size (nm)	Abs. edge (nm)	PL max (nm)
100% I 0% Br	0.628	> 100	765	763
75% I 25% Br	0.612	58	647	663
50% I 50% Br	0.594	> 100	532	576
25% I 75% Br	0.594	> 100	523	530
0% I 100% Br	0.591	> 100	527	519
100%Br 0% Cl	0.598	72	526	527
75%Br 25% Cl	0.588	> 100	488	498
50%Br 50% Cl	0.581	> 100	466	466
25%Br 75% Cl	0.579	> 100	430	438
0%Br 100%Cl	0.572	> 100	399	412

Table S2. Low dimensional mixed halide perovskites.

Loading	a (nm)	XRD size (nm)	TEM size (nm)	Abs. edge (nm)	PL max (nm)	Quantum Yield (%)
100% I 0% Br	0.634	> 100	7 ± 2	774	745	1.5
75% I 25% Br	0.608	> 100	4 ± 1	630	644	1.3
50% I 50% Br	0.599	> 100	8 ± 3	560	540	0.02
25% I 75% Br	0.591	> 100	15 ± 6	529	515	0.2
0% I 100% Br	0.587	7	8 ± 2	527	506	44
100%Br 0% Cl	0.596	86	164 ± 170 (sheet)	515	518	5
75%Br 25% Cl	0.582	18	20 ± 9 (plate)	486	497	3
50%Br 50% Cl	0.579	40	10 ± 3	449	459	3
25%Br 75% Cl	0.569	10	10 ± 5	412	423	0.3
0%Br 100%Cl	0.567	14	9 ± 3	387	398	0.03

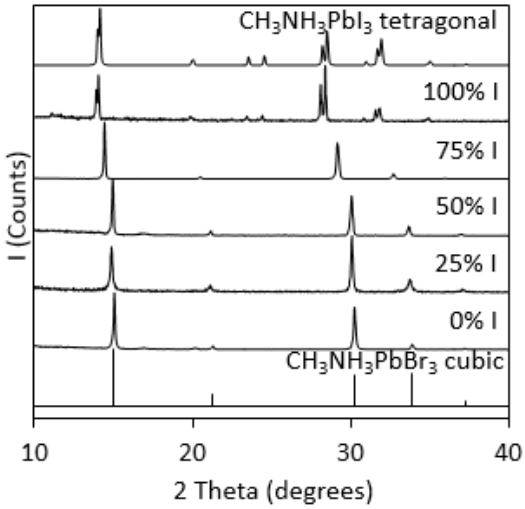

Figure S1. Powder XRD of experimental polycrystalline mixed Br-I perovskites $CH_3NH_3Pb(Br_xI_{1-x})_3$. The standard XRD patterns of cubic $CH_3NH_3PbBr_3$ (bottom) and tetragonal $CH_3NH_3PbI_3$ (top) are also shown.

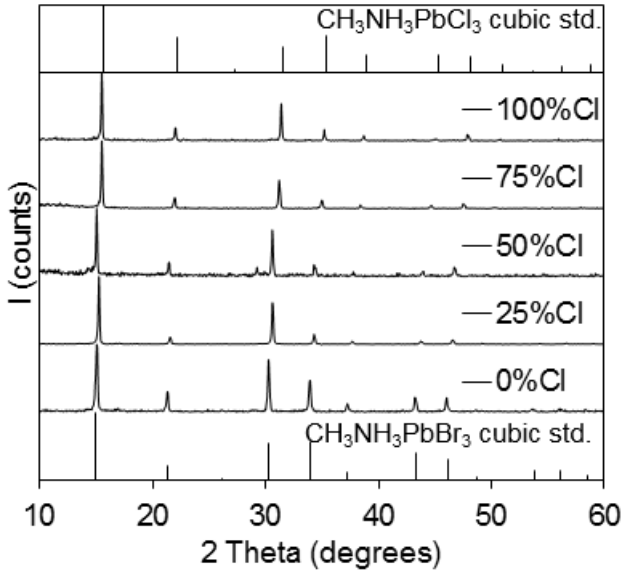

Figure S2. Powder XRD of experimental polycrystalline mixed Cl-Br perovskites $CH_3NH_3Pb(Cl_xBr_{1-x})_3$. The standard XRD patterns of cubic $CH_3NH_3PbCl_3$ (top) and cubic $CH_3NH_3PbBr_3$ (bottom) are also shown.

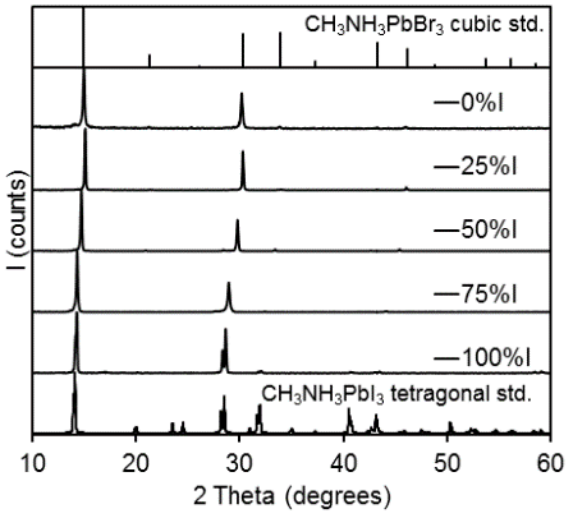

Figure S3. Powder XRD of experimental low dimensional mixed Br-I perovskites $CH_3NH_3Pb(Br_xI_{1-x})_3$. The standard XRD patterns of cubic $CH_3NH_3PbBr_3$ (top) and tetragonal $CH_3NH_3PbI_3$ (bottom) are also shown.

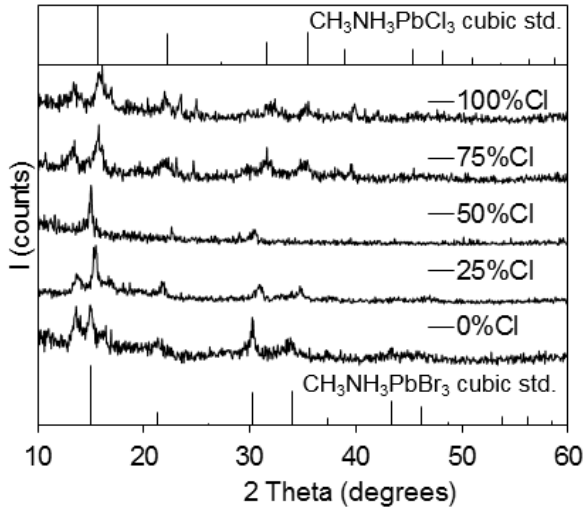

Figure S4. Powder XRD of experimental low dimensional mixed Cl-Br perovskites $CH_3NH_3Pb(Cl_xBr_{1-x})_3$. The standard XRD patterns of cubic $CH_3NH_3PbCl_3$ (top) and cubic $CH_3NH_3PbBr_3$ (bottom) are also shown.

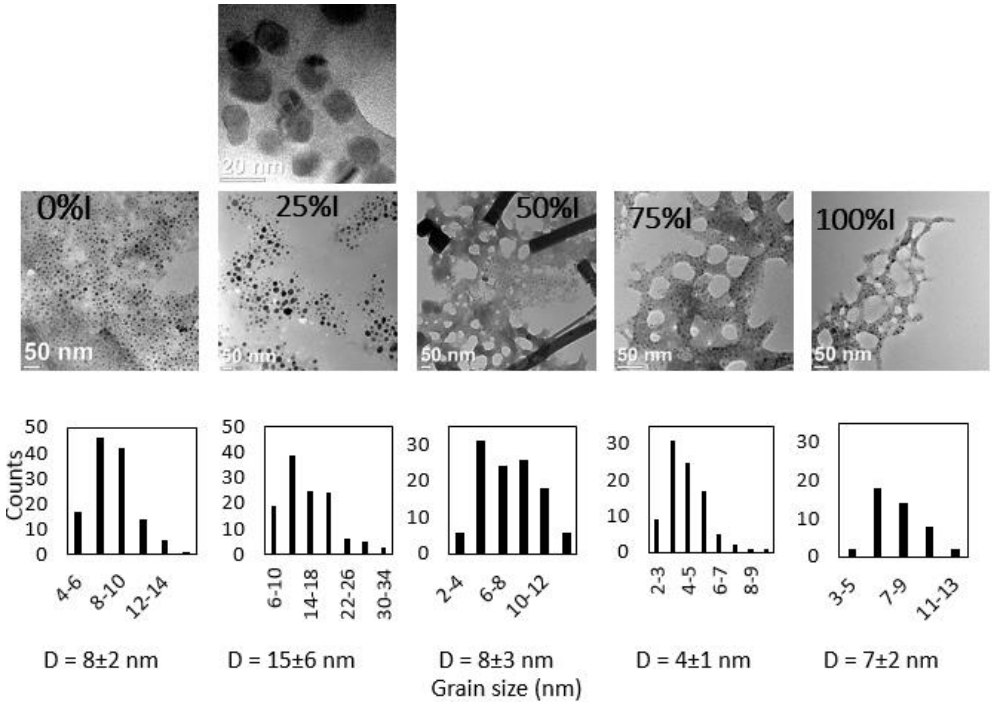

Figure S5. Typical TEM images of low dimensional mixed Br-I perovskites $CH_3NH_3Pb(Br_xI_{1-x})_3$ and their size distribution histograms obtained from TEM data. An HRTEM image of 25% I 75% Br perovskite is also shown.

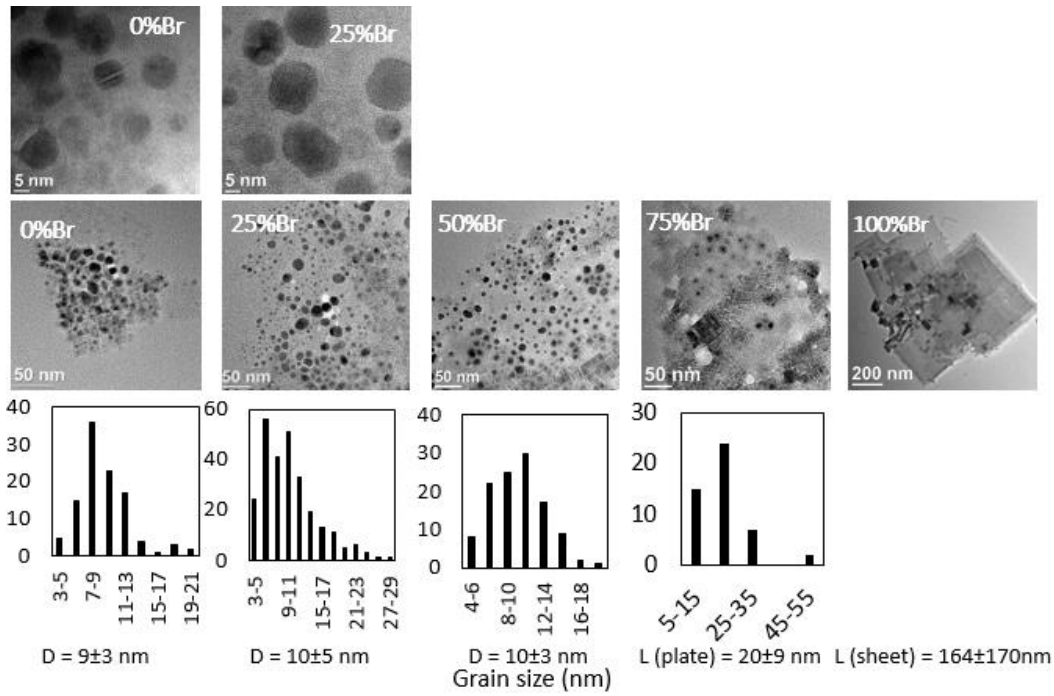

Figure S6. Typical TEM images of low dimensional mixed Cl-Br perovskites $CH_3NH_3Pb(Cl_xBr_{1-x})_3$ and their size distribution histograms obtained from TEM data. HRTEM images of 0%Br and 25%Br are also shown.

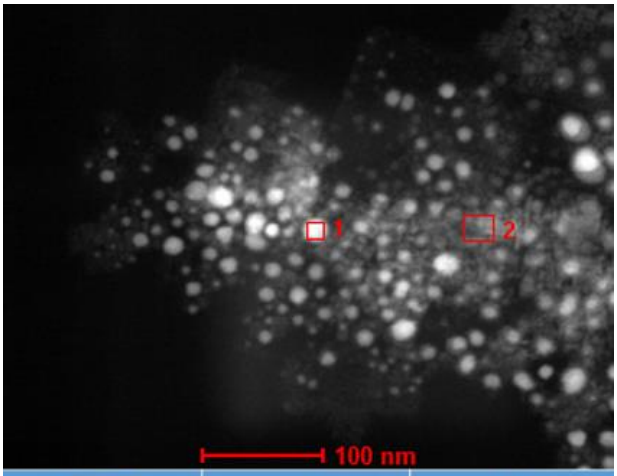

Region	1	2
Cl (Atomic %)	40	45
Br (Atomic %)	60	55

Figure S7. A typical STEM image of low dimensional 50%Br 50%Cl perovskites and their halide composition at different regions obtained from EDX data.

CHAPTER 3. ALIOVALENT DOPING OF LEAD HALIDE PEROVSKITES: EXPLORING THE $CH_3NH_3PbI_3$–$(CH_3NH_3)_3Sb_2I_9$ INTERFACE TOWARD ALL INORGANIC PEROVSKITES

Feng Zhu, Noreen E. Gentry, Long Men, Miles A. White, Javier Vela

Abstract

Lead halide perovskites have attracted much attention in the past few years due to their outstanding performance in photovoltaic devices. Nanoscale versions of these materials are also good candidates for light emitting devices. In this work, we synthesize perovskite nanocrystals using a surfactant-free method by introducing antimony iodide in the perovskite precursor. Surface-bound $(CH_3)_3Sb_2I_9$ layers restrict the growth of $CH_3NH_3PbI_3$, resulting in $CH_3NH_3PbI_3$ nanocrystals of about 50 nm. Compared to the bulk perovskites, the nanocrystals show stronger photoluminescence. As there are no long-chain organic ligands on the surface which will inhibit the charge (electron and hole) transport, these surfactant-free nanocrystals may have better performance in the photo-electronic devices.

Introduction

Organometal halide perovskites of general composition $APbX_3$ (A = $CH_3NH_3^+$, $H_2N\text{-}CH{=}NH_2^+$, Cs^+; X = I^-, Br^-, Cl^-) are attractive semiconducting materials due to their outstanding photovoltaic performance in both planar heterojunction and mesoporous solar cells.[1-4] Specific device performance heavily depends on perovskite composition, crystallinity, and morphology.[5,6] Substitution with a variety of small organic and inorganic cations (A, above), main group metals (Sn or Ge, in lieau of Pb), and halides (X) results in 'hybrid' perovskites with—in some cases—greatly enhanced performance.[7-12] Films made of well-crystallized perovskites display wide light absorption, high absorption coefficients, and long electron-hole carrier diffusion lengths.[13] Optimization of these properties has led to an increase in power conversion efficiency (PCE) from 3% to 22.1% in recent years.[14]

Large crystallites present a small band gap and long lifetime, which correlate to a small recombination coefficient and high conversion efficiency.[15] However, small $CH_3NH_3PbX_3$ nanocrystals show excellent photoluminescence quantum yields of up to 70% at room temperature and are good candidates for light-emitting devices.[16-19] Most of these fluorescent nanocrystals are prepared using organic ligands to control the crystal morphology, passivate the halide-rich surface, and thus improve the PL intensity.[20] Our group employed n-octylammonium halides to partially replace $CH_3NH_3^+$, and terminate the crystal growth in the synthesis of $CH_3NH_3PbX_3$ nanorods and nanoplates or sheets. $CH_3NH_3PbX_3$ nanoparticles display relatively stable and shape correlated photoluminescence at the single particle level.[21-24] An adverse effect of organic ligands is they form an insulated layer and restrict the carrier transport.[25] There are only a few papers reporting methods to synthesize nano-sized perovskites without organic ligands, including using solvents with different polarities,[26] employing lead halide and other Pb-containing precursors as self-template,[27-29] or creating an organic matrix to control the particle size.[30, 31] $CH_3NH_3PbI_3$ nanowires can be synthesized in a low temperature, solution processed crystallization, using a simple slip-coating method.[32]

Inorganic ligands, such as metal chalcogenide complexes, chalcogenide ions, and halide or pseudohalides, are always used to replace the organic ligands on the semiconductor surface. These all-inorganic nanocrystal films show improved charge transport capability compared with the organics capped ones.[33-39] As expected, the photovoltaic devices show improved conversion efficiency.[40, 41] Photovoltaic devices using inorganic passivated lead chalcogenide nanocrystals also have better air stability and retain performance characteristics for long time.[42,43] Moreover, the inorganic-capped crystals perform well in other fields, including water oxidation, photoluminescence, and electroncatalysis.[44-46] II–VI, III–V, and IV–VI, semiconductor nanocrystals capped with

lead halide perovskites ($CH_3NH_3PbX_3$, where X = I, Br) and other metal halide complexes (MXn, where M = Pb, Cd, In, Zn, Fe, Bi, Sb) show high luminescence quantum efficiencies at different wavelengths.[47] InP nanocrystals capped with chalcogenide complexes have relatively stable PL emission in elevated temperatures.[48]

In this paper, we synthesize and characterize $CH_3NH_3PbI_3$ nanocrystals, using organo-antimony halide as the capping agent instead of organic ligands. $(CH_3NH_3)_3Sb_2I_9$ gives two modifications from the three-dimensional (3D) $CH_3NH_3PbI_3$ perovskite structure: (1) two-dimensional (2D) corrugated layer of polyanions and (2) isolated bioctahedral $M_2X_9^{3-}$ anion.[49-55] By replacing Pb^{2+} with Sb^{3+} on the $CH_3NH_3PbI_3$ surface, large 2D layers generate and terminate the organo-lead halide crystal growth. These nanocrystals show improved PL emission over the bulk material.

Experimental

Materials. Lead(II) iodide (99%), antimony(III) iodide (98%), methylamine solution (33 wt %), 2,2′,7,7′-tetrakis(N,N-di-p-methoxyphenylamine)-9,9-spirobifluorene) (72.3 mg, spiro-MeOTAD), lithium bis(trifluoromethylsulphonyl)imide, and tris(2-(1H-pyrazol-1-yl)-4-tert-butylpyridine)cobalt(III) bis(trifluoromethylsulphonyl)imide were purchased from Sigma-Aldrich; hydroiodic acid (ACS, 55-58%) and oleic acid (tech., 90%) from Alfa-Aesar; acetonitrile (99.9%), and toluene (99.9%) from Fisher. All chemicals were used as received.

Synthesis. *Ammonium halides.* Hydroiodic acid (10 mL, 0.075 mol) was added to a solution of excess amine (0.192 mol) in ethanol (100 mL) at 0 °C, and the mixture stirred for 2 h. The solution was concentrated under vacuum, and the resulting powder dried under dynamic vacuum at 60 °C for 12 h and recrystallized from ethanol. *n*-Octylammonium iodide ($CH_3(CH_2)_7NH_3I$) was washed repeatedly with ethyl ether and dried under dynamic vacuum. *$(CH_3NH_3)_3Sb_2I_9$.* Solution A: SbI_3 (5.0 mg, 0.01 mmol) and CH_3NH_3I (4.8 mg,

0.03 mmol) were dissolved in acetonitrile (20 mL). A fraction of this solution (4 mL) was dropped into toluene (15 mL) under stirring. The orange product was centrifuged without sonication and washed with toluene. *Organic (C8) capping*. Solution B: SbI_3 (5.0 mg, 0.01 mmol), CH_3NH_3I (2.4 mg, 0.015 mmol) and $CH_3(CH_2)_7NH_3I$ (3.9 mg, 0.015 mmol) were dissolved in acetonitrile (20 mL). Octylammonium-capped $(CH_3NH_3)_3Sb_2I_9$ nanocrystals were synthesized by a similar procedure to the one above. $CH_3NH_3PbI_3$. Solution C: PbI_2 (9.2 mg, 0.02 mmol) and CH_3NH_3I (9.6 mg, 0.06 mmol) were dissolved in acetonitrile (40 mL). Solution D: PbI_2 (9.2 mg, 0.02 mmol), CH_3NH_3I (4.8 mg, 0.03 mmol) and $CH_3(CH_2)_7NH_3I$ (7.8 mg, 0.03 mmol) were dissolved in acetonitrile (40 mL). *Inorganic (Sb) capping.* Different amounts of solution C were mixed with solution A (4 mL in total, 0.002 mmol), and the mixture added into toluene (15 mL) under stirring. *Combined organic and inorganic capping.* Different amounts of solution D were mixed with solution A (4 mL, 0.002 mmol), and the mixture added into toluene (15 mL). In all cases, samples were stirred for 6 h before isolating the product by centrifugation (10 min at 4,500 rpm), following by re-dispersion in toluene (5 mL).

Structural Characterization. *Powder X-ray diffraction* (XRD) data were measured using Cu Kα radiation on Rigaku Ultima IV (40 kV, 44 mA). Samples were measured on a "background-less" quartz slide. *Transmission electron microscopy* (TEM) was conducted using a FEI Technai G2 F20 field emission TEM operating at up to 200 kV with a point-to-point resolution of less than 0.25 nm and a line-to-line resolution of less than 0.10 nm. Dilute sample solutions in toluene were dropped (2-3 drops) onto carbon-coated copper grids. Elemental composition was assessed by energy-dispersive spectroscopy (EDS).

Optical Characterization. *Optical extinction* (absorption plus scattering) spectra of solutions were measured with a photodiode-array Agilent 8453 UV/vis

spectrophotometer. Solvent absorption was recorded and subtracted from all spectra. *Diffuse reflectance* spectra of solid films were measured with a SL1 Tungsten Halogen lamp (vis-IR), a SL3 Deuterium Lamp (UV), and a BLACK-Comet C-SR-100 Spectrometer. Samples were prepared by drop-casting toluene solutions onto glass. *Steady-state photoluminescence* (PL) spectra were measured with a Horiba-Jobin Yvon Nanolog scanning spectrofluorometer equipped with a photomultiplier detector. Relative PL quantum yields (QYs) were measured against using Rhodamine 640 dye using standard procedures.

Solar cell device fabrication. *FTO glass cleaning*. Substrates were cleaned with a 2% solution of Hellmanex® cuvette cleaning detergent diluted in deionized water, rinsed with deionized water, acetone and ethanol, and dried with clean dry air. Oxygen plasma was then used to treat the substrate for 10 min.[56] *TiO_2 block layer*. The TiO_x flat film precursor solution consists of 0.23 M titanium isopropoxide and 0.013 M HCl in isopropanol. FTO substrates were coated with a compact layer of TiO_2 deposited by spin coating this TiO_x solution at 2000 rpm for 60 s and consequently heating at 500 °C for 30 min.[57] *TiO_2 porous layer*. A mesoporous TiO_2 layer composed of 20 nm-sized particles was deposited by spin coating at 5000 rpm for 30 s using a commercial TiO_2 paste (Dyesol 18NRT, Dyesol) diluted in ethanol (2:7, weight ratio). After drying at 125 °C, the TiO_2 films were gradually heated to 500 °C, baked at this temperature for 15 min and cooled to room temperature. Prior to use, the films were re-dried at 500 °C for 30 min.[58] *Perovskite layer (two-step deposition).* PbI_2 (1 M) with varying molar ratios of SbI_3 in DMF was spin coated onto the mesoporous TiO_2 at 6500 rpm for 30 s and dried at 70 ˚C. PbI_2 deposition repeated in order to ensure loading of the mesoporous structure. The perovskite layer was formed after drop casting CH_3NH_3I solution (0.2 mL, concentration?) in isopropanol (8 mg mL1?), waiting 20 s, and spin coating for 20 s at 4000 rpm. Substrates were dried at 70 ˚C.

Hole transport material (HTM) layer. Spiro-MeOTAD (72.3 mg), 4-tert-butylpyridine (28.8 μL), lithium bis(trifluoromethylsulphonyl)imide (17.5 μL of 520 mg/mL solution in acetonitrile) and tris(2-(1H-pyrazol-1-yl)-4-tert-butylpyridine)cobalt(III) bis(trifluoromethylsulphonyl)imide (29 μL of a 300 mg/mL solution in acetonitrile) were mixed with chlorobenzene (1 mL). The HTM was deposited by spin coating this solution at 4000 rpm for 30 s. *Current density–voltage (I-V) characterization.* One sun illumination was obtained using a light source (LS150 Abet Technologies) and calibrated with a reference crystalline Si solar cell. All the samples were measured under the same light intensity. The I-V curve was measured using a Keithley 2400 source-meter.

Results and Discussion

As highlighted in our original synthesis of lead perovskite nanocrystals,[21] one way to prepare these materials is by exploiting solvent polarity differences. CH_3NH_3X and PbX_2 precursors dissolved in a polar solvent—such as acetonitrile—quickly react upon exposure to less polar solvents—such as toluene—to form $CH_3NH_3PbX_3$ (X = I, Br, Cl) solids, which are easy to isolate by precipitation.[23] Addition of a surface truncating agent that does not fit within their structure—such as a long chain ammonium halide[21] or a long chain carboxylate—leads to size controlled perovskite nanoparticles capped and stabilized by surface-bound organic ligands.

We have adapted this general method to the synthesis of $(CH_3NH_3)_3Sb_2I_9$ (Scheme 1). Addition of excess toluene to an acetonitrile solution of SbI_3 and CH_3NH_3I causes the formation of an orange precipitate. Powder X-ray diffraction (XRD) of this solid shows that it contains crystalline $(CH_3NH_3)_3Sb_2I_9$ in its trigonal phase (Figure 1), although the product has relatively intense (-111), (011), (-231), and (-131) peaks compared to the standard pattern.

Scheme 1.

$$x\ SbI_3 + y\ CH_3NH_3I + z\ n\text{-}C_8H_{17}NH_3I \xrightarrow[(2)\ Toluene]{(1)\ CH_3CN} (CH_3NH_3)_3Sb_2I_9 \quad \text{(unbalanced)}$$

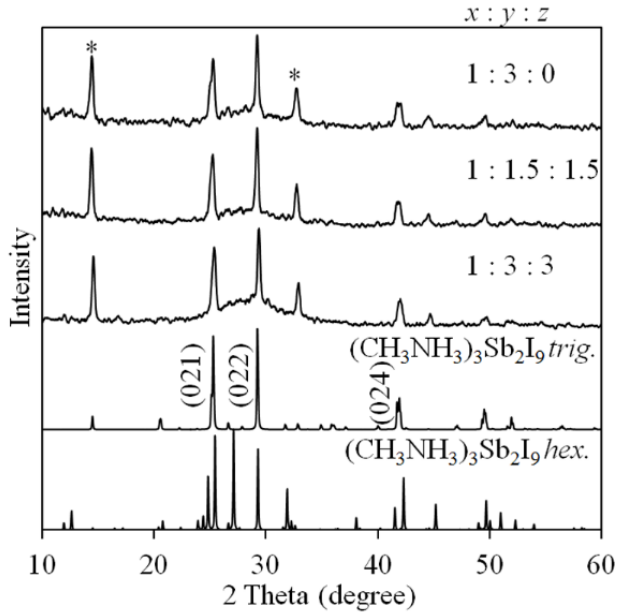

Figure 1. Powder XRD of $(CH_3NH_3)_3Sb_2I_9$ prepared with and without different amounts of n-$C_8H_{17}NH_3I$ as a capping agent. The x, y and z labels show the relative molar loadings of SbI_3, CH_3NH_3I and n-$C_8H_{17}NH_3I$.

$CH_3NH_3PbX_3$ perovskites form a 3D structure of corner sharing hexahalolead(II) octahedra [PbX_6^{4-}], and monovalent cations (A^+) opposing each of the octahedral faces in 12-fold cuboctahedral coordination. (Figure 1). There are two known structures for this compound, trigonal and hexagonal which contain isolated and face-sharing [PbX_6^{4-}] octahedra, which both. The organo-antimony halide, $(CH_3NH_3)_3Sb_2I_9$ forms 2D layers of polyanions in the crystal structure similar to the perovskite structure (Figure 1), with Sb also surrounded by 6 halide atoms. Since $CH_3NH_3PbI_3$ and $(CH_3NH_3)_3Sb_2I_9$ can generate

in the same solvent with a similar growth rate during precursor injection, layered $(CH_3NH_3)_3Sb_2I_9$ may cover the $CH_3NH_3PbI_3$ surface, leading to size-controlled crystals.

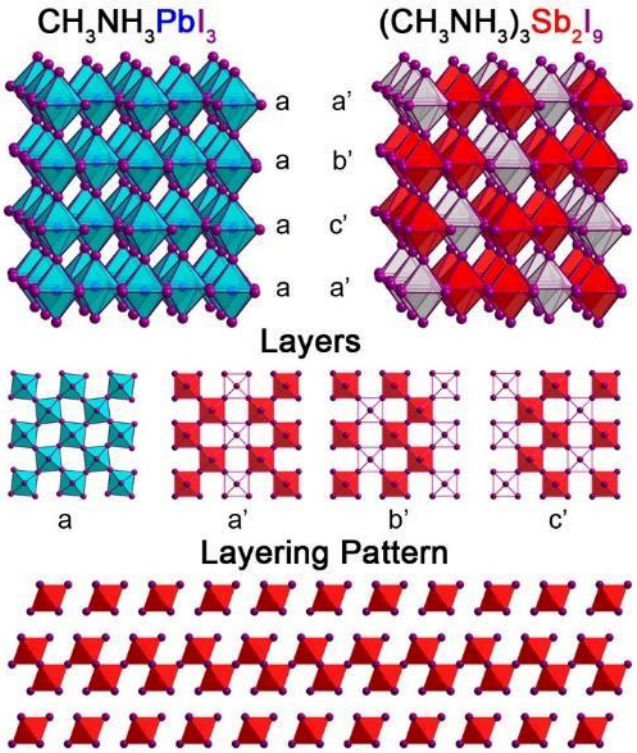

Figure 2. Unit cells of $CH_3NH_3PbI_3$ (left) and $(CH_3NH_3)_3Sb_2I_9$ (right) and the layering patterns of each perovskite. Vacant octahedra are depicted in gray for the Sb perovskite.

When the bulky n-$C_8H_{17}NH_3I$ ligand is introduced to partially replace CH_3NH_3I, XRD patterns show minor differences in either peak intensities or widths, indicating little change in morphology and size (Figure 2). Transmission Electron Microscopy (TEM) confirms this finding and shows the similar morphology of network between the system with and without n-$C_8H_{17}NH_3I$ (Figure 3). Absorption spectra measured from solution transmittance and powder diffuse reflectance show the absorption onset at about 640 nm (Figure 4).

$(CH_3NH_3)_3Sb_2I_9$ crystals remain relatively stable with dispersion in toluene, however the product is unstable if left stirring in the crude solution. During this decomposition, a significantly less yellow product replaces the orange crystals and can be

collected utilizing centrifuge. This decomposition gives a very broad XRD peak at about 29° (Figure S2) which can be attributed to weak van der Waals force between the layers in $(CH_3NH_3)_3Sb_2I_9$.

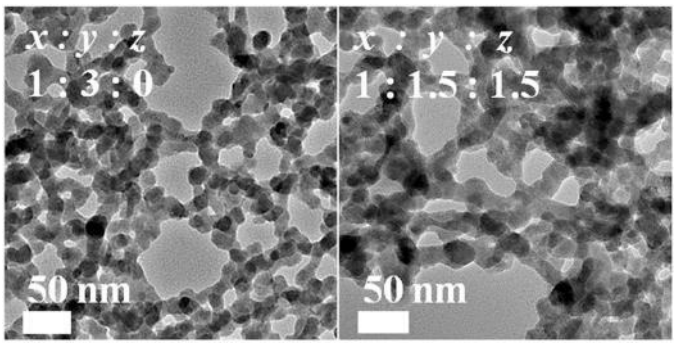

Figure 3. TEM of $(CH_3NH_3)_3Sb_2I_9$ prepared with different precursor ratios of SbI_3 (x), CH_3NH_3I (y) and n-$C_8H_{17}NH_3I$ (z).

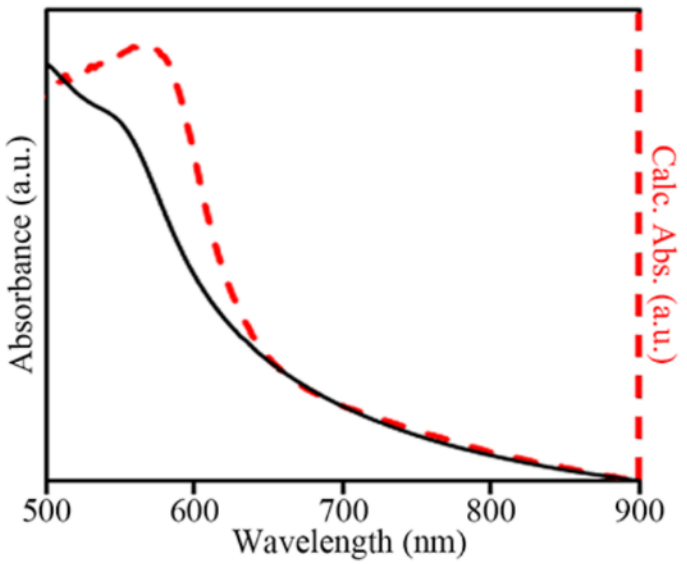

Figure 4. Absorption spectra of $(CH_3NH_3)_3Sb_2I_9$ measured from solution transmittance (red) and powder diffuse reflectance (black).

To prepare the $CH_3NH_3PbI_3$ perovskite, we repeated the procedure outlined above using PbI_2. SbI_3 was introduced into the system in various ratios to terminate particle growth without binding long-chain organic ligands to the surface of the particles. The initial concentrations of metal halide and CH_3NH_3I were preserved (Scheme 2). XRD peaks of

the doped Sb-Pb perovskites maintain the same pattern as the pure $CH_3NH_3PbI_3$ phase, even when the Sb^{3+} concentration is as high as 40% (x = 0.4) (Figure 5). No horizontal XRD peak shifts are observed in the Sb-Pb perovskite, either, suggesting the Sb does not fully incorporate into the crystal structure, but rather forms some sort of surface coating. The absence of XRD shifting can possibly be attributed to very thin layers of $(CH_3NH_3)_3Sb_2I_9$ covering the $CH_3NH_3PbI_3$ surface while stirring, which cannot be detected by XRD. While the structure of the perovskites appears resistant to Sb^{3+} doping, an increase in the XRD peak width is observed, indicating a reduction in crystal size with the addition of Sb^{3+}. $CH_3NH_3PbI_3$ formed in solution without SbI_3 (x = 0) has a relatively strong peaks of (002) and (004) compared to the standard powder XRD pattern; this is likely attributed to the preferred growth or packing orientation of the crystals. Products with Sb show consistent peak intensities compared to the synthesized standard, indicating the spherical morphology or isotropic packing of the crystals.

Scheme 2.

$$(1\text{-}x)\ PbI_2 + x\ SbI_3 + 3\ CH_3NH_3I \xrightarrow[(2)\ \text{Toluene}]{(1)\ CH_3CN} \text{product}$$

We further identify the hybrid crystal size using TEM. “Bulk” $CH_3NH_3PbI_3$, made in the absence of SbI_3 (x = 0), consists of relatively large 0.3-2 μm particles with cube-like or tetragonal morphology (Figure 6). In contrast, $CH_3NH_3PbI_3$ produced with the addition of SbI_3 consists of nanocrystals with an average diameter of 49 and 44nm for the 20% (x = 0.2) and 40% Sb crystals, respectively (Table 1). High-resolution transmission electron microscopy (HR-TEM) of the 20% Sb-doped perovskite shows the presence of three prominent d-spacing values of 3.0, 3.2, and 3.5 Å. The 3.2 Å lattice plane can be readily assigned to the (220) plane of $CH_3NH_3PbI_3$, while the 3.0 and 3.5 Å d-spacings correspond

to the (20-2) and (201) planes of $(CH_3NH_3)_3Sb_2I_9$, respectively (Table S1). Furthermore, the 40% Sb-doped products show layered materials surrounding the particles.

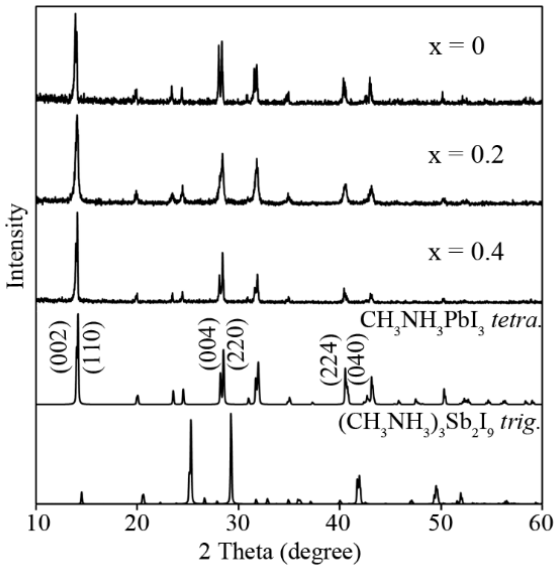

Figure 5. XRD patterns for $CH_3NH_3PbI_3$ prepared using different initial concentrations of PbI_2 (0.435·(1-*x*) mM), SbI_3 (0.435·*x* mM) and CH_3NH_3I (1.305 mM) in acetonitrile precursor solution and crashed with toluene according to Scheme 2. The standard XRD pattern reported for $CH_3NH_3PbI_3$ *I*4*cm* and $(CH_3NH_3)_3Sb_2I_9$ are shown for comparison.

Elemental mapping and composition analysis of Sb-doped perovskites by energy dispersive X-ray spectroscopy (EDX) in Figure 7 confirmed the presence of all three Pb, Sb, and I elements in 20% and 40% Sb-doped samples. Pb-containing products appear to maintain separate particles, while Sb are distributed over a wide area, indicating that organo-antimony halide formed layered products is layered over the surface of the $CH_3NH_3PbI_3$ particles. A line profile of the 20% and 40% doped samples (Figure 8) indicates a homogenous doping of the perovskites. Following a cross section, each elemental count appears to remain relatively consistent.

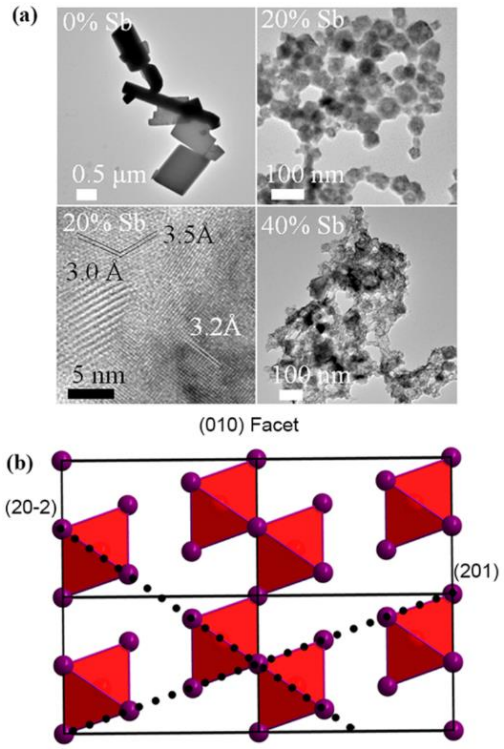

Figure 6. Representative TEM images (a) for $CH_3NH_3PbI_3$ crystals with 0, 20, and 40% Sb doping. The (010) facet (b) shows the lattice spacing of the 20% Sb-doped crystals on the (20-2) and (201) planes.

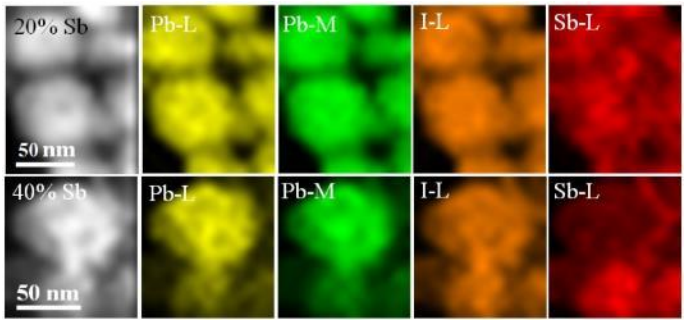

Figure 7. Elemental mapping of 20% (top) and 40% (bottom) Sb-doped perovskites by energy dispersive X-ray spectroscopy (EDX).

An interesting characteristic of organometal perovskite semiconductors is they can be highly emissive and are good fluorophores. Because structural defects are known to play a crucial role in perovskite's optical properties, non-radiative recombination could be attributed to surface defects. In agreement with this idea, nanostructured organolead halide

perovskites capped with organic ligands exhibit high PL quantum yields and have been used in light-emitting devices. Organo-antimony halide covered on the surface may also inhibit the non-radiative recombination path, enhancing the emission intensity.

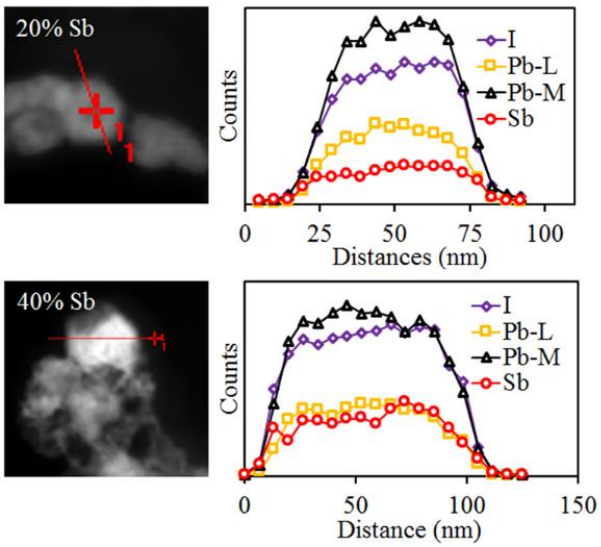

Figure 8. Line scanning analysis of perovskites with different amount of Sb. An overall homogenous doping across the plane is observed.

The optical properties of the inorganic capped perovskites were tested to explore this idea. The solution-phase optical absorption, solid-film diffuse reflectance, and photoluminescence spectra of several Sb-doped $CH_3NH_3PbI_3$ perovskites are shown in Figure 9. The solution-phase spectra show weak excitonic peaks in Sb-doped $CH_3NH_3PbI_3$ at about 735 nm. Due to partial or incomplete solubility (particularly for large and bulk particles), solution-phase absorption spectra of these materials show a significant amount of scattering at photon energies below their band gap (Figures 9a). The diffuse reflectance spectra (Figures 9b) are particularly helpful in determining the absorption onsets of these materials. As expected, bulk $CH_3NH_3PbI_3$shows absorption onset of about 800 nm (Figures 9b) while the absorption edge is blue shifted for 20% Sb-doped sample and red shifted in 40% doped sample (Table 1). The specific apparent band gaps, measured from the

absorption data using Tauc plots ($(\alpha h\nu)^2$ vs. hν for a direct band-gap semiconductor, where A = absorption coefficient, hν = energy of light) were the following: 1.56 eV for bulk $CH_3NH_3PbI_3$, 1.58 eV for 20% Sb- $CH_3NH_3PbI_3$, and 1.57 eV for 40% Sb- $CH_3NH_3PbI_3$. The PL peak (Figure 9c) also experiences a significant blue shift with the addition of 20% and 40% Sb doping. Bulk $CH_3NH_3PbI_3$ have very weak PL emission and exhibit a PL peak at 778 nm while 20% and 40% doped crystals have stronger emission peaks at 745 nm and 757 nm respectively. $CH_3NH_3PbI_3$ nanocrystals made in the presence of SbI_3 in precursor tend to have higher PL QYs.

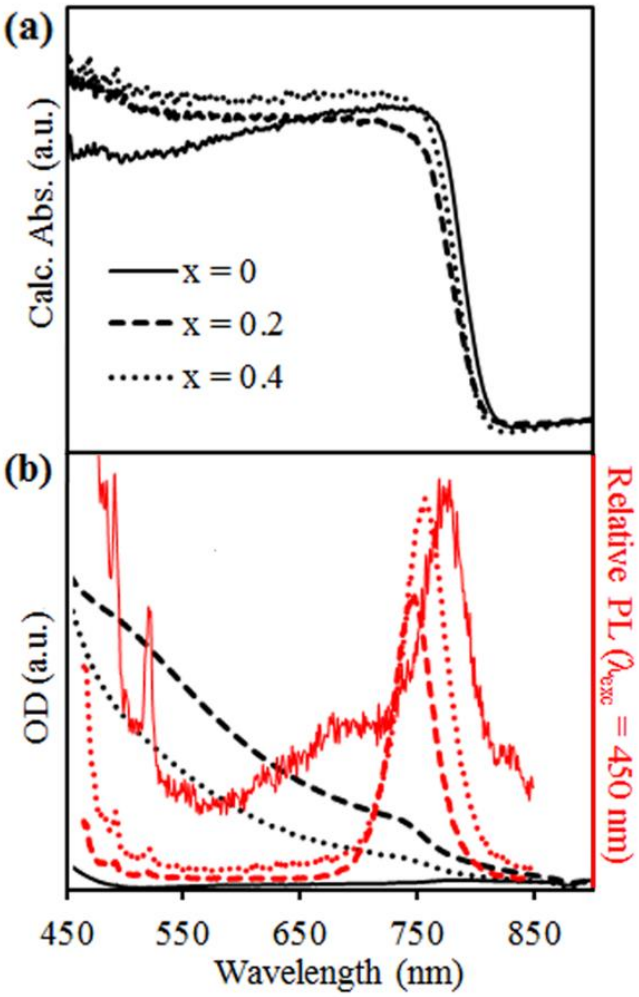

Figure 9. Solution-phase optical density (O.D. includes absorption and scattering) (a), solid-film diffuse reflectance (b), and relative photoluminescence spectra (normalized by each sample's O.D. at λ_{exc} = 450 nm) (c) of Sb-Pb perovskites with different Sb ratio.

To further study the effects of ligands and morphology control, n-$C_8H_{17}NH_3I$ and SbI_3 are both introduced for the preparation $CH_3NH_3PbI_3$, as shown in Scheme 3. Similar to the doping procedure outlined above, CH_3NH_3I and n-$C_8H_{17}NH_3I$ are both added in excess to the precursors, while PbI_2 and SbI_3 ratios are changed coordinately to maintain a constant molar ratio to the other reagents. XRD patterns of products prepared from different ratio of SbI_3 match the $CH_3NH_3PbI_3$ peaks, without any peaks from organo-Sb halide phase present, as shown in Figure 10. XRD peaks also indicate SbI_3 in the precursor may weaken the crystal growth orientation, because the samples with SbI_3 have more intense XRD peaks beyond 30 degrees than the perovskite without SbI_3, which correlates stronger to the standard pattern.

Scheme 3.

$$(1\text{-}x)\ PbI_2 + x\ SbI_3 + 1.5\ CH_3NH_3I + 1.5\ \text{n-}C_8H_{17}NH_3I \xrightarrow[(2)\ \text{Toluene}]{(1)\ CH_3CN} \text{product}$$

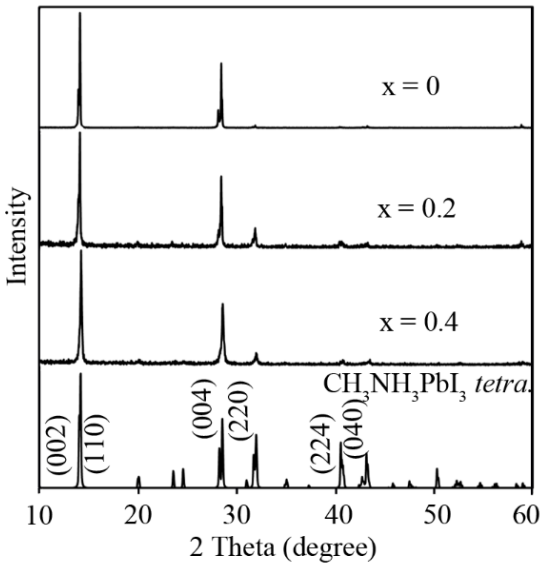

Figure 10. XRD patterns for $CH_3NH_3PbI_3$ prepared using different initial concentrations of PbI_2 (0.435·(1-*x*) mM), SbI_3 (0.435·*x* mM) in presence of CH_3NH_3I and n-$C_8H_{17}NH_3I$ according to Scheme 3.

TEM images (Figure 11) are consistent with our previous publication and show the product with only n-$C_8H_{17}NH_3I$ (x= 0, 0% Sb) forms primarily nanowires and a small distribution of nanocrystals (Figure 11). The addition of SbI_3 in the precursor solution containing n-$C_8H_{17}NH_3I$ adjusts preferred morphology with various doping levels. The 20% Sb perovskite becomes predominantly nanocrystals with a few short rods still present, while the 40% Sb perovskite produces only nanocrystals without nanorods or nanowires apparent. In the presence of n-$C_8H_{17}NH_3I$, nanoparticles are produced with 0%, 20% and 40% Sb doping with diameters of 17, 28, and 21nm respectively (Table 1).

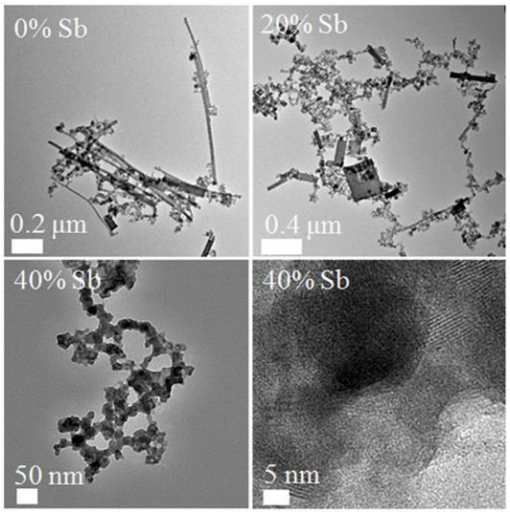

Figure 11. Representative TEM images and size histograms for $CH_3NH_3PbI_3$ crystals with different ratio of Sb doping in presence of n-$C_8H_{17}NH_3I$.

The optical characterizations of these perovskites is shown in Figure 12. The solution phase absorption spectra (Figure 12a) shows a significant change for the 40% perovskite, which is replicated with a slight blue shift for both doped perovskites during diffuse reflectance (Figure 12b). Diffuse reflectance spectra show an absorption onset at about 785 nm, with the bandgap of 1.57 eV for the 0% and 20% doped perovskites, while the 40% has a 1.59 eV bandgap. PL emission shows a little red shift in the products with SbI_3. Contrary to the Sb-doped perovskites prepared without the bulky organic ligand, the

PL emission intensity decreases significantly with increased SbI_3 doping in presence of n-$C_8H_{17}NH_3I$ (Figure 12).

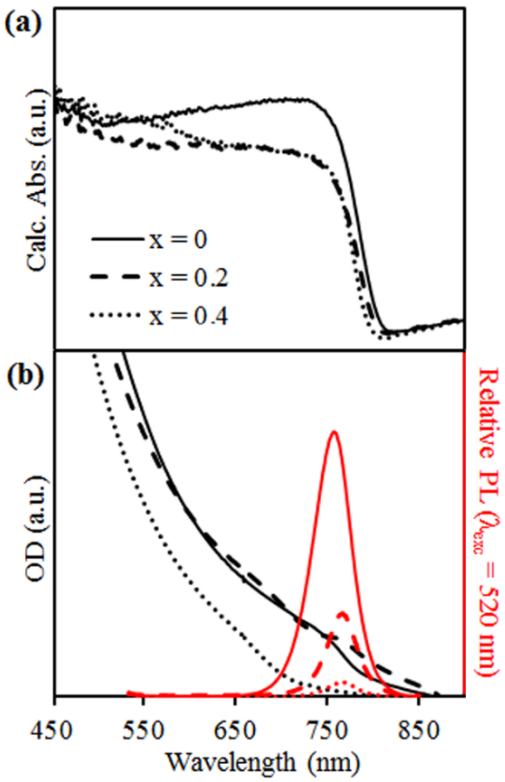

Figure 12. Solution-phase optical density (O.D. includes absorption and scattering) (a), solid-film diffuse reflectance (b), and relative photoluminescence spectra (normalized by each sample's O.D. at λ_{exc} = 520 nm) (c) of Sb-Pb perovskites with different Sb ratio in presence of n-$C_8H_{17}NH_3I$.

A single-junction solar cell was assembled, as outlined in the Experimental section, to distinguish the effects of Sb in devices. We dope SbI_3 (molar ratios of Sb to Pb 1%, 2%, 5%) into perovskite precursor to fabricate solar cell devices using a two-step deposition. The highest efficiency of single-junction solar cells is between 13 and 17%.[59, 60] As stated before, the Pb and Sb-Pb perovskites were spin coated from DMF solutions into the mesoporous TiO_2 layer. When the lead source is either PbI_2 or $PbCl_2$, after SbI_3 doping, the device fill factor will decrease when the SbI_3 amount is 1%. Further increasing SbI_3 will

decrease J_{SC} and V_{OC}. Films constructed using PbI_2 or $PbCl_2$ have higher conversion efficiency than the doped ones as shown in Figure S4.

Conclusion

In this manuscript, we successfully synthesize $CH_3NH_3PbI_3$ nanocrystals employing a surfactant-free method. Using a dissolve and polarity crash-out crystallization method, we produced $(CH_3)_3Sb_2I_9$ nanocrystals that remain stable in toluene solution. By introducing SbI_3 to partially replace PbI_2 in the precursor lead perovskite solution, layered $(CH_3)_3Sb_2I_9$ covers the surface of $CH_3NH_3PbI_3$ and terminates crystal growth during the crash-out process. The hybrid nanocrystals synthesized with $(CH_3)_3Sb_2I_9$ show higher PL quantum yield than bulk $CH_3NH_3PbI_3$. Nanocrystals prepared with only n-octylammonium have a higher PL intensity than those prepared in the presence of both n-octylammonium and $(CH_3)_3Sb_2I_9$. Nanocrystals prepared using $(CH_3)_3Sb_2I_9$ may be idealized in the photo-electronic devices, as no organic ligands are present on the perovskite surface that inhibit charge transport using the Sb film.

Acknowledgement

This research is supported by the U.S. Department of Energy, Office of Basic Energy Sciences, Division of Chemical Sciences, Geosciences, and Biosciences through the Ames Laboratory. The Ames Laboratory is operated for the U.S. Department of Energy by Iowa State University under Contract No. DE-AC02- 07CH11358.

References

(1) Saliba, M.; Matsui, T.; Seo, J.-Y.; Domanski, K.; Correa-Baena, J.-P.; Nazeeruddin, M. K.; Zakeeruddin, S. M.; Tress, W.; Abate, A.; Hagfeldt, A.; Gratzel, M. Cesium-Containing

Triple Cation Perovskite Solar Cells: Improved Stability, Reproducibility and High Efficiency. *Energy Environ. Sci.* **2016**, *9*, 1989–1997.

(2) Gao, P.; Grätzel, M.; Nazeeruddin, M. K. Organohalide Lead Perovskites for Photovoltaic Applications. *Energy Environ. Sci.* **2014**, *7*, 2448–2463.

(3) Green, M. A.; Ho-Baillie, A.; Snaith, H. J. The Emergence of Perovskite Solar Cells. *Nat. Photonics* **2014**, *8*, 506–514.

(4) Gratzel, M. The Light and Shade of Perovskite Solar Cells. *Nat. Mater.* **2014**, *13*, 838–842.

(5) Jeon, N. J.; Noh, J. H.; Yang, W. S.; Kim, Y. C.; Ryu, S.; Seo, J.; Seok, S. I. Compositional Engineering of Perovskite Materials for High Performance Solar Cells. *Nature* **2015**, *517*, 476–480.

(6) Nie, W.; Tsai, H.; Asadpour, R.; Blancon, J.-C.; Neukirch, A. J.; Gupta, G.; Crochet, J. J.; Chhowalla, M.; Tretiak, S.; Alam, M. A.; Wang, H.-L.; Mohite, A. D. High-Efficiency Solution-Processed Perovskite Solar Cells with Millimeter-Scale Grains. *Science* **2015**, *347*, 522–525.

(7) Saparov, B.; Mitzi, D. B. Organic-Inorganic Perovskites: Structural Versatility for Functional Materials Design. *Chem. Rev.* **2016**, *116*, 4558−4596.

(8) Stranks, S. D.; Snaith, H. J. Metal-Halide Perovskites for Photovoltaic and Light-Emitting Devices. *Nat. Nanotechnol.* **2015**, *10*, 391−402.

(9) McMeekin, D. P.; Sadoughi, G.; Rehman, W.; Eperon, G. E.; Saliba, M.; Hörantner, M. T.; Haghighirad, A.; Sakai, N.; Korte, L.; Rech, B.; Johnston, M. B.; Herz, L. M.; Snaith, H. J. A Mixed-Cation Lead Mixed-Halide Perovskite Absorber for Tandem Solar Cells. *Science* **2016**, *351*, 6269, 151–155.

(10) Hao, F.; Stoumpos, C. C.; Cao, D. H.; Chang, R. P. H.; Kanatzidis, M. G. Lead-Free Solid-State Organic-Inorganic Halide Perovskite Solar Cells. *Nat. Photon.* **2014**, *8*, 489–494.

(11) Giustino, F.; Snaith, H. J. Towards Lead-free Perovskite Solar Cells. *ACS Energy Lett.* **2016**, *1*, 1233–1240.

(12) Volonakis, G.; Filip, M. R.; Haghighirad, A. A.; Sakai, N.; Wenger, B.; Snaith, H. J.; Giustino, F. Lead-Free Halide Double Perovskites via Heterovalent Substitution of Noble Metals. *J. Phys. Chem. Lett.* **2016**, *7*, 1254–1259.

(13) Research Cell Efficiency Records; http://www.Nrel.Gov/Ncpv/ Images/Efficiency_Chart.Jpg

(14) Eperon, G. E.; Leijtens, T.; Bush, K. A.; Prasanna, R.; Green, T.; Wang, J. T.-W.; McMeekin, D. P.; Volonakis, G.; Milot, R. L.; May, R. Perovskite-Perovskite Tandem Photovoltaics with Optimized Band Gaps. *Science* **2016**, *354*, 86–865.

(15) D'Innocenzo, V.; Srimath Kandada, A. R.; De Bastiani, M.; Gandini, M.; Petrozza, A. Tuning the Light Emission Properties by Band Gap Engineering in Hybrid Lead Halide Perovskite. *J. Am. Chem. Soc.* **2014**, *136*, 17730–17733.

(16) Gonzalez-Carrero, S.; Galian, R. E.; Pérez-Prieto, J. Maximizing the Emissive Properties of $CH_3NH_3PbBr_3$ Perovskite Nanoparticles. *J. Mater. Chem. A* **2015**, *3*, 9187–9193.

(17) Zhang, F.; Zhong, H.; Chen, C.; Wu, X. G.; Hu, X.; Huang, H.; Han, J.; Zou, B.; Dong, Y. Brightly Luminescent and Color-Tunable Colloidal $CH_3NH_3PbX_3$ (X = Br, I, Cl) Quantum Dots: Potential Alternatives for Display Technology. *ACS Nano* **2015**, *9*, 4533–4542.

(18) Bade, S. G. R.; Li, J.; Ling, Y.; Tian, Y.; Dilbeck, T.; Besara, T.; Geske, T.; Gao, H.; Ma, B.; Hanson, K.; Siegrist, T.; Xu, C.; Yu, Z. Fully Printed Halide Perovskite Light-Emitting Diodes with Silver Nanowire Electrodes. *ACS Nano* **2016**, *10*, 1795−1801.

(19) Sutter-Fella, C. M.; Li, Y.; Amani, M.; Ager, J. W., III; Toma, F. M.; Yablonovitch, E.; Sharp, I. D.; Javey, A. High Photoluminescence Quantum Yield in Band Gap Tunable Bromide Containing Mixed Halide Perovskites. *Nano Lett.* **2016**, *16*, 800−806.

(20) Schmidt, L. C.; Pertegas, A.; Gonzalez-Carrero, S.; Malinkiewicz, O.; Agouram, S.; Minguez Espallargas, G.; Bolink, H. J.; Galian, R. E.; Perez-Prieto, J. Nontemplate Synthesis of $CH_3NH_3PbBr_3$ Perovskite Nanoparticles. *J. Am. Chem. Soc.* **2014**, *136*, 850–853.

(21) Zhu, F.; Men, L.; Guo, Y.; Zhu, Q.; Bhattacharjee, U.; Goodwin, P. M.; Petrich, J. W.; Smith, E. A.; Vela, J. Shape Evolution and Single Particle Luminescence of Organometal Halide Perovskite Nanocrystals. *ACS Nano* **2015**, *9*, 2948–2959.

(22) Freppon, D. J.; Men, L.; Burkhow, S. J.; Petrich, J. W.; Vela, J.; Smith, E. A. Photophysical Properties of Wavelength-Tunable Methylammonium Lead Halide Perovskite Nanocrystals. *J. Mater. Chem. C* **2017**, *5*, 118–126.

(23) Rosales, B. A.; Men, L.; Cady, S. D.; Hanrahan, M. P.; Rossini, A. J.; Vela, J. Persistent Dopants and Phase Segregation in Organolead Mixed-Halide Perovskites. *Chem. Mater.* **2016**, *28*, 6848–6859.

(24) Men, L.; White, M. A.; Andaraarachchi, H.; Rosales, B. A.; Vela, J. Synthetic Development of Low Dimensional Materials. *Chem. Mater.* **2017**, *29*, 168–175.

(25) Elliott III, E. W.; Glover, R. D.; Hutchison, J. E. Removal of Thiol Ligands from Surface-Confined Nanoparticles without Particle Growth or Desorption. *ACS Nano* **2015**, *9*, 3050–3059.

(26) Zhenhua, C.; Hui, L.; Yongbing, T.; Xing, H.; Derek, H.; Chun-Sing, L. Shape-Controlled Synthesis of Organolead Halide Perovskite Nanocrystals and Their Tunable Optical Absorption. *Mater. Res. Express* **2014**, *1*, 015034.

(27) Ha, S. T.; Liu, X.; Zhang, Q.; Giovanni, D.; Sum, T. C.; Xiong, Q. Synthesis of Organic-Inorganic Lead Halide Perovskite Nanoplatelets: Towards High-Performance Perovskite Solar Cells and Optoelectronic Devices. *Adv Optical Mater* **2014**, *2*, 838–844.

(28) Zhuo, S.; Zhang, J.; Shi, Y.; Huang, Y.; Zhang, B. Self-Template-Directed Synthesis of Porous Perovskite Nanowires at Room Temperature for High-Performance Visible-Light Photodetectors. *Angew. Chem. Int. Ed.* **2015**, *54*, 5693–5696.

(29) Yang, S.; Zheng, Y. C.; Hou, Y.; Chen, X.; Chen, Y.; Wang, Y.; Zhao, H.; Yang, H. G. Formation Mechanism of Freestanding $CH_3NH_3PbI_3$ Functional Crystals: In Situ Transformation vs Dissolution–Crystallization. *Chem. Mater.* **2014**, *26*, 6705–6710.

(30) Li, G.; Tan, Z. K.; Di, D.; Lai, M. L.; Jiang, L.; Lim, J. H.; Friend, R. H.; Greenham, N. C. Efficient Light-Emitting Diodes Based on Nanocrystalline Perovskite in a Dielectric Polymer Matrix. *Nano Lett.* **2015**, *15*, 2640–2644.

(31) Di, D.; Musselman, K. P.; Li, G.; Sadhanala, A.; Ievskaya, Y.; Song, Q.; Tan, Z. K.; Lai, M. L.; MacManus-Driscoll, J. L.; Greenham, N. C.; Friend, R. H. Size-Dependent Photon Emission from Organometal Halide Perovskite Nanocrystals Embedded in an Organic Matrix. *J. Phys. Chem. Lett.* **2015**, *6*, 446–450.

(32) Horvath, E.; Spina, M.; Szekrenyes, Z.; Kamaras, K.; Gaal, R.; Gachet, D.; Forro, L. Nanowires of Methylammonium Lead Iodide ($CH_3NH_3PbI_3$) Prepared by Low Temperature Solution-Mediated Crystallization. *Nano Lett.* **2014**, *14*, 6761–6766.

(33) Wang, X.; Zhou, W.-H.; Zhou, Z.-J.; Hou, Z.-L.; Guo, J.; Wu, S.-X. High-Efficient Dye-Sensitized Solar Cells with All-Inorganic $Cu_2ZnSnSe_4$ Counter-Electrode by Ligand Exchange. *Electrochim. Acta* **2013**, *104*, 26–32.

(34) Liu, W.; Lee, J. S.; Talapin, D. V. III-V Nanocrystals Capped with Molecular Metal Chalcogenide Ligands: High Electron Mobility and Ambipolar Photoresponse. *J. Am. Chem. Soc.* **2013**, *135*, 1349–1357.

(35) Chung, D. S.; Lee, J. S.; Huang, J.; Nag, A.; Ithurria, S.; Talapin, D. V. Low Voltage, Hysteresis Free, and High Mobility Transistors from All-Inorganic Colloidal Nanocrystals. *Nano Lett.* **2012**, *12*, 1813–1820.

(36) Yun, H. J.; Paik, T.; Edley, M. E.; Baxter, J. B.; Murray, C. B. Enhanced Charge Transfer Kinetics of Cdse Quantum Dot Sensitized Solar Cell by Inorganic Ligand Exchange Treatments. *ACS Appl. Mater. Interfaces* **2014**, *6*, 3721–3728.

(37) Nag, A.; Kovalenko, M. V.; Lee, J. S.; Liu, W.; Spokoyny, B.; Talapin, D. V. Metal-Free Inorganic Ligands for Colloidal Nanocrystals: S^{2-}, HS^{-}, Se^{2-}, HSe^{-}, Te^{2-}, HTe^{-}, TeS_3^{2-}, OH^{-}, and NH^{2-} as Surface Ligands. *J. Am. Chem. Soc.* **2011**, *133*, 10612–10620.

(38) Tang, J.; Kemp, K. W.; Hoogland, S.; Jeong, K. S.; Liu, H.; Levina, L.; Furukawa, M.; Wang, X.; Debnath, R.; Cha, D.; Chou, K. W.; Fischer, A.; Amassian, A.; Asbury, J. B.; Sargent, E. H. Colloidal-Quantum-Dot Photovoltaics Using Atomic-Ligand Passivation. *Nat. Mater.* **2011**, *10*, 765–771.

(39) Zhang, H.; Jang, J.; Liu, W.; Talapin, D. V. Colloidal Nanocrystals with Inorganic Halide, Pseudohalide, and Halometallate Ligands. *ACS Nano* **2014**, *8*, 7359–7369.

(40) Stolle, C. J.; Panthani, M. G.; Harvey, T. B.; Akhavan, V. A.; Korgel, B. A. Comparison of the photovoltaic response of oleylamine and inorganic ligand-capped $CuInSe_2$ nanocrystals. *ACS Appl. Mater. Interfaces* **2012**, *4*, 2757–2761.

(41) Choi, S.; Jin, H.; Kim, S. SnS_4^{4-} Metal Chalcogenide Ligand, S^{2-} Metal Free Ligand, and Organic Surface Ligand Toward Efficient CdSe Quantum Dot- Sensitized Solar Cells. *J. Phys. Chem. C* **2014**, *118*, 17019–17027.

(42) Asil, D.; Walker, B. J.; Ehrler, B.; Vaynzof, Y.; Sepe, A.; Bayliss, S.; Sadhanala, A.; Chow, P. C. Y.; Hopkinson, P. E.; Steiner, U.; Greenham, N. C.; Friend, R. H. Role of PbSe Structural Stabilization in Photovoltaic Cells. *Adv. Funct. Mater.* **2015**, *25*, 928–935.

(43) Chuang, C. H.; Brown, P. R.; Bulovic, V.; Bawendi, M. G. Improved Performance and Stability in Quantum Dot Solar Cells Through Band Alignment Engineering. *Nat. Mater.* **2014**, *13*, 796–801.

(44) Huang, J.; Liu, W.; Dolzhnikov, D. S.; Protesescu, L.; Kovalenko, M. V.; Koo, B.; Chattopadhyay, S.; Shenchenko, E. V.; Talapin, D. V. Surface Functionalization of Semiconductor and Oxide Nanocrystals with Small Inorganic Oxoanions (PO_4^{3-}, MoO_4^{2-}) and Polyoxometalate Ligands. *ACS Nano* **2014**, *8*, 9388–9402.

(45) Nag, A.; Chung, D. S.; Dolzhnikov, D. S.; Dimitrijevic, N. M.; Chattopadhyay, S.; Shibata, T.; Talapin, D. V. Effect of Metal Ions on Photoluminescence, Charge Transport, Magnetic and Catalytic Properties of All-Inorganic Colloidal Nanocrystals and Nanocrystal Solids. *J. Am. Chem. Soc.* **2012**, *134*, 13604–13615.

(46) Kovalenko, M. V.; Schaller, R. D.; Jarzab, D.; Loi, M. A.; Talapin, D. V. Inorganically Functionalized PbS-CdS Colloidal Nanocrystals: Integration into Amorphous Chalcogenide Glass and Luminescent Properties. *J. Am. Chem. Soc.* **2012**, *134*, 2457–2460.

(47) Dirin, D. N.; Dreyfuss, S.; Bodnarchuk, M. I.; Nedelcu, G.; Papagiorgis, P.; Itskos, G.; Kovalenko, M. V. Lead Halide Perovskites and Other Metal Halide Complexes as Inorganic Capping Ligands for Colloidal Nanocrystals. *J. Am. Chem. Soc.* **2014**, *136*, 6550–6553.

(48) Rowland, C. E.; Liu, W.; Hannah, D. C.; Chan, M. K.; Talapin, D. V.; Schaller, R. D. Thermal Stability of Colloidal InP Nanocrystals: Small Inorganic Ligands Boost High-Temperature Photoluminescence. *ACS Nano* **2014**, *8*, 977–985.

(49) Yamada, K.; Sera, H.; Sawada, S.; Tada, H.; Okuda, T.; Tanaka, H. Reconstructive Phase Transformation and Kinetics of $Cs_3Sb_2I_9$ by Means of Rietveld Analysis of X-Ray Diffraction and ^{127}I NQR. *J. Solid State Chem.* **1997**, *134*, 319–325.

(50) Papavassiliou, G. C.; Koutselas, I. B. Excitonic Bands in the Optical Absorption Spectra of A_3MX_6 and $A_3M_2X_9$ (A = $MeNH_3$, Me_2NH_2, Me_3NH, Me_4N; M= Bi, Sb; X= Cl, Br, I) *Z. Naturforsch, B: Chem. Sci.* **1994**, *49*, 849–851.

(51) Kuok, M. H.; Ng, S. G.; Tan, L. S.; Rang, Z. L.; Iwata, M.; Ishibashi, Y. A Brillouin Study of the Ferroelastic Phase Transition in $(CH_3NH_3)_3Sb_2Br_9$. *Solid State Commun.* **1998**, *108*, 159–163.

(52) Wojtaś, M.; Bator, G.; Jakubas, R.; Zaleski, J. Crystal Structure, Phase Transition and Ferroelectric Properties of the $[(CH_3)_3\ NH]_3[Sb_2Cl_{9(1-x)}Br_{9x}]$(TMACBA) Mixed Crystals. *J. Phys: Condens. Matter* **2003**, *15*, 5765.

(53) Saparov, B.; Hong, F.; Sun, J.-P.; Duan, H.-S.; Meng, W.; Cameron, S.; Hill, I. G.; Yan, Y.; Mitzi, D. B. Thin-Film Preparation and Characterization of $Cs_3Sb_2I_9$: A Lead-Free Layered Perovskite Semiconductor. *Chem. Mater.* **2015**, *27*, 5622–5632.

(54) Zhang, J.; Shang, M.-h.; Wang, P.; Huang, X.; Xu, J.; Hu, Z.; Zhu, Y.; Han, L. n-Type Doping and Energy States Tuning in $CH_3NH_3Pb_{1-x}Sb_{2x/3}I_3$ Perovskite Solar Cells. *ACS Energy Lett.* **2016**, *1*, 535–541.

(55) Oku, T.; Ohishi, Y.; Suzuki, A. Effects of Antimony Addition to Perovskite-Type $CH_3NH_3PbI_3$ Photovoltaic Devices. *Chem. Lett.* **2016,** *45*, 134–136.

(56) Liu, M.; Johnston, M. B.; Snaith, H. J. Efficient Planar Heterojunction Perovskite Solar Cells by Vapour Deposition. *Nature* **2013**, *501*, 395–398.

(57) Docampo, P.; Ball, J. M.; Darwich, M.; Eperon, G. E.; Snaith, H. J. Efficient Organometal Trihalide Perovskite Planar-Heterojunction Solar Cells on Flexible Polymer Substrates. *Nature commun.* **2013**, *4*, 2761.

(58) Burschka, J.; Pellet, N.; Moon, S.-J.; Humphry-Baker, R.; Gao, P.; Nazeeruddin, M. K.; Grätzel, M. Sequential Deposition as a Route to High-Performance Perovskite-Sensitized Solar Cells. *Nature* **2013**, *499*, 316–319.

(59) Marinova, N.; Tress, W.; Humphry-Baker, R.; Dar, M. I.; Bojinov, V.; Zakeeruddin, S. M.; Nazeeruddin, M. K.; Grätzel, M. Light Harvesting and Charge Recombination in $CH_3NH_3PbI_3$ Perovskite Solar Cells Studied by Hole Transport Layer Thickness Variation. *ACS nano* **2015**, *9*, 4200–4209.

(60) Im, J.-H.; Jang, I.-H.; Pellet, N.; Grätzel, M.; Park, N.-G. Growth of $CH_3NH_3PbI_3$ Cuboids with Controlled Size for High-Efficiency Perovskite Solar Cells. *Nat. Nanotechnol.* **2014**, *9*, 927–932.

Supporting Information

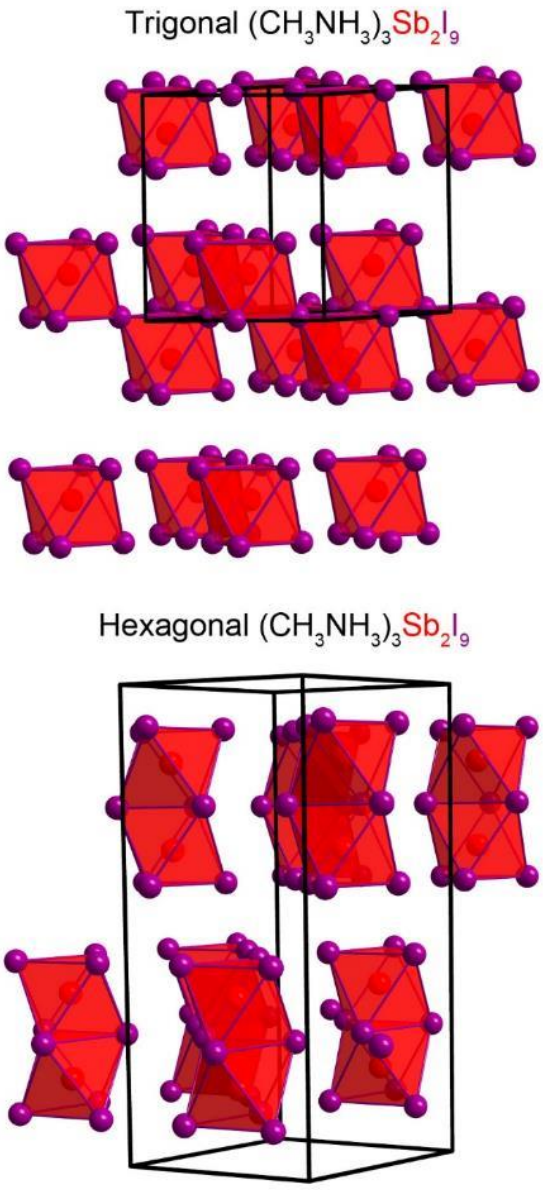

Figure S1. Comparison of two $(CH_3NH_3)_3Sb_2I_3$ structures: P$\bar{3}$*m*1 (trigonal) and P63*/mmc* (hexagonal).

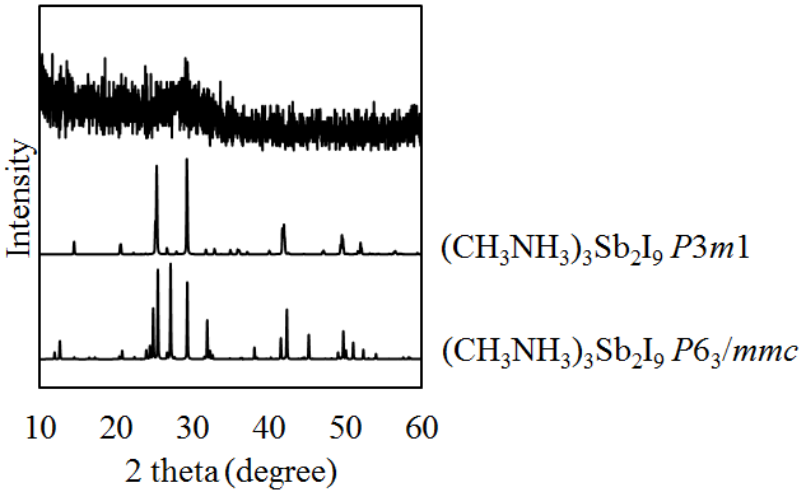

Figure S2. Powder XRD pattern of yellow product generated by stirring $(CH_3NH_3)_3Sb_2I_3$ in crude solution.

Table S1. Lattice spacing in $(CH_3)_3Sb_2I_9$.

h k l	d (Å)
2 0 -2	3.0514
2 0 1	3.5178

Table S2. Bandgap, PL peak and quantum yield of nanocrystals prepared with $(CH_3)_3Sb_2I_9$ capping.

Sb ratio	Bandgap (eV)	PL peak (nm)	QY (%)
0%	1.56	778	-
10%	1.56	750	0.15
20%	1.58	745	0.1
30%	1.61	748	0.08
40%	1.57	757	0.18

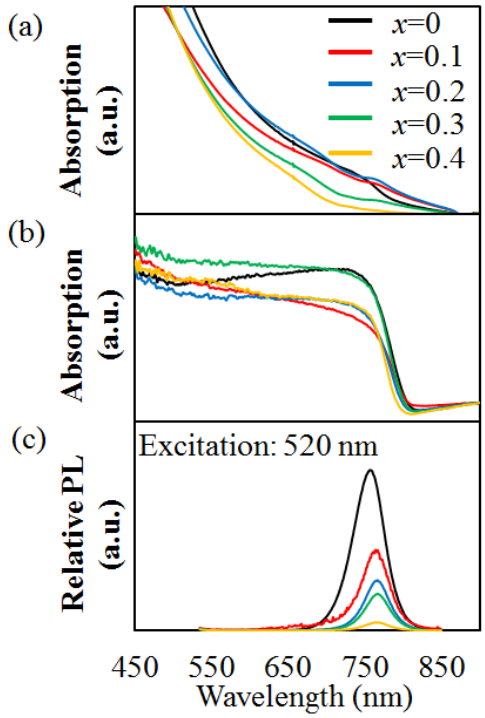

Figure S3. Solution-phase optical density (O.D. includes absorption and scattering) (a), solid-film diffuse reflectance (b), and relative photoluminescence spectra (normalized by each sample's O.D. at λ_{exc} = 520 nm) (c) of Sb-Pb perovskites with different Sb ratio in presence of n-$C_8H_{17}NH_3I$.

Table S3. Bandgap, PL peak and quantum yield of nanocrystals prepared with both $(CH_3)_3Sb_2I_9$ and n-$C_8H_{17}NH_3I$ capping.

Sb ratio	Bandgap (eV)	PL peak (nm)	QY(%)
0%	1.57	757	4.0
10%	1.56	764	2.1
20%	1.57	767	1.1
30%	1.57	768	0.8
40%	1.59	765	0.2

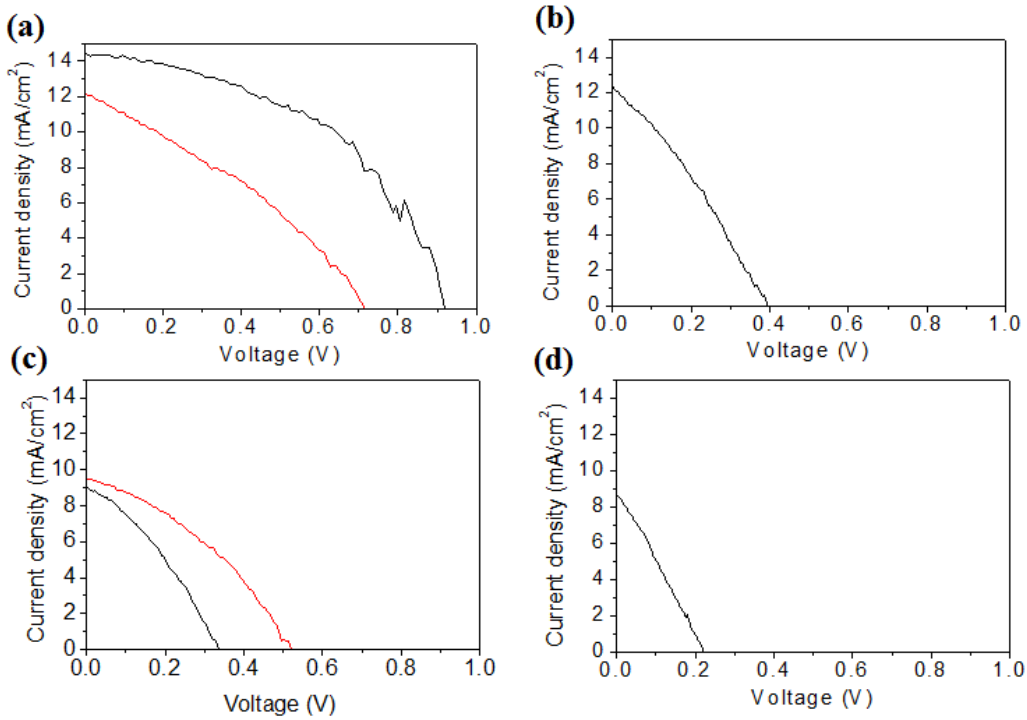

Figure S4. I-V curves of perovskite solar cells with different molar ratio of Sb doping: (a) 0% Sb, (b) 1% Sb, (c) 2% Sb, (d) 5% Sb.

CHAPTER 4. LEAD-FREE GERMANIUM PEROVSKITES: SOFT CHEMISTRY, DIMENSIONALITY CONTROL, AND MANGANESE-DOPING

Long Men, Bryan A. Rosales, Noreen E. Gentry, Javier Vela

Abstract

Organometal halide perovskites have drawn enormous interest recently as promising photovoltaic and optoelectronic materials along with their unique and remarkable properties; however, lead is a heavy metal element and its potential toxicity raises concerns for environmental compatibility. To address this problem, we developed a synthetic route to bulk cesium germanium triiodide ($CsGeI_3$) and their nanocrystals. With a direct bandgap of 1.6 eV and a corner-sharing octahedral network crystal structure that are comparable to $CH_3NH_3PbI_3$, $CsGeI_3$ is potentially promising for photovoltaic applications. The structural and optical properties were investigated by transmission electron microscopy (TEM), X-ray diffraction (XRD) and diffuse reflectance. To manipulate the optoelectronic properties, we doped high-spin, divalent manganese ions (Mn^{2+}) into the octahedral Ge^{2+} sites of $CsGeI_3$. Electron paramagnetic resonance (EPR) helps us better understand the local ion environment and composition of both $CsGeI_3$ and its doped analogue ($CsGe_{1-x}Mn_xI_3$). Our results expand the lead-free halide perovskite family and set the stage for their application beyond photovoltaics to spintronics and magnetic data storage.

Introduction

Lead halide perovskites have garnered great interest due to their excellent optoelectronic properties. Solar energy conversion efficiency of perovskite solar cells has surged from 3.8% to 22.1% within eight years,[1, 2] by virtue of their panchromatic light absorption, long carrier diffusion length and defect-tolerant behavior.[3-8] All of these factors make perovskites ideal candidates as light harvesters in next generation solar cells. Also, due to their long carrier lifetime, tunable emission and high quantum yield observed in

nanocrystals, the rise of perovskite nanocrystals as chromophores rejuvenates interest in the development of light-emitting materials[9-13] and low-threshold lasers.[14-17]

However, the element lead is a toxic, heavy metal that attacks the nervous and reproductive systems in humans and also raises concerns for environmental compatibility.[18-20] There is a need to reduce our dependency on lead by pursuing lead-free perovskites such as those based on germanium,[21] tin,[22-27] bismuth[28-30] or double perovskites.[31-34] Germanium perovskites, in particular, are excellent candidates to replace lead because most germanium compounds are considered as having rather low toxicity and are not carcinogenic to humans. [35,36] Moreover, germanium iodide perovskites exhibit a direct bandgap of 1.6 eV with a similar corner-sharing octahedral network as lead perovskites.[37] Theoretical studies suggest that germanium perovskites are a promising and competitive alternative to lead perovskites for efficient perovskite solar cells.[38-42] In spite of this, germanium perovskites are notably less experimentally explored compared to the other lead-free perovskites mentioned.

It is well established that transition metal doping can expand the application of semiconductor nanocrystals into new fields of energy transfer, optoelectronic devices and spintronics by introducing new electronic, optical and magnetic properties.[43-46] Doping lead perovskite nanocrystals with transition metal manganese ions (Mn^{2+}) has been shown to manipulate the magnetic and optical properties.[47-49] Manganese substitutions of up to 46% were reported that greatly enhances the photoluminescence quantum yields by ~10 times.[50] Efficient energy transfer from the host to the dopants manganese ions leads to a $^4T_1 – ^6A_1$ manganese d-electron emission. However, lead ion (Pb^{2+}) has a radius of 133 pm whereas high-spin manganese ion (Mn^{2+}) has a radius of 97 pm.[51] This large radius difference causes high lattice mismatch that will not allow formation of a solid solution according to Hume-Rothery rules.[52] On the contrary, germanium ions (Ge^{2+}) have an ionic radius of 87 pm,

which is closer to the radius of Mn^{2+}.[51] This small radius difference (< 15%) should lead to a higher incorporation of Mn^{2+} in germanium perovskites compared to lead perovskites, although a complete solid solution is not expected due to the different crystal structures.

Herein, we report the first synthesis of cesium germanium triiodide perovskite nanocrystals and demonstrate size control through ligand concentration. The bandgap of nanocrystals blue-shifted with decreasing particle size. We also doped high-spin, divalent manganese ions (Mn^{2+}) into the octahedral germanium sites in the lattice. A linear lattice expansion was observed with ascending MnI_2 synthetic loading, which is consistent with the incorporation of larger manganese ions in germanium perovskite lattice. Also, electron paramagnetic resonance spectroscopy (EPR) helps us better understand the local manganese ion environment in the doped germanium perovskites ($CsGe_{1-x}Mn_xI_3$).

Experimental

Materials. Germanium(IV) oxide (≥99.99%), cesium iodide (99.999%), hydriodic acid (ACS, 55%), hydrobromic acid (ACS, 48%) and cysteamine (95%) were purchased from Sigma-Aldrich; cesium bromide (99.9%-Cs), manganese(II) oxide (99%), manganese(II) iodide (98+%) and silicon powder (99+%) from Strem; hypophosphorous acid (50% w/w aqueous solution) from Alfa Aesar. All chemicals were used as received.

Synthesis. *Bulk germanium perovskites.* Cesium germanium halide perovskites were prepared by a slightly modified literature procedure.[21] Briefly, germanium(IV) oxide (10.5 mg, 0.1 mmol) was added to a mixture of hydrohalic acid (0.7 mL, 7.3 M for HI and 0.6 mL, 8.8 M for HBr) and hypophosphorous acid (0.25 mL, 9.1 M), and heated up to 120 °C while stirring until everything dissolved. An aqueous solution of cesium halide (0.3 mL, 0.3 M) was injected. The mixture was cooled to 0 °C, and a black ($CsGeI_3$) or orange ($CsGeBr_3$) solid precipitated. The precipitate was collected by centrifugation for 5 min at

4500 rpm and kept under an inert, dry N_2 or Ar atmosphere. *Germanium perovskite nanocrystals*. Cysteammonium halide solution: Cysteamine (771 mg, 10 mmol) was mixed with hydrohalic acid solution (1.4 mL, 7.3 M for HI or 1.4 mL, 8.8 M for HBr). Germanium(IV) oxide (10.5 mg, 0.1 mmol) was dissolved in a mixture of hydrohalic acid (0.7 mL, 7.3 M for HI and 0.6 mL, 8.8 M for HBr) and hypophosphorous acid (0.25 mL, 9.1 M) at 120 °C. Cysteammonium halide solution (0.2 mL, 7.3 M) was added, causing the formation of an orange precipitate. Cesium halide solution (0.3 mL, 0.3 M) was added, causing the orange precipitate to redissolve. The mixture was cooled to 0 °C, and a black ($CsGeI_3$) or orange ($CsGeBr_3$) solid precipitated. The precipitate was collected by centrifugation for 5 min at 4500 rpm and kept under an inert, dry N_2 or Ar atmosphere. For manganese-doped samples, a stoichiometric amount of germanium(IV) oxide was replaced (1:1) with the desired loading amount of manganese precursor (manganese oxide or manganese halide). The rest procedures are similar to the undoped samples.

Structural Characterization. *Powder X-ray diffraction* (XRD) data were measured using Cu Kα radiation on Rigaku Ultima IV (40 kV, 44 mA). Samples were measured on a "background-less" quartz slide. *Transmission electron microscopy* (TEM) was conducted using a FEI Technai G2 F20 field emission TEM operating at up to 200 kV with a point-to-point resolution of less than 0.25 nm and a line-to-line resolution of less than 0.10 nm. Dilute sample solutions in toluene were dropped onto carbon-coated copper grids. Elemental composition was assessed by energy-dispersive spectroscopy (EDS). Particle sizes (dimensions) based on the longest edge and statistics (>300 particles) were measured manually using ImageJ.

Optical Characterization. *Optical extinction* (absorption plus scattering) spectra of solutions were measured with a photodiode-array Agilent 8453 UV/vis spectrophotometer. Solvent absorption was recorded and subtracted from all spectra.

Diffuse reflectance spectra of solid films were measured with a SL1 Tungsten Halogen lamp (vis-IR), a SL3 Deuterium Lamp (UV), and a BLACK-Comet C-SR-100 Spectrometer. Samples were prepared by drop-casting toluene solutions onto glass. *Steady-state photoluminescence* (PL) spectra were measured with a Horiba-Jobin Yvon Nanolog scanning spectrofluorometer equipped with a photomultiplier detector. Relative PL quantum yields (QYs) were measured against using Coumarin 460 dye using standard procedures.

Other characterization. *Electron Paramagnetic Resonance* (EPR) spectra were measured using an ELEXYS E580 EPR Spectrometer (Bruker BioSpin) equipped with an SHQE resonator and an Oxford ESR900 cryostat. The samples were dispersed in ethanol, placed in a 4 mm quartz tube, and frozen in liquid N_2 prior to insertion into the cryostat. Low temperature spectra were measured at 10 K. Typical spectra were acquired with a sweep width of 5000 G, 2048 points, 8 G amplitude modulation, and 1.986 mW microwave power. Simulations were performed in the computational package EasySpin, which runs on the Matlab platform, using the "pepper" function.

Results and Discussion

Ge- vs. Pb-based Perovskites. Metal halide perovskites have a general formula AMX_3, where A is a monovalent cation ($CH_3NH_3^+$, Cs^+), M is a divalent metal cation (Pb^{2+}, Ge^{2+}) and X is a halide anion (I^-, Br^- or Cl^-). In the perovskite family, Pb-based perovskites have been the most widely studied due to their extraordinary photovoltaic properties; however, the heavy element lead still remains a concern for their solar cell commercialization. Due to the versatility of perovskite composition, one can substitute lead with any divalent metal cations and retain the perovskite structure, as long as the tolerance factor is close to one.[53] Ge^{2+} is a promising alternative as lead substitute due to their high similarity in structural and optical properties when forming perovskites. Similar to the

$[PbX_6]^{2-}$ corner sharing network in Pb-based perovskites, Ge-based perovskites also exhibit a corner-sharing $[GeI_6]^{4-}$ octahedral network. While $CsGeCl_3$ retains the cubic unit cell, $CsGeBr_3$ and $CsGeI_3$ have a hexagonal distorted structure with tilted octahedra due to a larger tolerance factor (Figure 1a-c).[54,55] The distorted octahedra in $CsGeI_3$ has different Ge–I bond lengths where three bonds are shorter with a distance of 2.75 Å while the other three bonds are longer with a distance of 3.26 Å (Figure 1d).[21] This asymmetry in octahedra is caused by a second-order Jahn-Teller effect.[56]

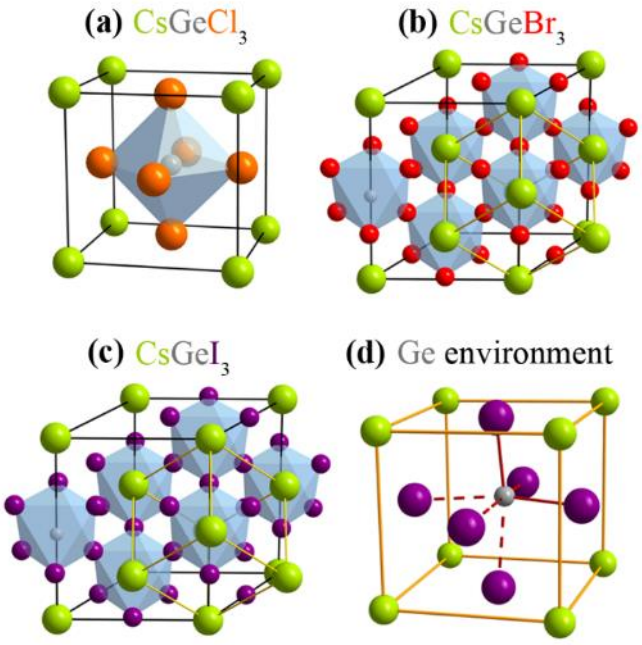

Figure 1. Unit cells of cesium germanium perovskite $CsGeCl_3$ (a), $CsGeBr_3$ (b) and $CsGeI_3$ (c) and octahedral germanium(II) coordination geometry of cesium germanium iodide perovskites (d).

One unique photophysical property Pb-based perovskites exhibit is their panchromatic absorption. Especially the iodide perovskite $CH_3NH_3PbI_3$ has a bandgap of 820 nm (1.5 eV), which allows it to absorb lights from the entire visible light region.[57] This bandgap is very close to the ideal bandgap of 1.34 eV for light harvesting materials, which indicates the theoretical efficiency limit is up to 33%.[58] $CsGeI_3$ also exhibits a band gap of

775 nm (1.6 eV), as shown in Figure 2c and 2d, which also allows $CsGeI_3$ to utilize solar light efficiently.[59] Figure S1 and Table S1 compare the bandgap values of $CsGeX_3$ with $CsPbX_3$ and $CH_3NH_3PbX_3$. The bandgap values of germanium perovskites show only a minor difference with lead perovskites, which indicates the effect of Ge^{2+} around the Fermi level of perovskites is analogous to Pb^{2+}.[60] This observation further establishes germanium perovskites as a promising replacement for lead perovskite photovoltaic materials.

Synthesis and Dimensionality Control. The general synthesis of $CsGeI_3$ is shown in Scheme 1.[21] Briefly, GeO_2 is dissolved in a mixture of HI and H_3PO_2 at 120 °C followed by injection of CsI pre-dissolved in water. $CsGeI_3$ is precipitated when the flask is submerged in an ice bath. H_3PO_2 serves as a reducing agent and prevents the oxidation of Ge^{2+} in $CsGeI_3$, which explains why we can perform this reaction in air. Upon adding GeO_2 into the acidic solution, GeI_4 is initially formed as an orange powder (confirmed by XRD, see Figure S2) that then re-dissolves by maintaining 120 °C over several seconds to form a transparent yellow solution. These observations suggest that GeI_4 is formed from the reaction between GeO_2 and HI followed by reduction of GeI_4 with H_3PO_2 to form Ge^{2+}. Powder X-ray diffraction (XRD) shows that our $CsGeI_3$ sample matches the standard pattern (Figure 2a). The sample crystalizes in micro-size scale as shown by SEM (Figure 2b). A bandgap of 1.6 eV is confirmed by diffuse reflectance and Tauc plot (Figure 2c and 2d), but no photoluminescence has been observed from $CsGeI_3$. Following the similar method using HBr, we are also able to synthesize $CsGeBr_3$, which appears as an orange precipitate in ice-water bath. Nothing precipitated out when we tried to synthesize $CsGeCl_3$, possibly due to a higher solubility of $CsGeCl_3$ in water.

Scheme 1.

$$GeO_{2\,(aq)} + \text{xs } HI_{(aq)} + \text{xs } H_3PO_{2\,(aq)} \xrightarrow[2)\ 0\ ^\circ C]{1)\ CsI_{(aq)} / 120\ ^\circ C} CsGeI_{3\,(s)}\ \text{(unbalanced)}$$

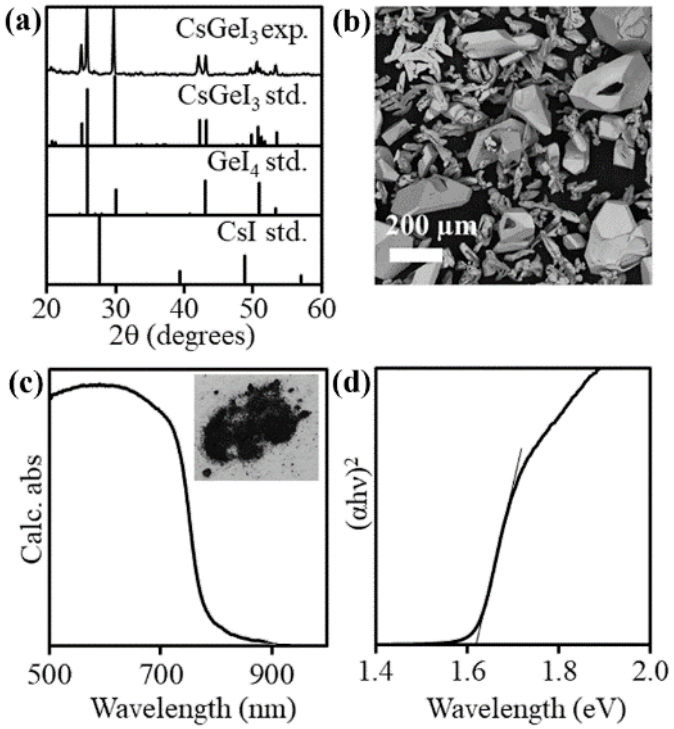

Figure 2. Powder XRD patterns (a), a typical SEM image (b), diffuse reflectance spectrum (c) and Tauc plot (d) of $CsGeI_3$ powder. A representative visual image is shown in the inset of (c).

Knowing that perovskite nanocrystals often exhibit unique electronic and optical properties, we also explored the synthesis of $CsGeI_3$ nanocrystals. Using bulky organic cation has been widely applied in synthesis of lead perovskite nanocrystals.[61-65] This organic cation serves as a blocker to terminate the lattice growth direction leading to size-controlled crystals. However, common ligands, such as the octylammonium cations used in our previous work,[66, 67] do not result in germanium perovskite nanocrystals. Here we

utilized short chain, ionic organic cysteammonium cations ($HSCH_2CH_2NH_3^+$) as ligands to control $CsGeI_3$ particle size (Scheme 2). We investigated the effect of cysteammonium ligand concentration by keeping the concentration of [Ge^+] and [Cs^+] constant at 0.05 M while increasing the concentration of [$HSCH_2CH_2NH_3^+$] from 0 to 2.50 M. Figure 3a displays the powder XRD patterns of $CsGeI_3$ perovskites at different concentrations of ligand concentrations. With cysteammonium ligand concentration up to 2.50M, powder XRD patterns match the $CsGeI_3$ standard pattern. As expected, a larger ligand concentration leads to a smaller particles size. Calculated by Scherrer equation, the particle size is over 100 nm when no ligands are introduced and is reduced to 26 ± 2 nm with a ligand concentration of 2.50 M (Figure 3b). When ligand concentration is 2.50 M, the diffraction peak at 25 degrees could be a convolution of two broad peaks from $CsGeI_3$ nanocrystals. Ligand concentration over 2.50M leads to no precipitate at the end of the reaction.

Scheme 2.

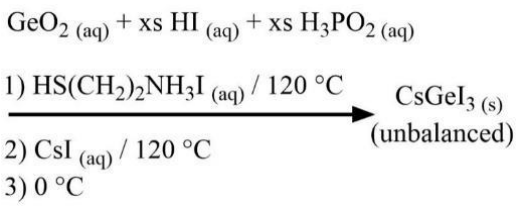

We characterized the morphology of $CsGeI_3$ nanocrystals prepared with different ligand concentrations by scanning and transmission electron microscopy (SEM and TEM). In the absence of cysteammonium cations, the crystals are quite large with an average particle size over 100 μm (Figure 4a). When ligand concentration is 0.5 M (10 molar equivalents), the average particle size is 79 ± 26 nm with triangular and hexagonal morphologies (Figure 4b). If the ligand concentration is increased to 2.5 M, the particle size decreases to 34 ± 8 nm with a narrower size distribution (Figure 4c and 4e). Selected area electron diffraction (SAED) of $CsGeI_3$ nanocrystals is consistent with the trigonal structure

(Figure 4d). Composition analyses of several individual particles by energy dispersive X-ray spectroscopy (EDS) confirmed the presence of all three elements with atomic % of 15 ± 1 for Cs, 27 ± 2 for Ge and 57 ± 1 for I (Cs: Ge: I = 1: 1.8: 3.8). High-resolution transmission electron microscopy (HRTEM) shows the lattice fringes along (021) direction, which has a d spacing of 3.425 Å (Figure 5).

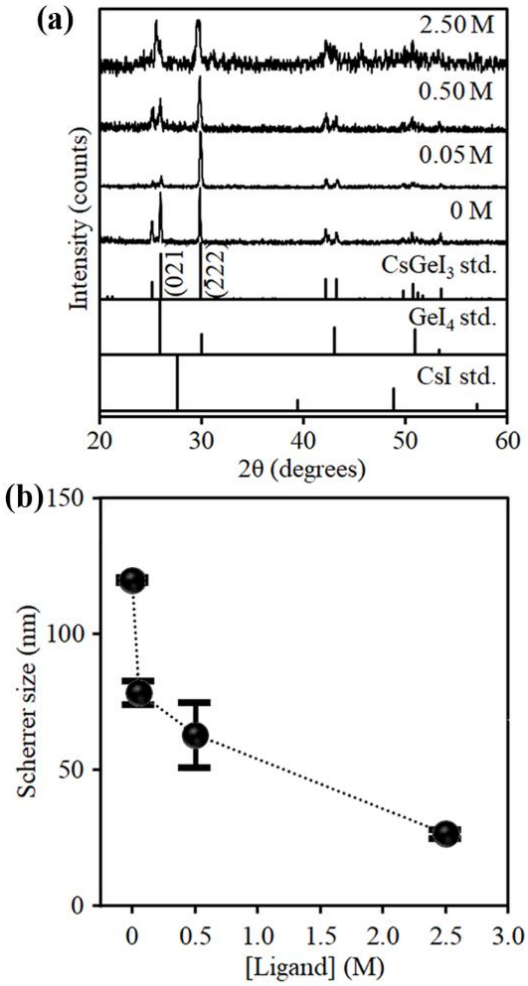

Figure 3. (a) Powder XRD patterns of $CsGeI_3$ perovskite crystals made in different ligand concentrations. $[Ge^{2+}] = [Cs^{+}] = 0.05$ M in all cases. (b) Average XRD sizes based on Scherrer equation as a function of ligand concentrations. The full width half maxima (FWHM) of the two most intense peaks, (-222) and (021), were measured to calculate XRD sizes and error bars.

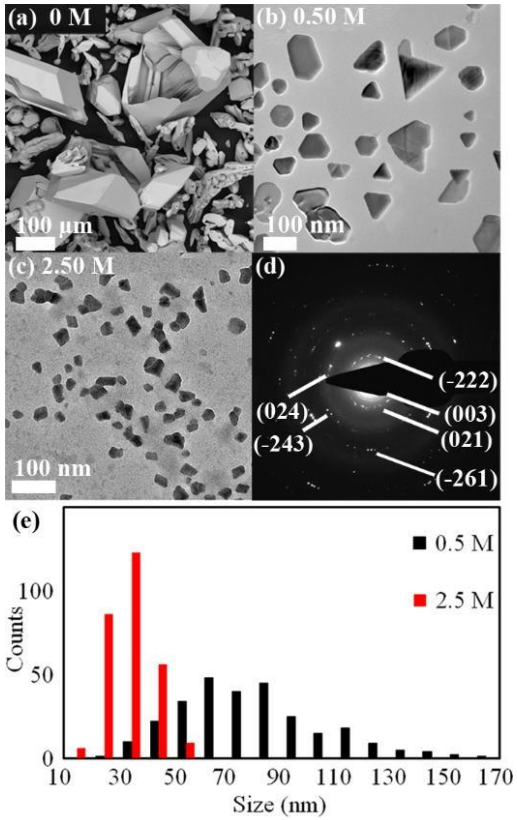

Figure 4. Representative SEM (a), TEM (b, c) images, SAED pattern (d) and size distribution histograms (over 300 particles counted in each case) for $CsGeI_3$ perovskites at three different ligand concentrations: 0, 0.5 and 2.5 M (a, b and c, respectively). SAED pattern (d) is collected on the $CsGeI_3$ with ligand concentration of 0.5 M.

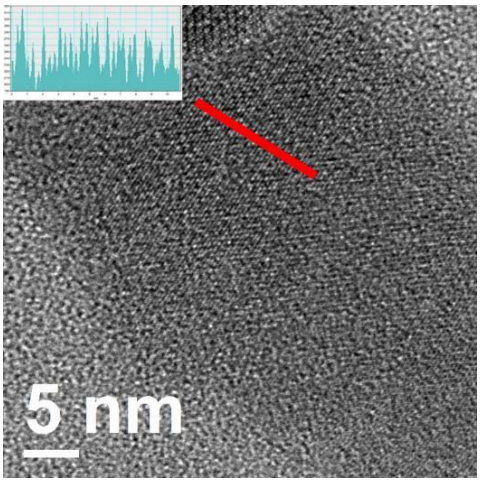

Figure 5. Representative HRTEM image of a $CsGeI_3$ nanocrystal. A line profile along the (021) direction (red line and inset) reveals lattice spacings of 0.3425 nm.

Figure 6 shows solid state diffuse reflectance spectra and their Tauc plots of $CsGeI_3$ perovskites. The diffuse reflectance spectra (Figure 6a) are better than solution phase absorption spectra in determining the absorption onsets because of the poor solubility of $CsGeI_3$ in aqueous solution. Tauc plots (Figure 6b) display a blue-shift from 1.61 eV for bulk $CsGeI_3$ ([ligand] = 0) to 1.66 eV for nano $CsGeI_3$ ([ligand] = 2.5 M). To determine whether or not this shift results from quantum confinement, we calculated the excitonic Bohr diameter for $CsGeI_3$. In effective mass theory,[68] the effective Bohr radius of a Wannier-Mott exciton can be determined from $a^* = a_0\varepsilon^{\infty}(\frac{m_0}{m_e} + \frac{m_0}{m_h})$, where hydrogen Bohr radius a_0 = 0.0529 nm, effective dielectric constant ε^{∞} = 5.0, electron-hole reduced effective masses m_h/m_0 = 0.2 and m_e/m_0 = 0.4 (Z → L) or 0.2 (Z → Γ).[56] Using these values, we estimated the effective Bohr radius is 2.5 nm. However, the smallest average particle size we have obtained is 34 ± 8 nm, which is larger than the estimated Bohr radius and disproves the hypothesis that the blue-shift derives from quantum confinement. In our previous work on lead perovskite nanocrystals, it is worth mentioning that we also noticed a bandgap blue shift when crystal size is larger than the reported Bohr radii.[13] Further study needs to be carried out to understand this phenomenon.

Table 1. $CsGeI_3$ perovskites synthesized under various ligand concentrations.

[Ligand] (M)	XRD size (nm) [a]	TEM size	Bandgap (eV)
0	106 ± 14	50-500 μm [b]	1.61
0.05	78 ± 4	-[c]	1.62
0.50	63 ± 12	79 ± 26 nm	1.64
2.50	26 ± 2	34 ± 8 nm	1.66

[a] XRD size is calculated by Scherrer equation. [b] Measured by SEM images. [c] Not measured.

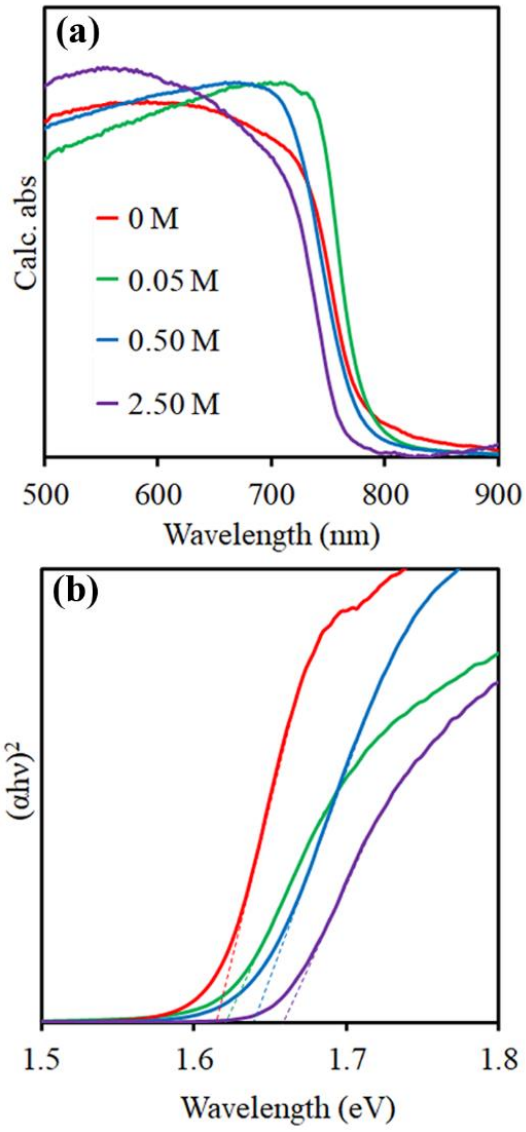

Figure 6. Diffuse reflectance (a) and Tauc plot (b) for $CsGeI_3$ crystals made with different cysteammonium ligand concentrations. $[Ge^{2+}] = [Cs^+] = 0.05$ M in all cases.

Cysteammonium cations can also be used as ligands in the synthesis of $CsGeBr_3$. Keeping the concentration of $[Ge^+]$ and $[Cs^+]$ constant at 0.067 M while increasing the concentration of $[HSCH_2CH_2NH_3^+]$ from 0 to 3.33 M. Figure 7a displays the powder XRD patterns of $CsGeBr_3$ perovskites at different concentrations of ligand concentrations. With cysteammonium ligand concentration up to 3.33 M, powder XRD patterns match the $CsGeBr_3$ standard pattern. As expected, a larger ligand concentration leads to a smaller

particles size. Calculated by Scherrer equation, the particle size is over 100 nm when no ligands are introduced and is reduced to 50 ± 5 nm with a ligand concentration of 3.33 M. Noted that the XRD pattern of $CsGeBr_3$ without any ligands has been amplified by 50 times because the intensity of diffraction peak from (-222) plane is too high, possibly due to preferred orientation in this sample. A representative TEM image of $CsGeBr_3$ perovskites at a ligand concentration of 3.33 M shows the nanoparticles have an average size of 53 ± 10 nm.

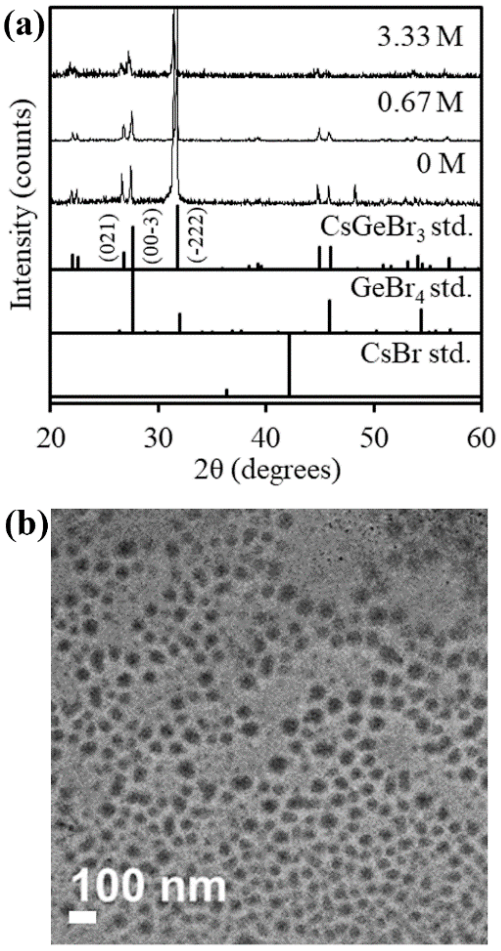

Figure 7. (a) Powder XRD patterns of $CsGeBr_3$ perovskite crystals made in different ligand concentrations. $[Ge^{2+}] = [Cs^{+}] = 0.067$ M in all cases. (b) A representative TEM image of $CsGeBr_3$ perovskites at a ligand concentration of 3.33 M.

Figure 8a shows for $CsGeBr_3$ crystals made with different cysteammonium ligand concentrations. $CsGeBr_3$ nanocrystals have a bandgap of 520 nm (2.4 eV). Unlike $CsGeI_3$ nanocrystals, no bandgap shift is observed with different ligand concentrations. Photoluminescence (PL) spectra (Figure 8b) show a weak PL at 500 nm, especially in nanocrystals. Among these three ligand concentrations, $CsGeBr_3$ nanocrystals with ligands appear to be more emissive than sample without ligands. This could be explained by better surface passivation of the nanocrystals from cysteammonium cations. When ligand concentration reaches 0.67 M, $CsGeBr_3$ nanocrystals have the most intense PL with a quantum yield of 0.34%. Noted that the photoluminescence peak at 450 nm is not derived from $CsGeBr_3$. We speculate some emissive impurities might give rise to the blue peak at 450 nm.

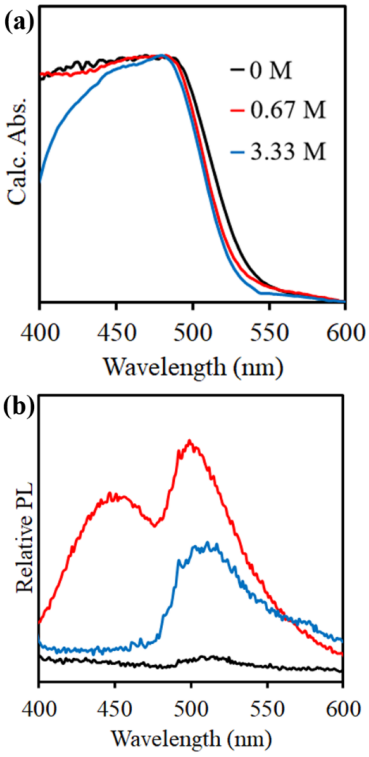

Figure 8. Diffuse reflectance (a) and photoluminescence spectra(b) for $CsGeBr_3$ crystals made with different cysteammonium ligand concentrations. $[Ge^{2+}] = [Cs^{+}] = 0.067$ M in all cases.

Manganese Doping. In order to incorporate Mn^{2+} into $CsGeI_3$ perovskites, we introduced MnI_2 with GeO_2 at the start of the reaction and the procedure above was repeated (Scheme 3). Powder XRD shows that $CsGe_{1-x}Mn_xI_3$ retains the same trigonal structure as $CsGeI_3$ (Figure 9a) despite the fact that $CsMnI_3$ has a hexagonal structure with a face-sharing octahedra network (Figure S3). The zoomed-in region of XRD patterns between 28 and 30 degrees reveals the peaks are monotonically shifted to lower angles with increasing MnI_2 synthetic loading (Figure 9b). The peak shift of $CsMn_xGe_{1-x}I_3$ in Figure 9b is consistent with lattice expansion due to the substitution of octahedral Ge^{2+} (six-coordinate crystal ionic radius of 87 pm) with larger Mn^{2+} (six-coordinate high spin crystal ionic radius of 97 pm).[51] The percentage of manganese incorporation into the $CsGeI_3$ lattice was estimated based on Vegard's Law[69,70]:

$$a_{(CsMn_xGe_{1-x}I_3)} = a_{(CsGeI_3)}(x) + a_{(simulated\ CsMnI_3)}(1-x).$$

Here, a is the lattice parameter and x is the composition of Mn^{2+} in the crystals. Since $CsMnI_3$ has a different crystal structure with $CsGeI_3$ (Figure 1c and S3), we simulated a trigonal cornering-sharing $CsMnI_3$ crystal as a reference to estimate the lattice parameter (see Figure S4 for details). Both the lattice parameter and actual manganese incorporation in $CsMn_xGe_{1-x}I_3$ are plotted as a function of MnI_2 synthetic loading in Figure 9c and Table 1. The shift of the most intense diffraction peak indicates a linear lattice expansion from 8.358 Å ($CsGeI_3$) to 8.397 Å ($CsMn_{0.29}Ge_{0.71}I_3$). To ensure this peak shift is not caused by other factors such as sample height or instrument effects, silicon powder was used as an internal standard. A problem with this standard is that the most intense diffraction peak of $CsMnI_3$ overlaps with one of the major silicon peaks at ~28 degrees. We also collected the powder XRD without silicon powder to confirm that no $CsMnI_3$ formed. Note that the actual manganese incorporation is lower than MnI_2 synthetic loading, which means not all

Mn^{2+} can be doped into $CsGeI_3$ crystals. The majority of Mn^{2+} still remains in solution and no new precipitates are observed. We also noticed the reaction yield decreases with increasing MnI_2 synthetic loading (Figure S5 and Table S2), which also supports our assumption that most of Mn^{2+} is present in the solution. $CsMnI_3$ might be more soluble in aqueous solution, possibly due to a more prominent ionic property of Mn^{2+} than Ge^{2+}.

Scheme 3.

$$(1\text{-}x)\ GeO_{2\ (aq)} + x\ MnI_{2\ (s)} + \text{xs}\ HI_{\ (aq)} + \text{xs}\ H_3PO_{2\ (aq)}$$

$$\xrightarrow[2)\ 0\ ^\circ C]{1)\ CsI_{\ (aq)}\ /\ 120\ ^\circ C} CsMn_xGe_{1-x}I_{3\ (s)}\ (x = 0\text{-}1)\ \text{(unbalanced)}$$

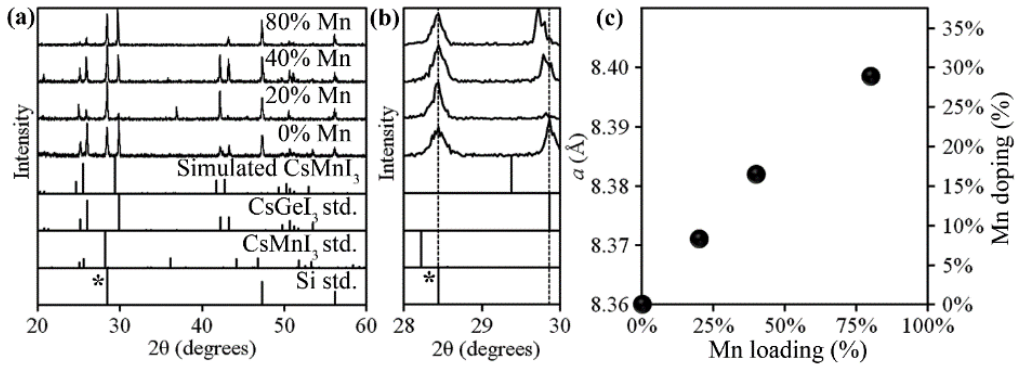

Figure 9. (a) Powder XRD patterns of $CsMn_xGe_{1-x}I_3$ (x = 0 – 0.8, MnI_2 synthetic loading) with silicon powder as an internal standard, denoted by an asterisk symbol(*). (b) A zoomed-in region between 28 and 30 degrees shows the most intense peak of $CsGeI_3$ shifts to lower 2 theta with increasing MnI_2 synthetic loading. (c) Lattice parameter *a* and manganese incorporation as a function of MnI_2 synthetic loading (%) for $CsMn_xGe_{1-x}I_3$ crystals.

Table 2. Structural parameters of $CsMn_xGe_{1-x}I_3$ perovskites.

MnI_2 synthetic loading	Lattice parameter (Å)	Mn incorporation	Bandgap (eV)
0%	8.358	0%	1.61
20%	8.369	8%	1.62
40%	8.380	16%	1.62
80%	8.397	29%	1.60

Doped samples exhibit similar optical properties and morphologies as undoped $CsGeI_3$ (Figure S6). Tauc plot shows all the band-edge spectral features of doped samples appear around 1.6 eV, which indicates the dopants at different concentrations have little effect on the electronic structure of the host perovskites. This is consistent with a previous study of manganese doped $CsPbX_3$ (X = Cl, Br and I) perovskites.[48] No photoluminescence has been observed from doped samples, which is reasonable because the bandgap of $CsGeI_3$ is lower than manganese emission bands.[47] A typical SEM image in Figure S5 displays the manganese doped perovskites are polycrystalline with crystal sizes in the micrometer scale.

We also tried to dope Mn^{2+} into $CsGeI_3$ nanocrystals prepared with a cysteammonium concentration of 0.50 M (10 molar equivalents). Powder XRD shows that $CsMn_xGe_{1-x}I_3$ nanocrystals have the same trigonal structure as the undoped $CsGeI_3$ without impurities (Figure 10a). Again, we used Si powder as an internal standard to calibrate the positions of $CsMn_xGe_{1-x}I_3$ nanocrystal patterns. The calibrated patterns exhibit a shift to lower 2 theta degrees with increasing MnI_2 synthetic loading, suggesting the presence of lattice expansion (Figure 10b). However, we also observed that the lattice parameter *a* of undoped $CsGeI_3$ nanocrystals is larger than that of bulk $CsGeI_3$ (Figure 10b) We suspect the lattice expansion of undoped nanocrystals is caused by the incorporation of cysteammonium cations into the $CsGeI_3$ lattice. Some cysteammonium cations may substitute Cs^+ sites or attach on the surface of nanocrystals and exert a tensile strain on the $CsGeI_3$ lattice. To test

this hypothesis, we estimated the ionic radius of cysteammonium cations as 2.83 Å based on the unit cell of cysteammonium chloride ($HS(CH_2)_2NH_3Cl$) (see Figure S7 for details of size estimation). This value is comparable to the ionic radii of organic cations in organometal perovskites, such as the guanidinium cation (2.78 Å) or ethylammonium cation (2.74 Å),[71] and this gives a tolerance factor t of 1.2. Values of t larger than 1 indicate that cysteammonium cations are too big to fit in the lattice. Cysteammonium is most likely attaches to the surface of the nanocrystals and applies a tensile strain on the $CsGeI_3$ lattice. To confirm the presence of cysteammonium in the nanocrystal samples, we performed CHN/S combustion elemental analysis. Results show the $CsGeI_3$ nanocrystal samples have average wt% of 2.59 ± 0.09 %C, 1.08 ± 0.05 %H, 1.43 ± 0.06%N and 3.29 ± 0.10 %S. The atom number ratio of C: H: N: S = 2: 11: 1: 1, which is in good agreement of cysteammonium cation formula $C_2H_8NS^+$. Therefore, the lattice expansion could be due to a synergic effect of incorporation of manganese and tensile strain from cysteammonium ligands. We can calculate manganese incorporation by Vegard's law if we offset the lattice expansion by cysteammonium ligands (Figure 10b). Up to 16% manganese doping in $CsGeI_3$ can be achieved when MnI_2 synthetic loading is 40%. MnI_2 synthetic loading over 40% leads to no precipitate in ice-water bath.

EPR Characterization. To confirm the presence of manganese ion dopants within the $CsGeI_3$ perovskite lattice, we utilized electron paramagnetic resonance (EPR) spectroscopy. The X-band EPR spectra of doped samples with 20% and 40% MnI_2 synthetic loadings exhibit typical hyperfine splitting signals consistent with high spin, octahedrally coordinated Mn^{2+}. EasySpin simulations of these EPR spectra results in a hyperfine splitting constant of A = 265 MHz that is consistent with previous studies of high spin octahedrally coordinated Mn^{2+} (Table 3 and 4).[72-78] We also collected the EPR spectrum of MnI_2 as a control. MnI_2 has a hyperfine splitting constant A of 265 MHz that

is also consistent with high-spin octahedral Mn^{2+}. The major difference between $CsMn_xGe_{1-x}I_3$ and MnI_2 is the zero-field splitting constant D, a parameter sensitive to distortion. D-values are usually small for hexacoordinate Mn(II) complexes and will increase with ligand sphere asymmetry.[79] No hyperfine splitting was observed in the 80% Mn sample, likely because excess Mn^{2+} can reduce spin-spin interactions between neighboring magnetic ions.[80] Unlike Mn: CdS, it is really hard to distinguish if Mn^{2+} sites are internal or on the surface in this system based on the values of hyperfine splitting constant A,[81] because no matter it is internal or external the A values are similar for octahedral Mn^{2+}. EPR spectra of the Mn-doped perovskite nanocrystals also confirm the presence of manganese (Figure 11). EasySpin simulations result in a hyperfine splitting constant A value of 265 MHz similar to both Mn-doped polycrystalline and MnI_2 samples, which suggests that Mn^{2+} cations are high-spin and octahedrally coordinated.

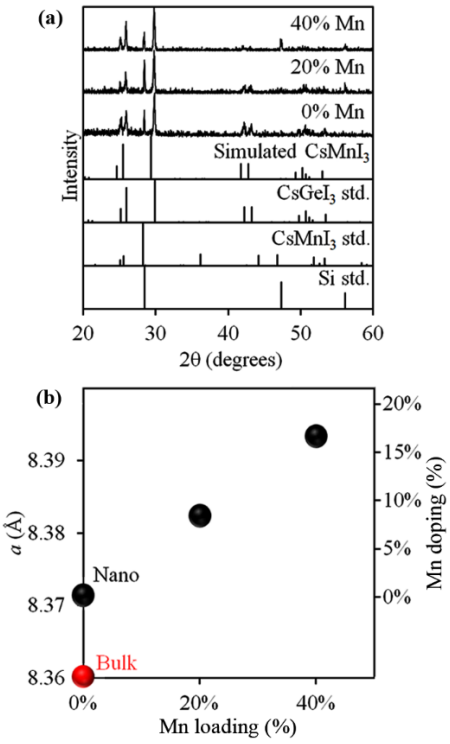

Figure 10. (a) Powder XRD patterns of $CsMn_xGe_{1-x}I_3$ (x = 0, 0.2 or 0.4, MnI_2 synthetic loading) nanocrystals with cysteammonium ligand concentration of 0.50 M. Silicon powder

is used as an internal standard. (b) Black balls are lattice parameter *a* and manganese incorporation as a function of MnI_2 synthetic loading (%) for $CsMn_xGe_{1-x}I_3$ nanocrystals. Red ball indicates the lattice parameter of $CsGeI_3$ in the absence of cysteammonium ligands.

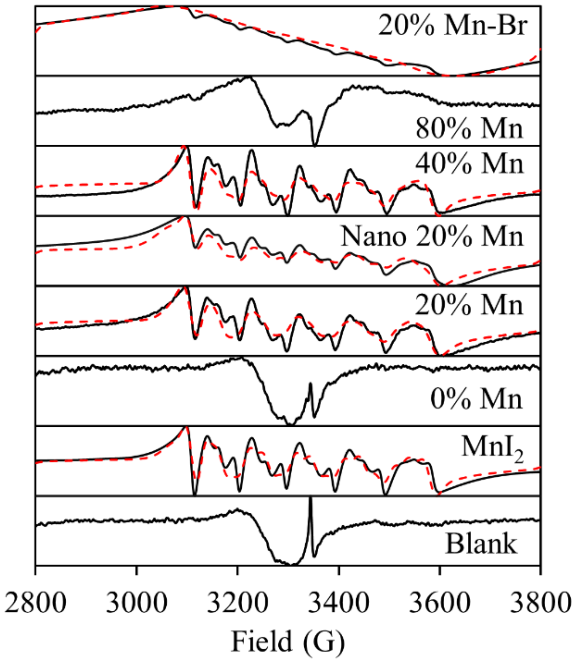

Figure 11. EPR spectra of bulk and nano Mn-doped $CsGeI_3$ perovskites and MnI_2 in ethanol at 10 K. All the samples don't have cysteammonium ligands in the reaction except Nano 20% Mn. Red dashed curves are simulated EPR spectra by the least-squares fitting. Note that manganese percentages are calculated from MnI_2 synthetic loading.

Table 3. EPR parameters for $CsMn_xGe_{1-x}I_3$ and MnI_2.

Parameters	MnI_2 synthetic loading, mol%			MnI_2
	20%Mn	Nano 20%Mn	40%Mn	
g	2.0023	2.0023	2.0023	2.0023
A (MHz)	265	265	265	265
D (MHz)	562	626	502	572
D strain (MHz)	623	642	546	701

Table 4. Comparison of EPR parameters.

Sample	Mn^{2+} site	EPR parameters		Reference
		g	A (MHz)	
Mn: $CsPbCl_3$	octahedral	n.a.	240	[48]
$[Mn(CH_3CN)_6]^{2+}$	octahedral	2.003	260	[73]
Mn: PbI_2	octahedral	$g_{\parallel} = 1.9955$ $g_{\perp} = 2.001$	220	[74]
$[Mn(MeOH)_6]^{2+}$	octahedral	2.0018	266	[76]
$[Mn(H_2O)_6]^{2+}$	octahedral	2.002	266	[76]

Conclusion

To address the concerns about the heavy element lead in conventional lead perovskites, we developed a synthetic route to germanium perovskites and their nanocrystals. $CsGeI_3$ exhibits a similar bandgap (1.6 eV) and corner-sharing octahedra network as lead perovskites that are potentially promising for photovoltaics. In addition, we have also successfully doped Mn^{2+} into $CsGeI_3$ lattice. XRD patterns show a lattice expansion with increasing manganese iodide loading, which we believed is caused by the substitution of Ge^{2+} by larger Mn^{2+}. The manganese incorporation percentage is up to 29% according to Vegard's law. EPR analysis also confirms the presence of Mn^{2+} and indicates Mn^{2+} sites are highly distorted, which is in good agreement with Ge^{2+} sites in $CsGeI_3$. Size control of $CsGeI_3$ perovskite nanocrystals is achieved by using cysteammonium cations as capping ligands. Diffraction peak broadening in powder XRD and TEM images corroborate the successful size control without introducing impurities. Diffuse reflectance measurements also reveal a bandgap blue-shift of 0.05 eV in the nanocrystals. Because the sizes of the nanocrystals are much larger than the Bohr radius, it is unlikely this blue shift is the result of quantum confinement. We also noticed that the lattice parameter for

nanocrystals is larger than that observed in the bulk, possibly caused by tensile strain from the bulky organic cations on the surface. Mn^{2+}-doped nanocrystals also have a larger lattice parameter, which is a synergetic effect of manganese incorporation and surface strain. EPR analysis on nanocrystals confirms the presence of high spin Mn^{2+} doping into the highly distorted octahedral sites. We expect these results will extend the arsenal of perovskites, especially the lead-free ones, beyond photovoltaics and to the fields of spintronics and magnetic data storage.

Acknowledgement

This research is supported by the U.S. Department of Energy, Office of Basic Energy Sciences, Division of Chemical Sciences, Geosciences, and Biosciences through the Ames Laboratory. The Ames Laboratory is operated for the U.S. Department of Energy by Iowa State University under Contract No. DE-AC02- 07CH11358.

References

(1) Kojima, A.; Teshima, K.; Shirai, Y.; Miyasaka, T. Organometal Halide Perovskites as Visible-Light Sensitizers for Photovoltaic Cells. *J. Am. Chem. Soc.* **2009**, *131*, 6050–6051.

(2) National Renewable Energy Laboratory. Best Research-Cell Efficiencies Chart. https://www.nrel.gov/pv/assets/images/efficiency_chart.jpg (accessed on July 19, 2017)

(3) Zhou, H.; Chen, Q.; Li, G.; Luo, S.; Song, T.-b.; Duan, H.-S.; Hong, Z.; You, J.; Liu, Y.; Yang, Y. Interface Engineering of Highly Efficient Perovskite Solar Cells. *Science* **2014**, *345*, 542–546.

(4) Shi, D.; Adinolfi, V.; Comin, R.; Yuan, M.; Alarousu, E.; Buin, A.; Chen, Y.; Hoogland, S.; Rothenberger, A.; Katsiev, K.; Losovyj, Y.; Zhang, X.; Dowben, P. A.; Mohammed, O.

F.; Sargent, E. H.; Bakr, O. M. Low Trap-state Density and Long Carrier Diffusion in Organolead Trihalide Perovskite Single Crystals. *Science* **2015**, *347*, 519–522.

(5) Kazim, S.; Nazeeruddin, M. K.; Grätzel, M.; Ahmad, S. Perovskite as Light Harvester: A Game Changer in Photovoltaics. *Angew. Chem. Int. Ed.* **2014,** *53*, 2812–2824.

(6) Dong, Q.; Fang, Y.; Shao, Y.; Mulligan, P.; Qiu, J.; Cao, L.; Huang, J. Electron-Hole Diffusion Lengths > 175 μm in Solution-Grown $CH_3NH_3PbI_3$ Single Crystals. *Science* **2015,** *347*, 967–970.

(7) Rosales, B. A.; Men, L.; Cady, S. D.; Hanrahan, M. P.; Rossini, A. J.; Vela, J. Persistent Dopants and Phase Segregation in Organolead Mixed-Halide Perovskites. *Chem. Mater.* **2016**, *28*, 6848−6859.

(8) Rosales, B. A.; Hanrahan, M. P.; Boote, B. W.; Rossini, A. J.; Smith, E. A.; Vela, J., Lead Halide Perovskites: Challenges and Opportunities in Advanced Synthesis and Spectroscopy. *ACS Energy Lett.* **2017**, *2*, 906–914.

(9) Schmidt, L. C.; Pertegás, A.; González-Carrero, S.; Malinkiewicz, O.; Agouram, S.; Mínguez Espallargas, G.; Bolink, H. J.; Galian, R. E.; Pérez-Prieto, J. Nontemplate Synthesis of $CH_3NH_3PbBr_3$ Perovskite Nanoparticles. *J. Am. Chem. Soc.* **2014**, *136*, 850–853.

(10) D'Innocenzo, V.; Srimath Kandada, A. R.; De Bastiani, M.; Gandini, M.; Petrozza, A. Tuning the Light Emission Properties by Band Gap Engineering in Hybrid Lead Halide Perovskite. *J. Am. Chem. Soc.* **2014**, *136*, 17730–17733.

(11) Zhang, F.; Zhong, H.; Chen, C.; Wu, X.-g.; Hu, X.; Huang, H.; Han, J.; Zou, B.; Dong, Y. Brightly Luminescent and Color-Tunable Colloidal $CH_3NH_3PbX_3$ (X = Br, I, Cl) Quantum Dots: Potential Alternatives for Display Technology. *ACS Nano* **2015,** *9*, 4533–4542.

(12) Protesescu, L.; Yakunin, S.; Bodnarchuk, M. I.; Krieg, F.; Caputo, R.; Hendon, C. H.; Yang, R. X.; Walsh, A.; Kovalenko, M. V. Nanocrystals of Cesium Lead Halide Perovskites ($CsPbX_3$, X= Cl, Br, and I): Novel Optoelectronic Materials Showing Bright Emission with Wide Color Gamut. *Nano Lett.* **2015**, *15*, 3692–3696.

(13) Zhu, F.; Men, L.; Guo, Y.; Zhu, Q.; Bhattacharjee, U.; Goodwin, P. M.; Petrich, J. W.; Smith, E. A.; Vela, J. Shape Evolution and Single Particle Luminescence of Organometal Halide Perovskite Nanocrystals. *ACS nano* **2015**, *9*, 2948–2959.

(14) Zhu, H.; Fu, Y.; Meng, F.; Wu, X.; Gong, Z.; Ding, Q.; Gustafsson, M.V.; Trinh, M.T.; Jin, S.; Zhu, X.Y. Lead Halide Perovskite Nanowire Lasers with Low Lasing Thresholds and High Quality Factors. *Nat. mater.* **2015**, *14*, 636–642.

(15) Wang, Y.; Li, X.; Zhao, X.; Xiao, L.; Zeng, H.; Sun, H. Nonlinear Absorption and Low-Threshold Multiphoton Pumped Stimulated Emission from All-Inorganic Perovskite Nanocrystals. *Nano Lett.* **2016**, *16*, 448–453.

(16) Yakunin, S.; Protesescu, L.; Krieg, F.; Bodnarchuk, M. I.; Nedelcu, G.; Humer, M.; De Luca, G.; Fiebig, M.; Heiss, W.; Kovalenko, M. V. Low-Threshold Amplified Spontaneous Emission and Lasing from Colloidal Nanocrystals of Caesium Lead Halide Perovskites. *Nat. Comm.* **2015**, *6*, 8056-1–8056-8.

(17) Pan, J.; Sarmah, S. P.; Murali, B.; Dursun, I.; Peng, W.; Parida, M. R.; Liu, J.; Sinatra, L.; Alyami, N.; Zhao, C.; Alarousu, E.; Ng, T. K.; Ooi, B. S.; Bakr, O. M.; Mohammed, O. F. Air-Stable Surface-Passivated Perovskite Quantum Dots for Ultra-Robust, Single- and Two-Photon-Induced Amplified Spontaneous Emission. *J. Phys. Chem. Lett.* **2015**, *6*, 5027–5033.

(18) Gidlow, D. A. Lead Toxicity. *Occup. Med.* **2004**, *52*, 76–81.

(19) Babayigit, A; Ethirajan, A.; Muller, M.; Conings, B. Toxicity of Organometal Halide Perovskite Solar Cells. *Nat. Mater*. **2016**, *15*, 247–251.

(20) Serrano-Lujan, L.; Espinosa, N.; Larsen-Olsen, T. T.; Abad, J.; Urbina, A.; Krebs, F. C. Tin- and Lead-Based Perovskite Solar Cells under Scrutiny: An Environmental Perspective. *Adv. Energy Mater.* **2015**, *5*, 1501119-1–1501119-5.

(21) Stoumpos, C. C.; Frazer, L.; Clark, D. J.; Kim, Y. S.; Rhim, S. H.; Freeman, A. J.; Ketterson, J. B.; Jang, J. I.; Kanatzidis, M. G. Hybrid Germanium Iodide Perovskite Semiconductors: Active Lone Pairs, Structural Distortions, Direct and Indirect Energy Gaps, and Strong Nonlinear Optical Properties. *J. Am. Chem. Soc.* **2015**, 137, 6804–6819.

(22) Stoumpos, C. C.; Malliakas, C. D.; Kanatzidis, M. G. Semiconducting Tin and Lead Iodide Perovskites with Organic Cations: Phase Transitions, High Mobilities, and Near-Infrared Photoluminescent Properties. *Inorg. Chem.* **2013**, *52*, 9019–9038.

(23) Wang, K.; Liang, Z.; Wang, X.; Cui, X. Lead Replacement in $CH_3NH_3PbI_3$ Perovskites. *Adv. Electron. Mater.* **2015**, *1*, 1500089-1–1500089-8.

(24) Hu, H.; Dong, B.; Zhang, W. Low-Toxic Metal Halide Perovskites: Opportunities and Future Challenges. *J. Mater. Chem. A* **2017**, *5*, 11436–11449

(25) Ogomi, Y.; Morita, A.; Tsukamoto, S.; Saitho, T.; Fujikawa, N.; Shen, Q.; Toyoda, T.; Yoshino, K.; Pandey, S. S.; Ma, T. $CH_3NH_3Sn_xPb_{(1-x)}I_3$ Perovskite Solar Cells Covering up to 1060 nm. *J. Phys. Chem. Lett.* **2014**, *5*, 1004–1011.

(26) Noel, N. K.; Stranks, S. D.; Abate, A.; Wehrenfennig, C.; Guarnera, S.; Haghighirad, A. A.; Sadhanala, A.; Eperon, G. E.; Pathak, S. K.; Johnston, M. B.; Petrozza, A.; Herz, L. M.; Snaith, H. J. Lead-Free Organic-Inorganic Tin Halide Perovskites for Photovoltaic Applications. *Energy Environ. Sci.* **2014**, *7*, 3061–3068.

(27) Babayigit, A.; Thanh, D. D.; Ethirajan, A.; Manca, J.; Muller, M.; Boyen, H. G.; Conings, B. Assessing the Toxicity of Pb- and Sn-Based Perovskite Solar Cells in Model Organism *Danio Rerio*. Sci. Rep. **2016**, *6*, 18721-1–18721-11.

(28) Park, B. W.; Philippe, B.; Zhang, X.; Rensmo, H.; Boschloo, G.; Johansson, E. M. Bismuth Based Hybrid Perovskites $A_3Bi_2I_9$ (A: Methylammonium or Cesium) for Solar Cell Application. *Adv. Mater.* **2015**, *27*, 6806–6813.

(29) Leng, M.; Chen, Z.; Yang, Y.; Li, Z.; Zeng, K.; Li, K.; Niu, G.; He, Y.; Zhou, Q.; Tang, J. Lead-Free, Blue Emitting Bismuth Halide Perovskite Quantum Dots. *Angew. Chem. Int. Ed.* **2016**, *55*, 15012–15016.

(30) Lehner, A. J.; Fabini, D. H.; Evans, H. A.; Hébert, C. A.; Smock, S. R.; Hu, J.; Wang, H.; Zwanziger, J. W.; Chabinyc, M. L.; Seshadri, R. Crystal and Electronic Structures of Complex Bismuth Iodides A3Bi2I9 (A= K, Rb, Cs) Related to Perovskite: Aiding the Rational Design of Photovoltaics. *Chem. Mater.* **2015**, *27*, 7137–7148.

(31) Volonakis, G.; Filip, M. R.; Haghighirad, A. A.; Sakai, N.; Wenger, B.; Snaith, H. J.; Giustino, F. Lead-Free Halide Double Perovskites via Heterovalent Substitution of Noble Metals. *J. Phys. Chem. Lett.* **2016**, *7*, 1254–1259.

(32) Slavney, A. H.; Hu, T.; Lindenberg, A. M.; Karunadasa, H. I. A Bismuth-Halide Double Perovskite with Long Carrier Recombination Lifetime for Photovoltaic Applications. *J. Am. Chem. Soc.* **2016**, *138*, 2138–2141.

(33) McClure, E. T.; Ball, M. R.; Windl, W.; Woodward, P. M. Cs_2AgBiX_6 (X = Br, Cl): New Visible Light Absorbing, Lead-Free Halide Perovskite Semiconductors. *Chem. Mater.* **2016**, *28*, 1348–1354.

(34) Wei, F.; Deng, Z.; Sun, S.; Zhang, F.; Evans, D. M.; Kieslich, G.; Tominaka, S.; Carpenter, M. A.; Zhang, J.; Bristowe, P. D.; Cheetham, A. K. Synthesis and Properties of a Lead-Free Hybrid Double Perovskite: $(CH_3NH_3)_2AgBiBr_6$. *Chem. Mater.* **2017**, *29*, 1089–1094.

(35) Gerber, G. B.; Léonard, A. Mutagenicity, Carcinogenicity and Teratogenicity of Germanium Compounds. *Mutat. Res.*, **1997**, *387*, 141–146.

(36) Kanisawa, M.; Schroeder, H. A. Life Term Studies on the Effect of Trace Elements on Spontaneous Tumors in Mice and Rats. *Cancer Res.* **1969**, *29*, 892–895.

(37) Tang, L. C.; Chang, Y. C.; Huang, J. Y.; Lee, M. H.; Chang, C. S. First Principles Calculations of Linear and Second-Order Optical Responses in Rhombohedrally Distorted Perovskite Ternary Halides, $CsGeX_3$ (X = Cl, Br, and I). *Jpn. J. Appl. Phys.* **2009**, *48*, 112402-1–112402-9.

(38) Krishnamoorthy, T.; Ding, H.; Yan, C.; Leong, W. L.; Baikie, T.; Zhang, Z.; Sherburne, M.; Li, S.; Asta, M.; Mathews, N.; Mhaisalkar, S. G. Lead-Free Germanium Iodide Perovskite Materials for Photovoltaic Applications. *J. Mater. Chem. A* **2015**, *3*, 23829–23832.

(39) Sun, P. P.; Li, Q. S.; Yang, L. N.; Li, Z. S. Theoretical Insights into a Potential Lead-Free Hybrid Perovskite: Substituting Pb^{2+} with Ge^{2+}. *Nanoscale*, **2016**, *8*, 1503–1512.

(40) Huang, L. Y.; Lambrecht, W. R. Electronic Band Structure Trends of Perovskite Halides: Beyond Pb and Sn to Ge and Si. *Phys. Rev. B* **2016**, *93*, 195211-1–195211-8.

(41) Sun, P. P.; Li, Q. S.; Feng, S.; Li, Z. S. Mixed Ge/Pb Perovskite Light Absorbers with an Ascendant Efficiency Explored from Theoretical View. *Phys. Chem. Chem. Phys.* **2016**, *18*, 14408–14418.

(42) Ju, M.; Dai, J.; Ma, L.; Zeng, X. Lead-Free Mixed Tin and Germanium Perovskites for Photovoltaic Application. *J. Am. Chem. Soc.* **2017**, *139*, 8038–8043.

(43) Norris, D. J.; Efros, A. L.; Erwin, S. C. Doped Nanocrystals. *Science* **2008**, *319*, 1776–1779.

(44) Erwin, S. C.; Zu, L.; Haftel, M. I.; Efros, A. L. Doping Semiconductor Nanocrystals. *Nature* **2005**, *436*, 91–94.

(45) Buonsanti, R.; Milliron, D. J. Chemistry of Doped Colloidal Nanocrystals. *Chem. Mater.* **2013**, *25*, 1305–1317.

(46) Beaulac, R.; Archer, P. I.; Ochsenbein, S. T.; Gamelin, D. R. Mn^{2+}-Doped CdSe Quantum Dots: New Inorganic Materials for Spin-Electronics and Spin-Photonics. *Adv. Funct. Mater.* **2008**. *18*, 3873–3891.

(47) Liu, W. Y.; Lin, Q. L.; Li, H. B.; Wu, K. F.; Robel, I.; Pietryga, J. M.; Klimov, V. I. Mn^{2+}-Doped Lead Halide Perovskite Nanocrystals with Dual-Color Emission Controlled by Halide Content. *J. Am. Chem. Soc.* **2016,** 138, 14954–14961.

(48) Parobek, D.; Roman, B. J.; Dong, Y. T.; Jin, H.; Lee, E.; Sheldon, M.; Son, D. H. Exciton-to-Dopant Energy Transfer in Mn-Doped Cesium Lead Halide Perovskite Nanocrystals. *Nano Lett.* **2016,** 16, 7376–7380.

(49) Mir, W. J.; Jagadeeswararao, M.; Das, S.; Nag, A. Colloidal Mn-Doped Cesium Lead Halide Perovskite Nanoplatelets. *ACS Energy Lett.* **2017**, *2*, 537–543.

(50) Liu, H.; Wu, Z.; Shao, J.; Yao, D.; Gao, H.; Liu, Y.; Yu, W.; Zhang, H.; Yang, B. $CsPb_xMn_{1-x}Cl_3$ Perovskite Quantum Dots with High Mn Substitution Ratio. *ACS nano* **2017**, *11*, 2239–2247.

(51) Shannon, R. D.; Prewitt, C. T. Effective Ionic Radii in Oxides and Fluorides. *Acta Crystallogr. Sect. B.* **1969**, *25*, 925–946.

(52) Hume-Rothery, W. *The Structures of Alloys of Iron: An Elementary Introduction*. Elsevier: 2013.

(53) Goldschmidt, V.M. Die Gesetze der Krystallochemie. *Naturwissenschaften* **1926**, *14*, 477–485.

(54) Li, Z.; Yang, M.; Park, J. S.; Wei, S. H.; Berry, J. J.; Zhu, K. Stabilizing Perovskite Structures by Tuning Tolerance Factor: Formation of Formamidinium and Cesium Lead Iodide Solid-State Alloys. *Chem. Mater.* **2015**, *28*, 284–292.

(55) Tang, L.C.; Huang, J.Y.; Chang, C.S.; Lee, M.H.; Liu, L.Q. New Infrared Nonlinear Optical Crystal $CsGeBr_3$: Synthesis, Structure and Powder Second-Harmonic Generation Properties. *J. Phys. Condens. Matter* **2005**, *17*, 7275–7286.

(56) Seo, D. K.; Gupta, N.; Whangbo, M. H.; Hillebrecht, H.; Thiele, G. Pressure-Induced Changes in the Structure and Band Gap of $CsGeX_3$ (X = Cl, Br) Studied by Electronic Band Structure Calculations. *Inorg. Chem.* **1998**, *37*, 407–410.

(57) Luo, L.; Men, L.; Liu, Z.; Mudryk, Y.; Zhao, X.; Yao, Y.; Park, J. M.; Shinar, R.; Shinar, J.; Ho, K.-M.; Perakis, I. E.; Vela, J.; Wang, J. Ultrafast Terahertz Snapshots of Excitonic Rydberg States and Electronic Coherence in an Organometal Halide Perovskite. *Nature Commun.* **2017**, *8*, 15565-1–15565-8.

(58) Shockley, W.; Queisser, H. J. Detailed Balance Limit of Efficiency of P-N Junction Solar Cells. *J. Appl. Phys.* **1961**, *32*, 510–519.

(59) Ming, W. M.; Shi, H. L.; Du, M. H. Large Dielectric Constant, High Acceptor Density, and Deep Electron Traps in Perovskite Solar Cell Material $CsGeI_3$. *J. Mater. Chem. A* **2016**, *4*, 13852–13858.

(60) Saparov, B.; Mitzi, D. B. Organic–Inorganic Perovskites: Structural Versatility for Functional Materials Design. *Chem. Rev.* **2016**, 116, 4558–4596.

(61) Dou, L. T.; Wong, A. B.; Yu, Y.; Lai, M. L.; Kornienko, N.; Eaton, S. W.; Fu, A.; Bischak, C. G.; Ma, J.; Ding, T. N.; Ginsberg, N. S.; Wang, L. W.; Alivisatos, A. P.; Yang, P. D. Atomically Thin Two-Dimensional Organic-Inorganic Hybrid Perovskites. *Science* **2015**, *349*, 1518−1521.

(62) Weidman, M. C.; Goodman, A. J.; Tisdale, W. A. Colloidal Halide Perovskite Nanoplatelets: An Exciting New Class of Semiconductor Nanomaterials. *Chem. Mater.* **2017**, *29*, 5019–5030.

(63) Tyagi, P.; Arveson, S. M.; Tisdale, W. A. Colloidal Organohalide Perovskite Nanoplatelets Exhibiting Quantum Confinement. *J. Phys. Chem. Lett.* **2015**, *6*, 1911−1916.

(64) Quan, L. N.; Yuan, M.; Comin, R.; Voznyy, O.; Beauregard, E. M.; Hoogland, S.; Buin, A.; Kirmani, A. R.; Zhao, K.; Amassian, A.; Kim, D. H.; Sargent, E. H. Ligand-Stabilized Reduced-Dimensionality Perovskites. *J. Am. Chem. Soc.* **2016**, *138*, 2649−2655.

(65) Sichert, J. A.; Tong, Y.; Mutz, N.; Vollmer, M.; Fischer, S.; Milowska, K. Z.; García Cortadella, R.; Nickel, B.; Cardenas-Daw, C.; Stolarczyk, J. K.; Urban, A. S. Quantum Size Effect in Organometal Halide Perovskite Nanoplatelets. *Nano Lett.* **2015**, *15*, 6521–6527.

(66) Freppon, D. J.; Men, L.; Burkhow, S. J.; Petrich, J. W.; Vela, J.; Smith, E. A. Photophysical Properties of Wavelength-Tunable Methylammonium Lead Halide Perovskite Nanocrystals. *J. Mater. Chem. C* **2017**, *5*, 118–126.

(67) Men, L.; White, M. A.; Andaraarachchi, H.; Rosales, B. A.; Vela, J. Synthetic Development of Low Dimensional Materials. *Chem. Mater.* **2017**, *29*, 168–175.

(68) Yu, P. Y.; Cardona, M. *Fundamentals of semiconductors*; Springer, 1996.

(69) Vegard, L. Die Konstitution der Mischkristalle und die Raumfüllung der Atome. *Eur. Phys. J. A* **1921**, *5*, 17–26.

(70) Denton, A. R.; Ashcroft, N. W. Vegard ’s Law. *Phys. Rev. A: At., Mol., Opt. Phys.* **1991**, *43*, 3161–3164.

(71) Kieslich, G.; Sun, S.; Cheetham, A.K. Solid-State Principles Applied to Organic–Inorganic Perovskites: New Tricks for an Old Dog. *Chem. Sci.* **2014**, *5*, 4712–4715.

(72) Chan, S. I.; Fung, B. M.; Lütje, H. Electron Paramagnetic Resonance of Mn (II) Complexes in Acetonitrile. *J. Chem. Phys.* **1967**, *47*, 2121–2130.

(73) Motsnyi, F. V.; Dorogan, V. G.; Kovalyuk, Z. D.; Okulov, S. M.; Yaremko, A. M. Spectroscopic Studies of 2H-PbI_2(Mn) Layered Crystals. *Phys. Status Solidi B* **2005**, *242*, 2427–2432.

(74) Van der Valk, H. J. L.; Meertens, P.; Haas, C. Electron Paramagnetic Resonance of Divalent V, Mn, and Co in Single Crystals of CdI_2 and PbI_2. *Phys. Status Solidi B* **1978**, *87*, 135–144.

(75) Levanon, H.; Luz, Z. ESR and NMR of Mn (II) Complexes in Methanol. *J. Chem. Phys*. **1968**, *49*, 2031–2040.

(76) Cape, J. A.; White, R. L.; Feigelson, R. S. EPR Study of the Structure of $CsPbCl_3$. *J. Appl. Phys.* **1969**, *40*, 5001–5005.

(77) Levi, Z.; Raitsimring, A. M.; Goldfarb, D. ESR and Electron Spin-Echo Studies of $MnAlPO_5$. *J. Chem. Phys*. **1991**, *95*, 7830–7838.

(78) Rapheal, P. F.; Manoj, E.; Kurup, M. P. Syntheses and EPR Spectral Studies of Manganese (II) Complexes Derived from Pyridine-2-Carbaldehyde Based N(4)-Substituted Thiosemicarbazones: Crystal Structure of One Complex. *Polyhedron* **2007**, *26*, 5088–5094.

(79) Boča, R. Zero-Field Splitting in Metal Complexes. *Coord. Chem. Rev.* **2004**, *248*, 757–815.

(80) Thompson, M. J.; Blakeney, K. J.; Cady, S. D.; Reichert, M. D.; Pilar-Albaladejo, J. D.; White, S. T.; Vela, J. Cu_2ZnSnS_4 Nanorods Doped with Tetrahedral, High Spin Transition Metal Ions: Mn^{2+}, Co^{2+}, and Ni^{2+}. *Chem. Mater.* **2016**, *28*, 1668–1677.

(81) Guo, B. C.; Pang, Q.; Yang, C. L.; Ge, W. K.; Yang, S. H.; Wang, J. N. Reverse Micelles Synthesis and Optical Characterization of Manganese Doped CdSe Quantum Dots. *AIP Conf. Proc.* **2004**, *772*, 605–606.

Supporting Information

Table S1. Bandgap comparison between Pb- and Ge-based perovskites.

Compositions	Reported experiment bandgap (bulk, eV)	Experiment bandgap (bulk, eV)	Bohr radius (nm)
$CsGeCl_3$	3.67, 3.43	-	-
$CsGeBr_3$	2.32, 2.38	2.36	-
$CsGeI_3$	1.60	1.60	**4, 5**
$CsPbCl_3$	3.0	-	5
$CsPbBr_3$	2.2	-	7
$CsPbI_3$	1.7	-	12
$CH_3NH_3PbCl_3$	3.1	3.11	-
$CH_3NH_3PbBr_3$	2.3	2.36	2
$CH_3NH_3PbI_3$	1.5	1.62	2.2

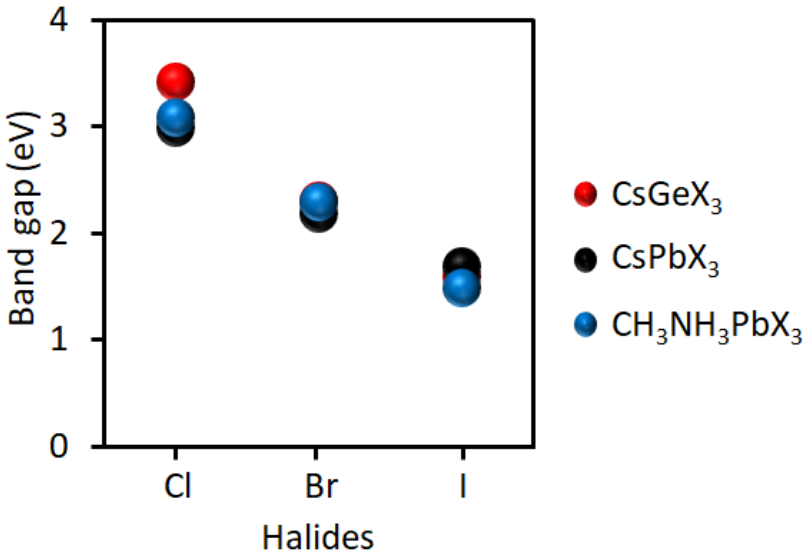

Figure S1. Bandgap comparison of $CsGeX_3$, $CsPbX_3$ and $CH_3NH_3PbX_3$ (X = Cl, Br and I) perovskites.

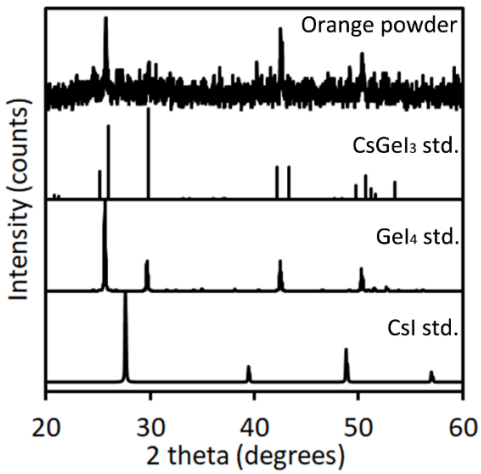

Figure S2. XRD pattern of the orange pattern. Major diffraction peaks match with GeI_4 standard pattern.

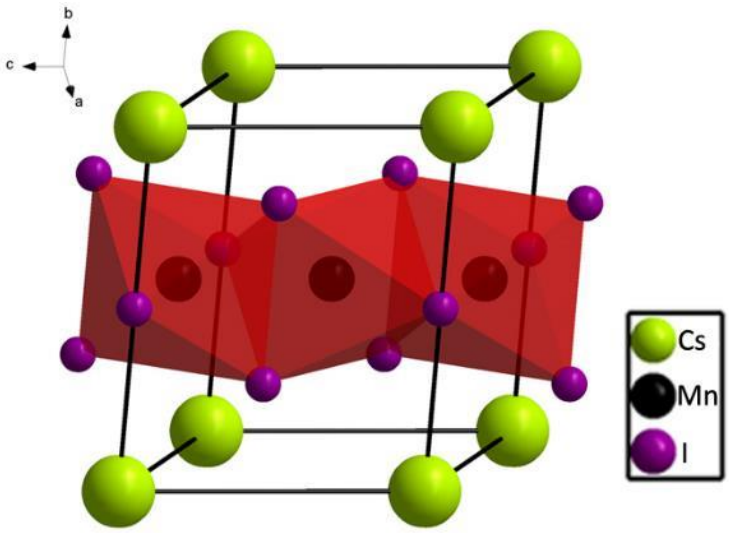

Figure S3. A unit cell of $CsMnI_3$ perovskites.

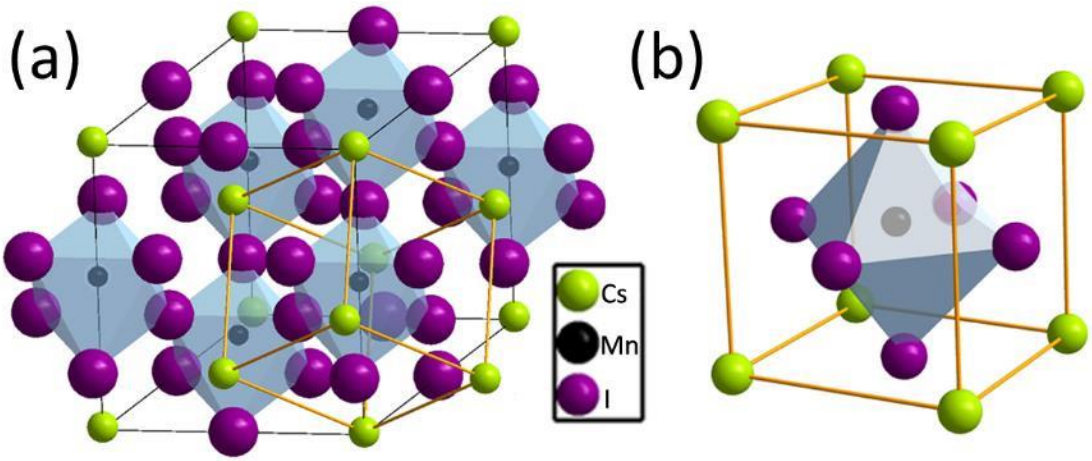

Figure S4. (a) unit cell of simulated $CsMnI_3$ and (b) octahedral Mn(II) coordination geometry of $CsMn_xGe_{1-x}I_3$.

$CsGeI_3$ has a trigonal structure with a = 8.3582 Å and c = 10.6098 Å. High spin octahedral Mn^{2+} has an ionic size of 0.97 Å whereas the diameter of Ge^{2+} is 0.87 Å. Assuming the central atoms in the octahedra are in contact with the surrounding halide anions, by substituting Ge^{2+} with Mn^{2+}, this will expand the octahedra by 0.1 Å. This leads to an expansion of the edge of the small cube in Figure S3(b) by 0.1 Å. Since the longer edge c in Fig S3(a) is the space diagonal of the small cube in Figure S3(b), 0.1 Å expansion in the octahedral will result in an expansion of 0.1 Å × $\sqrt{3}$ = 0.1732 Å for the longer edge c, which gives the length of c axis 10.6098 Å + 0.1732 Å = 10.7830 Å. Since the simulated

$CsMnI_3$ retains the structure of $CsGeI_3$, they should have the same value of c/a, which is 1.2694. Therefore, the shorter edge of the simulated $CsMnI_3$ should be 8.4946 Å. Knowing the lattice parameters of the simulated $CsMnI_3$ unit cells, we can generate an XRD standard pattern as a reference to calculate manganese incorporation.

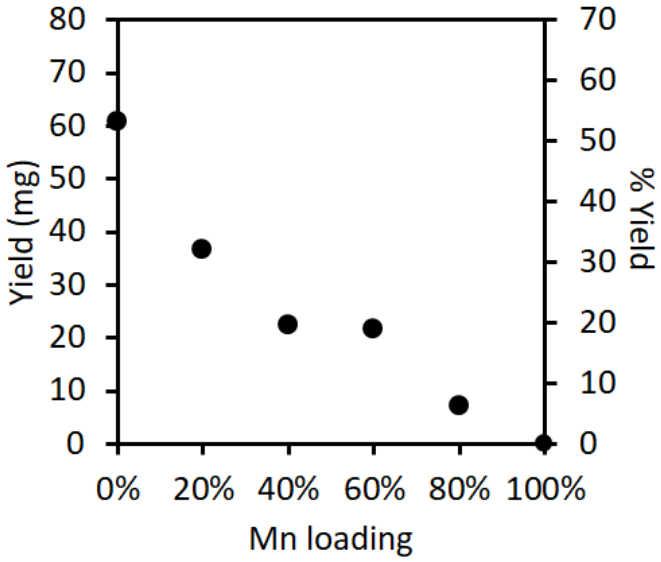

Figure S5. $CsMn_xGe_{1-x}I_3$ reaction yields as a function of manganese synthetic loading.

Table S1. $CsMn_xGe_{1-x}I_3$ reaction yields.

Mn synthetic loading	Final weight (mg)	%Yield
0%	60.8	51.9%
20%	36.7	31.8%
40%	22.3	19.0%
60%	21.6	18.9%
80%	7.0	6.1%
100%	0	0%

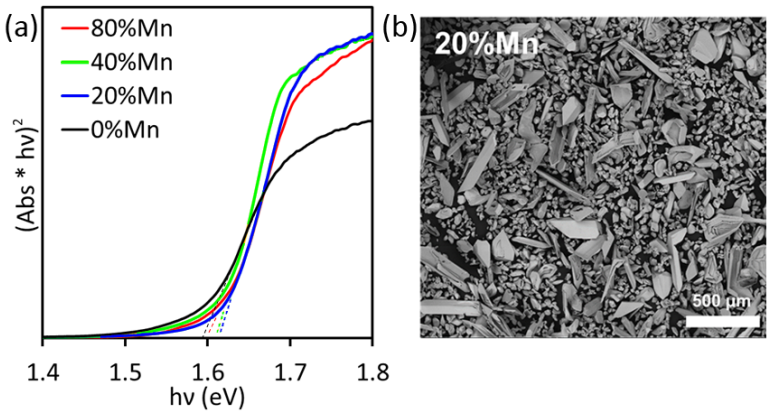

Figure S6. Tauc plot (a) and a typical SEM image (b) of $CsMn_xGe_{1-x}I_3$ crystals.

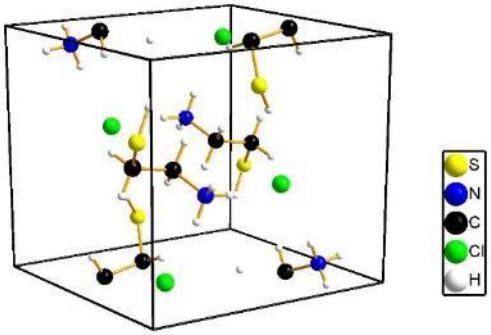

Figure S7. Unit cell of cysteammonium chloride.

Size Estimation of Cysteammonium Cation. The volume of cysteammonium chloride unit cell V(unit cell) = 560 $Å^3$ and Z = 4. Radius of Cl^- is 1.67 Å. If we assume cysteammonium cations and chloride anions are spheres, the volume of one cation should be $V(HSCH_2CH_2NH_3^+) = V(\text{unit cell})/4 - V(Cl^-) = 120.5\ Å^3$. Therefore, radius of cysteammonium cation should be 283 pm.

CHAPTER 5. GERMANIUM–TIN/CADMIUM SULFIDE CORE/SHELL NANOCRYSTALS WITH ENHANCED NEAR-INFRARED PHOTOLUMINESCENCE

Reprinted with permission from *Chem. Mater.* **2017**, *29*, 6012–6021.

Brett W. Boote, Long Men, Himashi P. Andaraarachchi, Ujjal Bhattacharjee, Jacob W. Petrich, Javier Vela, Emily A. Smith

Abstract

$Ge_{1-x}Sn_x$ alloy nanocrystals and $Ge_{1-x}Sn_x$ core/shell nanocrystals were prepared *via* solution phase synthesis and their size, composition, and optical properties were characterized. The diameter of the nanocrystal samples ranged from 6 to 13 nm. The crystal structure of the $Ge_{1-x}Sn_x$ materials was consistent with cubic diamond phase while the CdS shell was consistent with the zinc blende polytype. Inclusion of Sn alone does not result in enhanced photoluminescence intensity, however, adding an epitaxial CdS shell onto the $Ge_{1-x}Sn_x$ nanocrystals does enhance the photoluminescence up to 15× over Ge/CdS nanocrystals with a pure Ge core. More effective passivation of surface defects—and a consequent decrease in surface oxidation—by the CdS shell as a result of improved epitaxy (smaller lattice mismatch) is the most likely explanation for the increased photoluminescence observed for the $Ge_{1-x}Sn_x$/CdS materials. With enhanced photoluminescence in the near-infrared, $Ge_{1-x}Sn_x$ core/shell nanocrystals might be useful alternatives to other materials for energy capture and conversion applications and as imaging probes.

Introduction

Ge-based materials have garnered significant attention recently as alternatives to other well-studied luminescent semiconductors, such as cadmium and lead

chalcogenides.[1,2] Materials made of elemental Ge have band gaps in the 0.67 to 1.6 eV range for bulk and highly confined (~2-3 nm) nanocrystals, respectively.[3] The large blue shift in the band gap of the nanocrystals is due to size-dependent quantum confinement. Though prone to oxidation when uncoated, Ge nanocrystals have been shown to exhibit increased stability as well as enhanced photoluminescence when a suitable shell is added.[4,5]

Ge initially would seem to have limited utility in energy applications due to its inherent indirect band gap, which lowers its absorption cross-section and quantum yields. Recent reports suggest incorporation of Sn into Ge nanocrystals and thin films should produce a more direct band gap as a result of lattice strain.[6-8] For thin films, modifying the substrate on which the films are grown also allows the strain to be tuned while keeping the Sn composition constant.[9] A careful study of the bowing parameter on $Ge_{1-x}Sn_x$ films showed the crossover Sn content to be x = 0.087, which was higher than previously predicted.[10] It has also been shown by Senaratne *et al.* that n-type doping of $Ge_{1-x}Sn_x$ films enhances the photoluminescence.[11] Recently, Stange *et al.* demonstrated a strain-dependent indirect-to-direct band gap transition in $Ge_{0.875}Sn_{0.125}$ thin films grown on Ge buffer layers.[12] Band gap characteristics of related Ge-rich $Ge_{1-x}Si_x$ films have also been studied as a step toward the design of ternary systems based on Si, Ge, and Sn.[2]

Over the last decade, various methods to prepare Ge nanocrystals have been developed. Reduction of germanium halides ($GeCl_4$, $GeBr_2$, GeI_2 or GeI_4) using strong reducing agents ($NaBH_4$, $LiAlH_4$, etc.) in the presence of suitable surfactants [oleylamine, octadecene (ODE), trioctylphosphine (TOP)] is widely used to make monodisperse Ge nanocrystals.[13-22] Heating a solution of $GeBr_2$ or GeI_2 with a surfactant has also been shown to generate Ge nanocrystals.[23-25] Co-reduction of GeI_2 and GeI_4 is another common strategy for generating Ge nanocrystals in the ~2-20nm size regime, where the precursor ratio

controls the particle size.[3, 26-30] The polymerization of $[Ge_9]^{4-}$ or other related Zintl ions, both with and without linking cations such as Ge^{4+} or Pt^{2+}, generates highly ordered, porous Ge nanocrystals.[31-35] Other preparations involve reduction of Ge-rich oxides,[36-41] heat-assisted reduction of the GeH_2 Wittig adduct $Ph_3PCMe_2 \cdot GeH_2 \cdot BH_3$,[42, 43] laser photolysis of $Ge(CH_3)_4$ or GeH_4 gas,[44-46] photolysis of Ge wafer,[47] electroless deposition on preformed Ag nanocrystals,[48] Au-catalyzed vapor-liquid-solid growth using GeH_4[49] or diphenylgermane,[50] ultrasonic aerosol pyrolysis of tetrapropylgermane,[51] solution or solid phase reduction of NaGe,[52] plasma decomposition of $GeCl_4$[53-55] or GeH_4,[56] sulfur-assisted thermal decomposition of triphenylgermanium chloride,[57] and heating a solution of an alkylgermane in various high-temperature organic solvents.[58]

The preparation of Ge-Sn alloy nanocrystals typically follows one of the aforementioned strategies with the addition of a suitable Sn precursor, such as tin(II) chloride ($SnCl_2$) or bis(trimethylsilyl)amide $[Sn(HDMS)_2]$.[6, 59] A recent report showed the bottom-up formation of $Ge_{1-x}Sn_x$ nanowires grown from Sn nanocrystals.[60] The concentration of Sn in these nanowires was found to be 12.4 atom% ($x = 0.124$). $Ge_{1-x}Sn_x$ nanowires have also been formed from mixed Ge(II) and Sn(II) imido cubane precursors.[61] Spherical, Sn-rich Ge-Sn nanocrystals within a Ge matrix were prepared by annealing a Ge-Sn alloy layer cast between two thick layers of Ge.[62] Small aspect ratio Ge-Sn nanorod heterostructures have been prepared in one-pot through sequential additions of Sn and Ge precursors.[63] There are also several reports on Ge-Sn alloy thin films to study strained and relaxed phases.[7, 9, 64, 65]

Raman spectroscopy is very useful for the characterization of multiple component inorganic materials. It can be used to characterize amorphous *vs.* crystalline materials[58] and to determine strain within alloy systems.[6, 60, 61] Lin *et al.* independently found the contributions of alloy composition and strain to the shift in the Ge-Ge longitudinal optical

(LO) phonon in $Ge_{1-x}Sn_x$ films by tuning substrate topology.[9] They found a linear dependence between the Raman shift and film strain ($\Delta\omega = -(563 \pm 34)\varepsilon$ cm^{-1}) as well as Sn composition ($\Delta\omega = -(82 \pm 4)x$ cm^{-1}) where ε is the strain (in fractional form) and *x* is the Sn composition. Esteves *et al.* measured the Ge LO phonon mode by Raman spectroscopy for spherical $Ge_{1-x}Sn_x$ nanocrystals with increasing Sn content up to x = 0.279.[6] Increasing Sn content was associated with a lower Raman shift from ~294 to 287 cm^{-1}, which they attributed to combined alloy composition and lattice strain. Using Raman spectroscopy and scanning tunneling electron microscopy with energy dispersive X-ray spectroscopy (STEM-EDX), Seifner *et al.* correlated a shift in the LO phonon mode with varying Sn content for $Ge_{1-x}Sn_x$ nanorods.[61] A maximum shift in the LO phonon mode of -15 cm^{-1} was observed for nanorod sections where the mole fraction of Sn was at least 0.20. Similar behavior in $Ge_{1-x}Sn_x$ nanorods was observed by Biswas and coworkers.[50]

X-ray photoelectron spectroscopy (XPS) is another technique well suited to characterize Ge materials since they are prone to oxidation. XPS data for $Ge_{1-x}Sn_x$ nanocrystals synthesized by Ramasamy *et al.* showed typical peaks corresponding to Ge^0, Ge^{2+}, Ge^{4+}, Sn^0, and a broad, overlapping peak for Sn^{2+} and Sn^{4+}.[59] Relatively high ratios of the metallic peak to the oxidized peaks correlate to very little surface oxidation of these nanocrystals. Esteves and coworkers observed similar results, where three types of peaks were present: metallic Ge^0 and Sn^0 peaks from interior atoms, Ge^{2+} and $Sn^{2+/4+}$ peaks from atoms bound to passivating ligands, and a small Ge^{4+}peak from GeO_2 at the surface.[6] It has also been shown by XPS that treating Ge nanocrystals with dilute HCl removed a high percentage of a GeO_2 layer at the surface, with weakly bound Cl^- acting as a passivating ligand.[45] Indeed, all reports on the preparation of Ge nanocrystals where XPS was performed show strong peaks for Ge^0 and small contributions from oxidized species, whether they are attributed to surface ligands and/or surface oxidation (GeO_2).[19, 29, 66]

The photoluminescence (PL) properties of Ge-based materials are highly sensitive to the resultant size of the nanocrystals as well as other properties such as the capping ligand used.[3, 4, 18, 53, 67] Lee *et al.* prepared Ge nanocrystals stabilized with 1-octadecene that exhibited luminescence maxima from 900 to 1400 nm for diameters 3.2 to 4.0 nm.[18] Ruddy and coworkers demonstrated luminescent 2.3-4.7 nm nanocrystals capped with 1-octadecene prepared by co-reduction of GeI_2 and GeI_4 with size-dependent near-infrared PL from 860-1230 nm.[3] Guo *et al.* demonstrated 7 nm Ge/4.9CdS core/shell nanocrystals that exhibited a PL maximum at 950 nm.[4] Wheeler and coworkers showed 4.8-10.2 nm Ge nanocrystals capped with alkyl chains synthesized in the vapor phase that exhibit PL from 1200-1610 nm.[53] Recently, Robel and coworkers monitored the combined effect of temperature and high magnetic field on the PL lifetimes of Ge nanocrystals, which showed splitting between closely-spaced states as well as mixing between dark and bright states all contribute toward the indirect PL.[67] The intricacies of these widely varying optical properties are not clear: surface states very likely play a role for the luminescence in the visible region, as this extent of a blue shift from the bulk band gap is not explained by confinement alone.

Temperature-dependent PL studies have also been performed to examine the direct and indirect band gap contributions of $Ge_{1-x}Sn_x$ materials.[68, 69] The Arachchige group has demonstrated highly confined $Ge_{1-x}Sn_x$ nanocrystals showing PL in the 620 to 770 nm range, which closely follow calculations using *ab initio* HSE hybrid functional theory. They also used time-resolved PL at low (15 K) and ambient temperatures to further understand carrier dynamics.[70, 71] PL lifetimes at 15 K were found to be 3-27 μs, three orders of magnitude slower than at room temperature, owing to slow recombination of carriers in surface traps and spin-forbidden dark excitons. Temperature effects on the PL of very thin

$Ge_{1-x}Sn_x$ films have also been studied, showing a monotonic thermal PL quenching despite the indirect nature of the band gap.[72]

Reported herein are the comparative solution phase synthesis, characterization, and optical properties of $Ge_{1-x}Sn_x$ alloy nanocrystals *vs.* $Ge_{1-x}Sn_x$/CdS core/shell nanocrystals. All nanocrystalline samples were characterized by X-ray diffraction (XRD), transmission electron microscopy (TEM), Raman spectroscopy, X-ray photoelectron spectroscopy (XPS), and steady-state and time-resolved near infrared PL spectroscopy. The purpose of this work is to better understand the photophysical properties of Sn-doped Ge-based nanocrystals that may be useful for energy-related applications such as photovoltaics, light emitting devices (LEDs) or, with appropriate surface passivation,[73, 74] as near-infrared active luminescent biological markers.

Experimental

Materials. Cadmium oxide (CdO, 99.998%), sulfur (S_8, 99.999%) and oleic acid (90%) were purchased from Alfa Aesar; *n*-butyllithum (*n*-BuLi, 1.6 M hexane solution), bis[bis(trimethylsilyl)amido]tin(II) ($Sn(HMDS)_2$, ≥99.0%), oleylamine (OLA, ≥80-90.0%) and dioctylamine ($octyl_2NH$, 98%) were purchased from Sigma-Aldrich; hexadecylamine ($hexadecylNH_2$, 98%) and 1-octadecene (ODE, 90%) were purchased from Acros; and germanium(II) iodide (GeI_2, 99.99+%-Ge) was purchased from Strem. Procedures were performed under a dry inert gas atmosphere (N_2 or Ar) inside a glovebox or Schlenk line, unless specified otherwise.

Preparation of Ge and $Ge_{1-x}Sn_x$ (core) nanocrystals. Germanium cores were synthesized by a modified literature procedure.[4] Briefly, GeI_2 (0.049 g, 0.15 mmol) was added to an oven-dry, four-neck 250 mL round-bottom (R.B.) flask containing hexadecylamine (0.75 g, 3.1 mmol). The contents were degassed under vacuum at 80°C for 30 min, refilled with dry Ar, and heated to 200°C. A mixture of n-BuLi (0.2 mL of 1.6 M

hexane solution) and ODE (0.75 mL) was quickly injected while stirring. The temperature was raised from 200°C to 300°C, and the mixture further stirred for 1 h before cooling to room temperature (R.T., 21°C). The nanocrystals were purified by crashing three times with 10 mL of a 1:1 or 1:3 v/v acetone/methanol solution and centrifugation at 4500 rpm for 5 min, followed by redispersion in 5 mL of toluene.

$Ge_{1-x}Sn_x$ cores were prepared by a modified reported procedure.[59] Briefly, GeI_2 (0.049g, 0.15 mmol) and oleylamine (5 mL for $Ge_{0.95}Sn_{0.05}$; 10 mL for $Ge_{0.75}Sn_{0.25}$) with a varied amount of $Sn(HMDS)_2$ (0.018 g, 0.04 mmol for $Ge_{0.95}Sn_{0.05}$; 0.066 g, 0.15 mmol for $Ge_{0.75}Sn_{0.25}$) were added into a four-neck 250 mL round-bottom flask in a glovebox. The mixture was degassed under vacuum at 80 °C for 30 min, refilled with dry Ar, and heated to 230 °C for $Ge_{0.95}Sn_{0.05}$ or 250°C for $Ge_{0.75}Sn_{0.25}$. The mixture was annealed for 30 min for $Ge_{0.95}Sn_{0.05}$ cores or 5 min for $Ge_{0.75}Sn_{0.25}$ cores before cooling down to R.T.. It should be noted that the exact compositions of $Ge_{1-x}Sn_x$ nanocrystals varied somewhat from batch to batch; the low Sn inclusion preparation varied from 4-8% Sn, while the high Sn inclusion preparation varied from 23-28%. For simplicity, these are labeled as $Ge_{0.95}Sn_{0.05}$ and $Ge_{0.75}Sn_{0.25}$, respectively.

Preparation of Ge/CdS and $Ge_{1-x}Sn_x$/CdS (core/shell) nanocrystals. Ge/CdS or $Ge_{1-x}Sn_x$/CdS core/shell nanocrystals were prepared as follows: precursor solutions of Cd and S were prepared by a literature procedure.[4] 0.1 M $Cd(oleate)_2$ solution: CdO (318 mg, 2.48 mmol), oleic acid (3.09 g, 10.9 mmol), and ODE (7.11 g, 28.2 mmol) were degassed under vacuum at 80°C for 60 min, refilled with Ar, and heated to 240°C until optically clear. The mixture was allowed to cool down to R.T., and $(octyl)_2NH$ (12.5 mL, 41.4 mmol), previously degassed at 80°C for 30 min, injected into it. 0.1 M S_8 solution: S_8 (79.0 mg, 2.47 mmol) and ODE (19.7 g, 78.1 mmol) were degassed under a vacuum at 80°C for 30 min, refilled with Ar, and heated to 180°C for 20 min until optically clear.

To prepare core-shell nanocrystals *with excess precursors* (one-pot synthesis), a batch of freshly prepared $Ge_{1-x}Sn_x$ cores (in amine or amine/ODE) solution, ODE (1.5 mL, 4.7 mmol), and $(octyl)_2NH$ (1.5 mL, 5.0 mmol) were added to a four-neck 250 mL R.B. flask. The mixture was degassed at 80°C for 30 min, refilled with Ar, and heated to 230°C for Ge and $Ge_{0.95}Sn_{0.05}$ or 280°C for $Ge_{0.75}Sn_{0.25}$). Cd and S precursors were alternately injected using two programmable syringe pumps, each followed by a 15 min wait. The S precursor was injected first. 15 min after the last Cd injection, the mixture was allowed to cool to R.T.. Core-shell nanocrystals were washed as described above for $Ge_{1-x}Sn_x$ nanocrystals.

To prepare core-shell nanocrystals *without excess precursors*, the procedure above was repeated using nanocrystal cores where excess precursors have been removed following the purification method above. Toluene was removed under vacuum prior to shell growth.

Optical Characterization. Solution optical density (absorption plus scattering) spectra were measured with a photodiode array 8453 UV-visible spectrophotometer (Agilent, Santa Clara, CA). Steady-state photoluminescence (PL) spectra were measured using a Horiba-Jobin Yvon Nanolog scanning spectrofluorometer equipped with a liquid nitrogen-cooled InGaAs photodiode array. To account for sample concentration, PL intensities were divided by the optical density at the excitation wavelength of 350 nm. Photoluminescence lifetime measurements were performed using a previously described setup with a Nd:YAG laser (Continuum) and an avalanche photodiode.[75] The samples in toluene solution were excited at 532-nm with a pulse energy of 1 mJ/cm^2. The time-resolved photoluminescence was collected using an 800-nm long-pass filter and the decay trace was fit to a single or double exponential decay as needed.

Raman microspectroscopy was performed on nanocrystals using a 532-nm Sapphire SF laser (Coherent, Santa Clara, CA) illuminating a DM IRBE inverted light microscope (Leica Microsystems, Buffalo Grove, IL) fitted with a 100× oil (1.47 NA) objective. The nanocrystal solutions were drop cast onto glass slides and dried under ambient conditions. The scattered light was passed into a HoloSpec spectrometer (Kaiser Optical Systems, Ann Arbor, MI) equipped with a Newton 940 CCD camera (Andor Technology, Belfast, United Kingdom). The laser power density was 1.3×10^4 W/cm^2 with a laser spot size of 1 μm, and the acquisition time was 60 s. The data were plotted using IGOR (WaveMetrics, Portland, OR).

Infrared spectroscopy was performed on a Bruker Vertex 80 FT-IR spectrometer equipped with a MIR_IR_XPM detector with 16 scans at a resolution of 4 cm^{-1}. The samples were prepared as drop cast thin films on NaCl salt plates. Background spectra were collected under identical conditions, and samples were continuously purged with dry N_2 to minimize water vapor absorbance.

Structural Characterization. Powder X-ray diffraction (XRD) was measured using Cu Kα radiation on a Rigaku Ultima diffractometer. X-ray photoelectron spectroscopy (XPS) measurements were performed using a Kratos Amicus/ESCA 3400 instrument. The sample was irradiated with 240 W non-monochromated Mg Kα x-rays, and photoelectrons emitted at 0 ° from the surface were analyzed using a DuPont-type analyzer. The pass energy was set at 75 eV. CasaXPS was used to process raw data files. The binding energy of C 1s at 284.6 eV was used as a reference. Depth profiling was performed using monoatomic Ar ion sputtering for 8 s, followed by XPS acquisition. The acceleration voltage used was 500 V in order to minimize ion-induced reduction. Sample rotation during sputtering was used to achieve uniform etching. Transmission Electron Microscopy (TEM) was conducted using a FEI Tecnai G2 F20 field emission TEM operating at up to 200 kV.

Samples were prepared by placing 1 or 2 drops of concentrated toluene solutions onto carbon-coated copper grids. Elemental composition was characterized by energy-dispersive spectroscopy (EDX). Nanocrystal dimensions were measured with ImageJ. The longest dimension was measured and reported. At least 300 nanocrystals were counted in each case. Uncertainties in all measurements are reported as standard deviations.

Results and Discussion

Synthesis and Characterization of $Ge_{1-x}Sn_x$ Core Nanocrystals. Ge, $Ge_{0.95}Sn_{0.05}$, and $Ge_{0.75}Sn_{0.25}$ nanocrystals were prepared and characterized by powder X-ray diffraction (XRD). Patterns of $Ge_{1-x}Sn_x$ nanocrystals shown in **Figure 1** confirm the crystalline products are homogeneous nanoalloys of Ge and α-Sn in the cubic diamond phase with $Fd\bar{3}m$ space group. The composition of Sn incorporated in the cubic Ge lattice was calculated based on Vegard's Law: $a_{(Ge_{1-x}Sn_x)} = a_{(Sn)}(x) + a_{(Ge)}(1-x)$. Here, a is the lattice parameter of the sample or standard and x is the composition of Sn in the nanocrystal. Structural parameters of the Ge and $Ge_{1-x}Sn_x$ nanocrystals, as well as CdS, are shown in **Table 1** and **Figure 2**. The shift in the diffraction peak to lower 2θ angles indicates a lattice expansion from 5.658 Å (Ge) to 5.706 Å ($Ge_{0.95}Sn_{0.05}$) and 5.870 Å ($Ge_{0.75}Sn_{0.25}$). To ensure the measured peak shift was not due to any measurement variables, such as the sample height in the XRD instrument, Si powder was used as an internal standard to align the experimental pattern for all samples. As is often the case in low temperature, solution-synthesized nanocrystals,[5] the molar ratios of Ge:Sn used in the synthetic preparations were not conserved in the nanocrystal. For instance, the $Ge_{0.75}Sn_{0.25}$ sample was prepared from a 1:1 molar ratio of Ge:Sn. This could be explained, in part, by the comparatively large cationic radius of Sn^{2+} compared to Ge^{2+}, which contributes to Sn having a relatively low solubility in bulk Ge of about ~1%.[76] However, Sn incorporation as

high as 42% has been reported in $Ge_{1-x}Sn_x$ nanocrystal alloys,[59] likely because solution phase nanocrystal syntheses are often kinetically and not thermodynamically controlled.

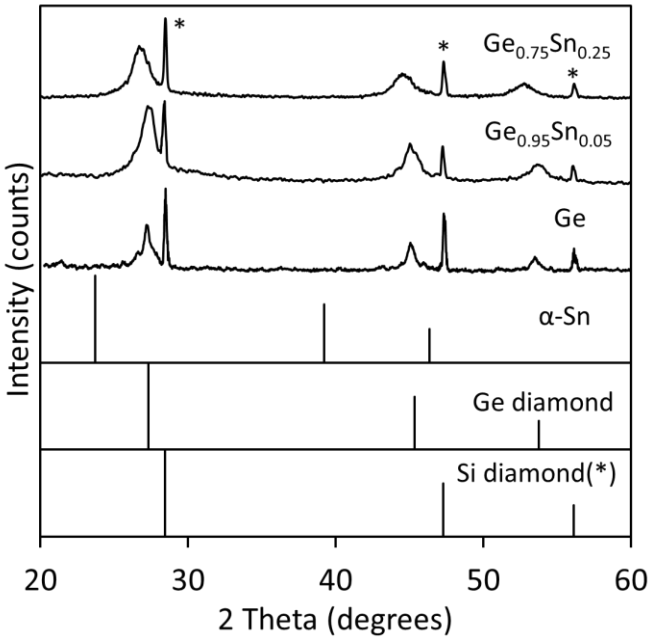

Figure 1. Experimental powder X-ray diffraction (XRD) patterns of Ge and $Ge_{1-x}Sn_x$ alloy nanocrystals. The standard powder XRD patterns of bulk Ge, α-Sn, and Si diamond (* = used as an internal standard) are shown for comparison.

Table 1. Structural parameters of Ge and $Ge_{1-x}Sn_x$ nanocrystals.

Material	Crystal structure	Lattice parameter (Å)	Lattice mismatch[a]
CdS	zinc blende	5.832	0
Ge	diamond	5.658	+3.0%
$Ge_{0.95}Sn_{0.05}$	diamond	5.706	+2.2%
$Ge_{0.75}Sn_{0.25}$	diamond	5.870	-0.65%

[a] $\Delta a = 100 \times (a_{shell} - a_{core})/(a_{core})$; signs refer to shell-induced core expansion (+) or compression (-).

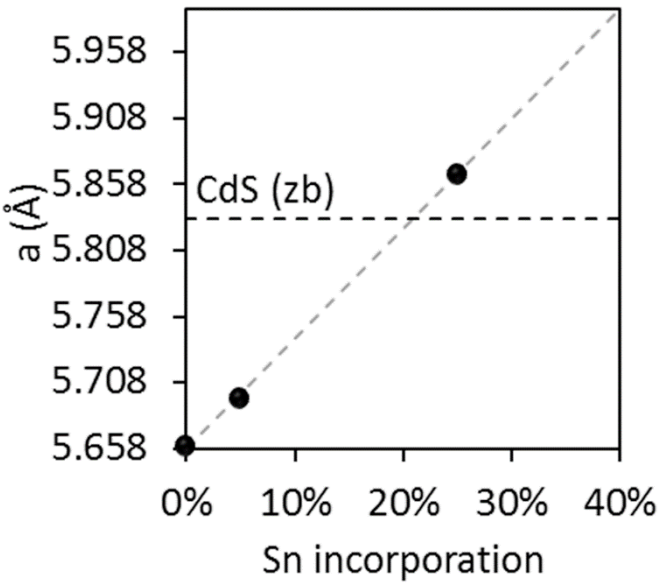

Figure 2. Lattice parameter of $Ge_{1-x}Sn_x$ nanocrystals as a function of Sn incorporation. $Ge_{0.75}Sn_{0.25}$ nanocrystals have the smallest lattice mismatch with the cubic CdS (5.832, horizontal dashed line), compared to Ge or $Ge_{0.95}Sn_{0.05}$. The dashed gray line is a linear regression to the data.

To accurately characterize the morphology and size of the nanocrystals, TEM images were collected (**Figure 3**). Size histograms for each sample are shown in **Figure S1**. Overall, the samples are well dispersed spheroidal nanocrystals with crystal sizes of 6 ± 1 nm (Ge), 6 ± 1 nm ($Ge_{0.95}Sn_{0.05}$), and 11 ± 2 nm ($Ge_{0.75}Sn_{0.25}$). Adding more Sn precursor always leads to larger core particles. In an effort to make $Ge_{1-x}Sn_x$ cores comparable in size to Ge cores, we lowered the precursor solution concentration and shortened the reaction time. However, while this approach works well for $Ge_{0.95}Sn_{0.05}$ with a particle size of 6 ± 1 nm, the smallest $Ge_{0.75}Sn_{0.25}$ we could synthesize still has a relatively large particle size of 11 ± 2 nm. In addition to TEM, energy dispersive spectrometry (EDX) was performed to assess the particle composition and homogeneity (**Table 2**). EDX data of $Ge_{1-x}Sn_x$ nanocrystals shows good agreement with the theoretical elemental composition calculated by Vegard's Law.

Table 2. TEM-EDX analysis of Ge, $Ge_{1-x}Sn_x$ and $Ge_{1-x}Sn_x$/CdS nanocrystals.			
Sample	Size (nm)	Composition: Ge, Sn, Cd, S	
		Theoretical (%)[a]	EDX (%)
Ge	6 ± 1	100, 0, 0, 0	100, 0, 0, 0
$Ge_{0.95}Sn_{0.05}$	6 ± 1	95, 5, 0, 0	90 ± 1, 10 ± 1, 0, 0
$Ge_{0.75}Sn_{0.25}$	11 ± 2	75, 25, 0, 0	78 ± 3, 22 ± 3, 0, 0
Ge/3.4CdS	8 ± 2	19, 0, 41, 41	7 ± 1, 0, 49 ± 1, 44 ± 1
$Ge_{0.95}Sn_{0.05}$/3.4CdS	8 ± 2	29, 2, 35, 35	67 ± 9, 8 ± 7, 18 ± 8, 7 ± 3
$Ge_{0.75}Sn_{0.25}$/3.4CdS	13 ± 2	28, 9, 31, 31	58 ± 3, 4 ± 2, 16 ± 2, 22 ± 1
[a]Based on a 100% Ge_xSn_{1-x}/CdS composition.			

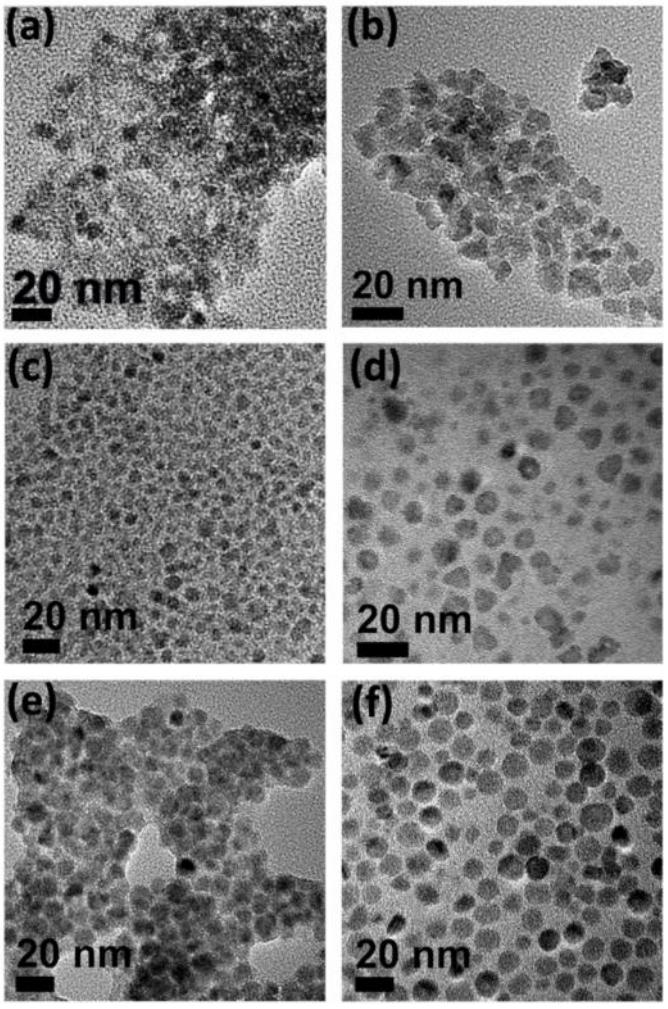

Figure 3. $Ge_{1-x}Sn_x$ core and $Ge_{1-x}Sn_x$ /CdS core/shell nanocrystals: (a) Ge (6 ± 1 nm), (b) Ge/CdS (8 ± 2 nm), (c) $Ge_{0.95}Sn_{0.05}$ (6 ± 1 nm), (d) $Ge_{0.95}Sn_{0.05}$/CdS (8 ± 2 nm), (e) $Ge_{0.75}Sn_{0.25}$ (11 ± 2 nm), (f) $Ge_{0.75}Sn_{0.25}$/CdS (13 ± 2 nm). The average size measured from more than 300 nanocrystals is provided in parentheses.

Raman spectra for the Ge-Ge LO phonon mode of pure Ge and $Ge_{1-x}Sn_x$ alloy nanocrystals are shown in **Figure 4a**. As the Sn content is increased, the Ge LO phonon mode is shifted by -1.2 cm^{-1} ($Ge_{0.95}Sn_{0.05}$) and -4.4 cm^{-1} ($Ge_{0.75}Sn_{0.25}$). For the $Ge_{1-x}Sn_x$ alloy system, two additive factors determine the observed peak shift in the Ge-Ge LO phonon: the compositional (pure mass) effect and lattice strain. Deconvoluting the compositional effect and strain has been performed on films, where substrate conditions allow for tuning the strain.[9, 64, 65, 77, 78] For small nanocrystals it is likely that the compositional effect dominates since strain within the alloy can be dissipated due to a high surface area.[50] The smaller Raman shifts are thus primarily attributed to the larger Sn atoms expanding the crystal lattice as shown by XRD; longer (weaker) bonds are associated with a shift to lower energies. A plot of the Sn compositional dependence of the Ge-Ge LO phonon is shown in **Figure 4b**. For two batches of $Ge_{1-x}Sn_x$ nanocrystals prepared in the same way the best-fit line produced different slopes despite similar compositions being measured by XRD: $\Delta\omega(x) = -(17 \pm 1)x$ and $\Delta\omega(x) = -(42 \pm 5)x$ where x is the Sn composition. At present, it is unclear why the two sets of experiments showed different compositional dependence, and why these values are different than those reported for nanorods[50] and strain-free films[65]—further experiments are underway to investigate this. The line traces shown in **Figure 4a** are two-peak Gaussian fits to the experimental spectra to account for asymmetry at lower Raman shifts. Asymmetry in the phonon peaks of small nanocrystals is attributed to contributions from surface optical (SO) phonons, which are typically slightly lower in energy than the corresponding LO phonons.[79, 80] SO phonons are more prominent for anisotropic crystals.[81] The Sn-Ge LO phonon was not observed in the Raman spectrum of the nanoalloy, which is consistent with previous work on thin films.[65] A Raman spectrum of GeO_2 was also acquired to investigate the possibility of interference from surface oxidation (**Figure S2**), but no GeO_2 bands are observed in the 280 to 320 cm^{-}

[1] Ge-Ge LO phonon range, which is consistent with the literature.[82] Likewise, no additional bands that correlate to GeO_2 were observed outside this spectral range for the Ge and $Ge_{1-x}Sn_x$ nanocrystal samples.

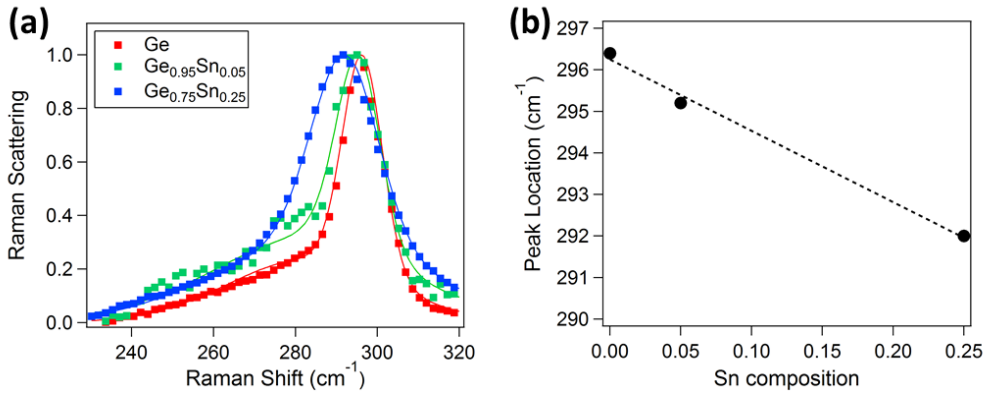

Figure 4. (a) Normalized Raman spectra for Ge and $Ge_{1-x}Sn_x$ alloy nanocrystals and (b) Sn compositional dependence of Ge-Ge LO phonon peak position. As the Sn content increases, the Ge LO phonon peak is shifted to lower wavenumbers and the FWHM increases. Spectra were fit to 2-peak Gaussian curves (solid lines) to account for asymmetry. Average Raman peak properties are listed in Table S1.

Synthesis and Characterization of $Ge_{1-x}Sn_x$/CdS Core/Shell Nanocrystals. Freshly synthesized $Ge_{1-x}Sn_x$ cores were reacted with Cd and S precursors alternately to form CdS shells using the successive ion layer adsorption and reaction (SILAR) method.[4, 83] Two preparation methods were employed: one using the synthetic mixture of the $Ge_{1-x}Sn_x$ cores without removing the residual precursors (one-pot synthesis), referred to as the crude $Ge_{1-x}Sn_x$ sample, and the second using cores re-suspended in toluene after purification *via* centrifugation, referred to as the purified $Ge_{1-x}Sn_x$ sample. The XRD patterns and Raman spectra of the crude $Ge_{1-x}Sn_x$ samples showed unwanted SnS (**Figure S3**). Because the core/shell synthesis using crude core solutions did not generate monodisperse core/shell nanocrystals, all core/shell samples discussed in the remaining text were prepared using purified cores. **Figure 5** shows XRD patterns of the core/shell nanocrystals. The Ge/CdS

sample showed mainly hexagonal wurtzite structure. Ge/CdS nanocrystals with a predominately wurtzite structure have been reported previously for a preparation using crude core solution.[4] Polytypism in group IV and II-VI nanocrystals, as well as in their epitaxial (core/shell, etc.) systems is relatively common, and can be size-dependent.[84-86]

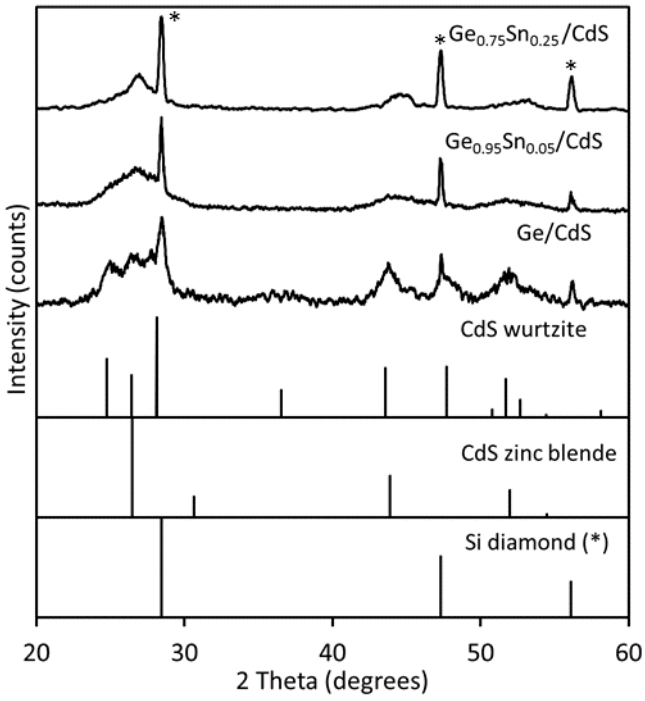

Figure 5. Experimental powder X-ray diffraction (XRD) patterns of Ge/CdS and $Ge_{1-x}Sn_x$/CdS core/shell nanocrystals. The standard powder XRD patterns of bulk CdS zinc blende (cubic), CdS wurtzite (hexagonal), and Si diamond (* = used as an internal standard) are shown for comparison.

To make the core/shell nanocrystals with different Sn incorporations comparable, we grew CdS shells with similar thicknesses. TEM images in **Figure 3** show, in all cases, the core/shell nanocrystals increase 2 nm in diameter compared to their uncoated or bare cores. When compared to the known lattice parameter of CdS (either wurtzite or zinc blende give similar results), this shell thickness corresponds to the growth of 3.4 monolayers of CdS on the $Ge_{1-x}Sn_x$ cores. Area EDX scans containing several $Ge_{1-x}Sn_x$ cores agree with

their theoretical elemental composition; albeit the Ge content in $Ge_{1-x}Sn_x$ /CdS core/shells appears to be larger than the theoretical value. EDX elemental mapping of individual particles show that a majority of $Ge_{1-x}Sn_x$ cores are coated with CdS (**Figure S4**). Many of these core/shell particles have a relatively inhomogeneous shell, which is consistent with well documented studies on CdSe/CdS core/shell nanocrystals.[73, 74, 87-89]

As in the classical CdSe/CdS system, inhomogeneous surface coverage in $Ge_{1-x}Sn_x$ /CdS core/shell nanocrystals is not an immediate problem, at least in terms of ensemble optical properties, as it is able to provide enough surface passivation to enhance and stabilize PL compared to the bare $Ge_{1-x}Sn_x$ cores. High resolution high-angle annular dark-field (HAADF) STEM images of a $Ge_{0.75}Sn_{0.25}$/CdS nanocrystals (**Figure S5**) show the presence of continuous lattice fringes throughout each particle.

Raman spectra for the $Ge_{1-x}Sn_x$/CdS core/shell nanocrystals are shown in **Figure S6**. The Raman shift of the Ge-Ge LO phonon mode for the Ge/CdS nanocrystals is shifted by a statistically significant +1.1 cm^{-1} relative to the nanocrystals without a shell. This implies the shell generates compressive strain on the core, due to the smaller lattice parameter of CdS wurtzite compared to Ge (Ge = 5.658 Å, CdS wurtzite a = 4.135 Å). If CdS (with a peak maximum at 300 cm^{-1}) spectrally interfered with the Ge LO optical phonon mode (with a peak maximum <296 cm^{-1} in the core material), we would expect the peak FWHM to increase. We conclude that CdS does not spectrally interfere in our data, as the peak FWHM is the same or slightly decreased for the core/shell nanocrystals. In addition, no peaks were measured for pure CdS nanocrystals measured under similar acquisition parameters as those used to collect the data in **Figure S6**. For the $Ge_{1-x}Sn_x$ core/shell samples, the shifts in the LO phonon mode upon shell addition are insignificant (**Table S1**). The lattice parameter for CdS zinc blende (5.82 Å) is closer to the lattice parameter of the alloy core materials (**Table 1**), particularly $Ge_{0.75}Sn_{0.25}$, which is consistent

with minimal compressive strain and a negligible phonon mode shift. The smaller lattice mismatch between the $Ge_{1-x}Sn_x$ core nanocrystals and the CdS shell facilitates epitaxial growth of the latter.

X-Ray Photoelectron Spectroscopy of Ge/CdS and $Ge_{1-x}Sn_x$/CdS Core/Shell Nanocrystals. XPS survey spectra of all core/shell nanocrystal samples are shown in the supporting information (**Figure S7**). XPS depth profiling was performed to reveal the sub-surface information of the Ge/CdS core/shell nanocrystals and to corroborate the formation of a core/shell structure (**Figure 6**). We analyzed the chemical states of Ge, Cd, and S. There is no Ge signal above the noise in the initial etching cycles. After a few etching cycles, emerging peaks at ~29.5 eV in the Ge 3d energy region and ~1217 and 1250 eV in the Ge 2p energy region that correspond to metallic Ge^0 were measured, along with a shoulder peak at ~32-33 eV corresponding to $Ge^{2+/4+}$ (**Figure 6a**). These data are consistent with the chemical state of purified Ge core without any shell growth (Ge^0), which exhibits a peak at ~29.5 eV, and mild surface oxidation ($Ge^{2+/4+}$). Furthermore, the core/shell nanocrystals exhibited peaks throughout the etching at ~405 and ~412 eV corresponding to Cd, and a peak at ~162 eV, which corresponds to S^{2-} (**Figure 6c-d**). This substructure information provides confirmation for the chemical speciation of the core/shell structure of Ge/CdS nanocrystals.

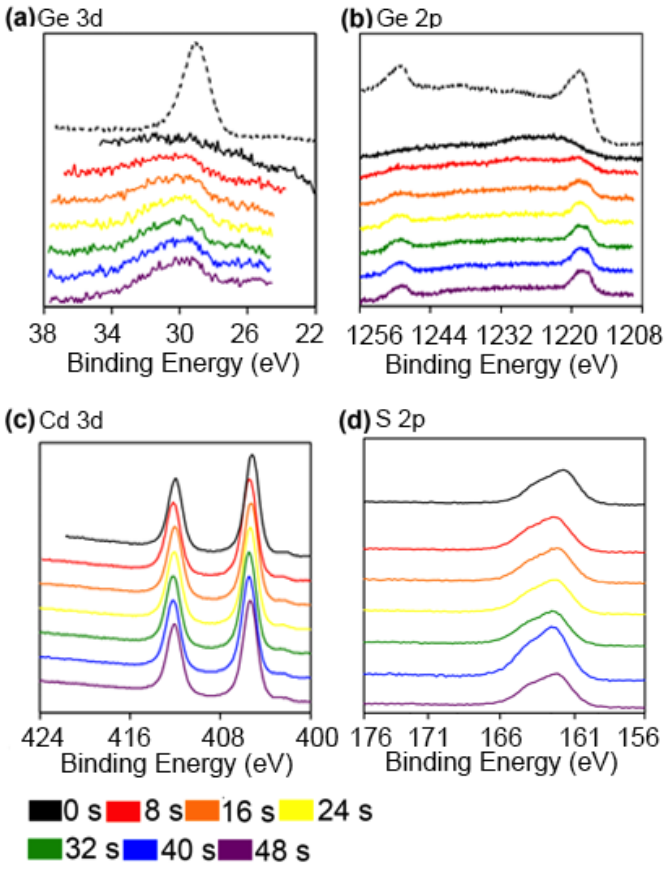

Figure 6. XPS depth profiles of Ge/CdS core/shell nanocrystals. Depth profiling uses an ion beam to etch the layers of the sample revealing sub-surface information; each etching cycle is 8 s and total etching time is indicated by the color of the spectra. Ge nanocrystals with no shell are shown as dashed lines in (a) and (b) for reference, and all the spectra are calibrated to adventitious carbon at 284.6 eV.

We similarly analyzed the chemical states of Ge, Sn, Cd, and S in the purified $Ge_{1-x}Sn_x$ and $Ge_{1-x}Sn_x$/CdS core/shell nanocrystals (**Figure 7**). XPS confirms the element distribution in alloy nanocrystals. The Ge 3d peak at ~29.5 eV and a shoulder around ~32-33 eV corresponds to Ge^0 and $Ge^{2+/4+}$ species, respectively. The peak at ~486 eV corresponds to Sn^{4+} species (SnO_2). Ge and Sn in higher oxidation states indicate post-synthetic surface oxidation. The core/shell

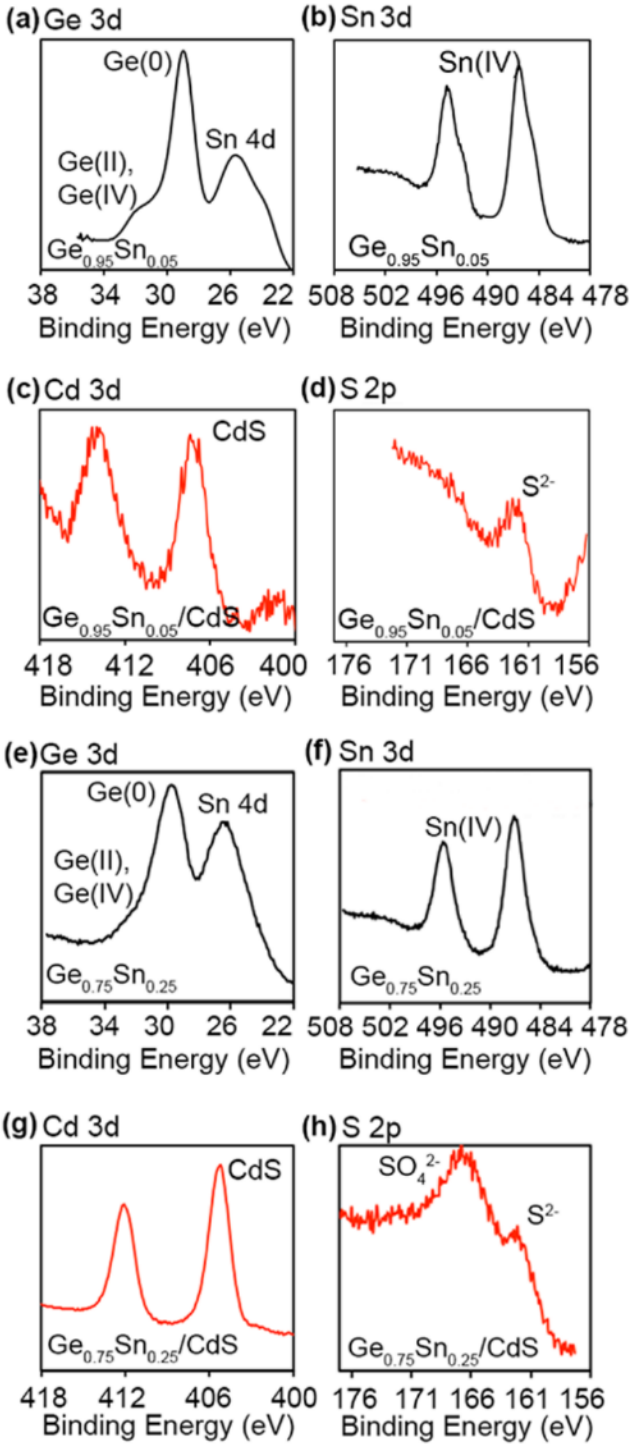

Figure 7. X-ray photoelectron spectra (XPS) of (a-b) $Ge_{0.95}Sn_{0.05}$, (c-d) $Ge_{0.95}Sn_{0.05}$/CdS, (e-f) $Ge_{0.75}Sn_{0.25}$, and (g-h) $Ge_{0.75}Sn_{0.25}$/CdS nanocrystals. All the spectra are calibrated to adventitious carbon at 284.6 eV.

Luminescence Properties of $Ge_{1-x}Sn_x$ Core and $Ge_{1-x}Sn_x$/CdS Core/Shell Nanocrystals. The solution phase optical density spectra of Ge and $Ge_{1-x}Sn_x$ nanoscrystals

show no prominent absorption features (**Figure 8**), which could be due to the small bandgap (0.66 eV, 1876 nm for bulk Ge, **Figure S8**) being out of our instrument range. The $Ge_{1-x}Sn_x$/CdS core/shell nanocrystals have absorption onsets at 450-500 nm, which is consistent with the bandgap of quantum confined CdS shells (**Figure S8**).[90]

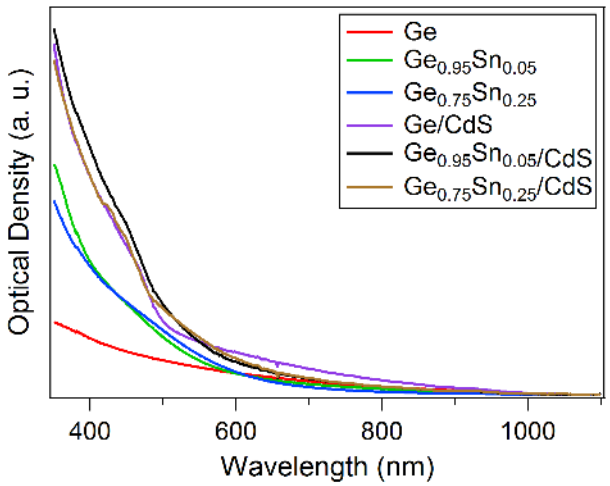

Figure 8. Solution phase optical density (absorption and scattering) spectra of Ge, $Ge_{1-x}Sn_x$, Ge/CdS and $Ge_{1-x}Sn_x$/CdS nanocrystals suspended in toluene.

Photoluminescence spectra of the nanocrystals corrected for optical density at the excitation wavelength of 350 nm are shown in **Figure 9**. For the nanocrystals without shells, the signals from all samples were too low to confidently discriminate them from the instrument's background. This means there is no detectable PL from any of the core-only nanocrystals. Sn inclusion in the alloy nanocrystals is thus not associated with an increase in luminescence intensity. Assuming the doped and undoped samples had similar surface defects and surface oxidation, there is no indication that a more direct band gap character was achieved in the Sn-doped nanocrystals, as an enhanced PL response was not measured. On the other hand, all the core/shell nanocrystals display an enhanced near infrared PL compared to the $Ge_{1-x}Sn_x$ and Ge nanocrystals without shells. With a bulk band gap of 0.66 eV (**Figure S8**), the PL spectra indicate these core/shells are also quantum confined. The

PL enhancements of $Ge_{0.75}Sn_{0.25}$/CdS and $Ge_{0.95}Sn_{0.05}$/CdS were 15× and 12× greater than Ge/CdS, respectively. The luminescence intensity decreases when oxidation is measured by the presence of a Ge-O band in the FT-IR spectrum. $Ge_{0.75}Sn_{0.25}$/CdS core/shells where no oxidation was present show the highest PL intensity. In another set of experiments where oxidation was measured by FT-IR spectroscopy (for example **Figure S9** shows an example of oxidation in the $Ge_{0.75}Sn_{0.25}$ sample), the oxidized core/shells exhibited 100× lower luminescence than the non-oxidized $Ge_{0.75}Sn_{0.25}$/CdS sample (**Figure 9**). The observed PL enhancement is most likely due to more effective surface passivation by the CdS shell on the $Ge_{1-x}Sn_x$ cores, because Sn inclusion in the core without the shell did not result in a higher PL response (see above), whereas oxidation reduces luminescence. Considering the lattice parameters of the core and shell, doping the core with Sn leads to improved epitaxy (smaller lattice mismatch with the shell). This may produce improved crystal growth for core/shell nanocrystals with fewer defects within the crystals that can quench photoluminescence.

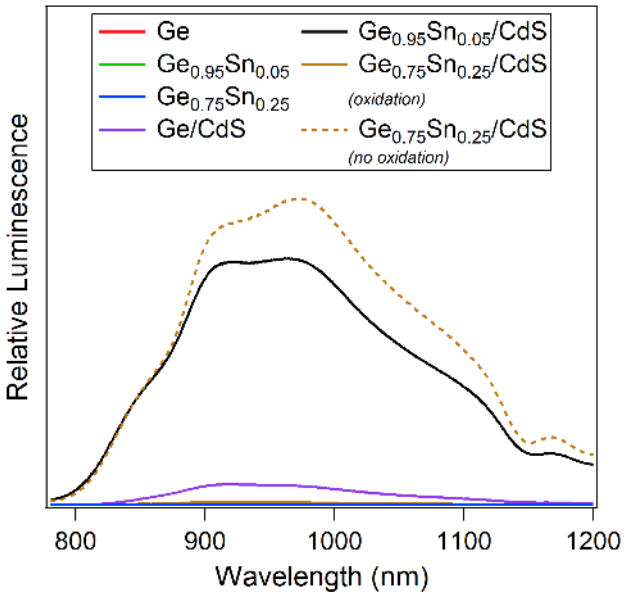

Figure 9. Relative near infrared photoluminescence (PL) spectra of the Ge and $Ge_{1-x}Sn_x$ cores and requisite core/shell nanocrystals. The intensity is normalized by the optical

density at the excitation wavelength, λ_{exc} = 350 nm. The Ge, $Ge_{0.95}Sn_{0.05}$, $Ge_{0.75}Sn_{0.25}$, and oxidized $Ge_{0.75}Sn_{0.25}$/CdS samples overlap on this scale.

Excited-state lifetime measurements for the core/shell nanocrystals are shown in **Figure 10**. These measurements were performed on only the core/shell nanocrystals because the PL intensity of the core-only particles was too low to measure the lifetimes. The Ge/CdS nanocrystals yielded a lifetime of 4.1 µs, which is similar to the previous finding of Guo *et al*.[4] Upon incorporation of Sn in the Ge core, the PL lifetimes decreased to 2.8 and 1.0 µs for $Ge_{0.95}Sn_{0.05}$/CdS and $Ge_{0.75}Sn_{0.25}$/CdS, respectively. The observed decrease in PL lifetime along with higher steady state PL intensity in the core/shell nanocrystals could be indicative of a more direct band gap. However, there may be no correlation between the steady state PL intensity and the lifetimes of these materials. In order to correlate these two measurements, one would have to show the emitting states are the same for all types of nanocrystals; however, and unlike the case of coating cores of the exact same material but having different sizes, there is no reason to assume this is the case for our series because they are based on chemically distinct cores (materials with different doping levels).

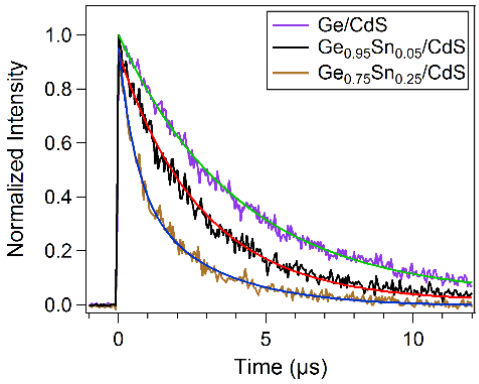

Figure 10. Time-resolved photoluminescence traces of Ge/CdS, $Ge_{0.95}Sn_{0.05}$/CdS, and $Ge_{0.75}Sn_{0.25}$/CdS core/shell nanocrystals. The decays of Ge/CdS and $Ge_{0.95}Sn_{0.05}$/CdS are

single-exponential with lifetimes of 4.1 μs and 2.8 μs, respectively, while a double-exponential was used for $Ge_{0.75}Sn_{0.25}$/CdS, yielding an average lifetime of 1.0 μs.

Conclusion

$Ge_{1-x}Sn_x$ alloy nanocrystals and $Ge_{1-x}Sn_x$ core/shell nanocrystals were prepared *via* solution-based synthesis and characterized by XRD, TEM, Raman, optical, and X-ray photoelectron spectroscopy. Incorporation of Sn did not increase the PL intensity in the cores, but core/shell nanocrystals prepared using the Sn-doped cores and CdS shell show up to 15× enhanced PL when compared to Ge/CdS materials. This is explained by improved epitaxy between the lattice-expanded Sn-doped Ge cores and the structurally similar CdS shell, along with reduced surface oxidation. The combination of scalability and improved PL intensities make these $Ge_{1-x}Sn_x$ core/shell nanocrystals promising alternatives to other near infrared-active materials for use as functional materials in solar cells and LEDs. In addition, these nanocrystals have potential as anode materials in advanced lithium ion batteries, and when combined with available biocompatibility steps (ligand exchange and surface-protection or encapsulation), as near-infrared luminescent markers in biological studies.

Acknowledgements

This research is supported by the U.S. Department of Energy, Office of Basic Energy Sciences, Division of Chemical Sciences, Geosciences, and Biosciences through the Ames Laboratory. Electron microscopy characterization was performed at Ames Laboratory's Sensitive Instrument Facility. Ames Laboratory is operated for the U.S. Department of Energy by Iowa State University under contract # DE-AC02-07CH11358. The authors thank Duane Johnson and Gordie Miller for comments. XPS work was performed at the Materials Analysis and Research Laboratory of the Iowa State University Office of Biotechnology. We thank Dapeng Jing for XPS measurements and discussions.

References

1. Vaughn, D. D., II; Schaak, R. E., Synthesis, Properties and Applications of Colloidal Germanium and Germanium-Based Nanomaterial. *Chem. Soc. Rev.* **2013,** 42, 2861–2879.

2. Xu, C.; Gallagher, J. D.; Senaratne, C. L.; Menéndez, J.; Kouvetakis, J., Optical Properties of Ge-Rich $Ge_{1-x}Si_x$ Alloys: Compositional Dependence of the Lowest Direct and Indirect Gaps. *Phys. Rev. B* **2016,** 93, 125207-1–125207-16.

3. Ruddy, D. A.; Johnson, J. C.; Smith, E. R.; Neale, N. R., Size and Bandgap Control in the Solution-Phase Synthesis of Near-Infrared-Emitting Germanium Nanocrystals. *ACS Nano* **2010,** 4, 7459–7466.

4. Guo, Y.; Rowland, C. E.; Schaller, R. D.; Vela, J., Near-Infrared Photoluminescence Enhancement in Ge/CdS and Ge/ZnS Core/Shell Nanocrystals: Utilizing IV/II-VI Semiconductor Epitaxy. *ACS Nano* **2014,** 8, 8334–8343.

5. Men, L.; White, M. A.; Andaraarachchi, H. A.; Rosales, B. A.; Vela, J., Synthetic Development of Low Dimensional Materials. *Chem. Mater.* **2017,** 29, 168–175.

6. Esteves, R. J. A.; Ho, M. Q.; Arachchige, I. U., Nanocrystalline Group IV Alloy Semiconductors: Synthesis and Characterization of $Ge_{1-x}Sn_x$ Quantum Dots for Tunable Bandgaps. *Chem. Mater.* **2015,** 27, 1559–1568.

7. Cheng, R.; Wang, W.; Gong, X.; Sun, L.; Guo, P.; Hu, H.; Shen, Z.; Han, G.; Yeo, Y.-C., Relaxed and Strained Patterned Germanium-Tin Structures: A Raman Scattering Study. *J. Solid State Sci.* **2013,** 2, 138–145.

8. Gupta, S.; Magyari-Köpe, B.; Nishi, Y.; Saraswat, K. C., Achieving Direct Band Gap in Germanium Through Integration of Sn Alloying and External Strain. *J. Appl. Phys.* **2013,** 113, 073707-1–073707-7.

9. Lin, H.; Chen, R.; Huo, Y.; Kamins, T. I.; Harris, J. S., Raman Study of Strained $Ge_{1-x}Sn_x$ Alloys. *Appl. Phys. Lett.* **2011,** 98, 261917-1–261917-3.

10. Gallagher, J. D.; Senaratne, C. L.; Kouvetakis, J.; Menendez, J., Compositional Dependence of the Bowing Parameter for the Direct and Indirect Band Gaps in $Ge_{1-y}Sn_y$ Alloys. *Appl. Phys. Lett.* **2014,** 105, 142102-1–142102-5.

11. Senaratne, C. L.; Gallagher, J. D.; Xu, C.; Sims, P.; Menendez, J.; Kouvetakis, J., Doping of Direct Gap $Ge_{1-y}Sn_y$ Alloys to Attain Electroluminescence and Enhanced Photoluminescence. *ECS Trans.* **2015,** 69, 157–164.

12. Stange, D.; Wirths, S.; Von Den Driesch, N.; Mussler, G.; Stoica, T.; Ikonic, Z.; Hartmann, J.; Mantl, S.; Grützmacher, D.; Buca, D., Optical Transitions in Direct-Bandgap $Ge_{1-x}Sn_x$ Alloys. *ACS Photonics* **2015,** 2, 1539–1545.

13. Carolan, D.; Doyle, H., Efficient One-Pot Synthesis of Monodisperse Alkyl-Terminated Colloidal Germanium Nanocrystals. *J. Nanopart. Res.* **2014,** 16, 2721.

14. Carolan, D.; Doyle, H., Size Controlled Synthesis of Germanium Nanocrystals: Effect of Ge Precursor and Hydride Reducing Agent. *Journal of Nanomater.* **2015,** 2015, 156-1–156-9.

15. Chou, N. H.; Oyler, K. D.; Motl, N. E.; Schaak, R. E., Colloidal Synthesis of Germanium Nanocrystals Using Room-Temperature Benchtop Chemistry. *Chem. Mater.* **2009,** 21, 4105–4107.

16. Codoluto, S. C.; Baumgardner, W. J.; Hanrath, T., Fundamental Aspects of Nucleation and Growth in the Solution-Phase Synthesis of Germanium Nanocrystals. *CrystEngComm* **2010,** 12, 2903–2909.

17. Karatutlu, A.; Song, M.; Wheeler, A. P.; Ersoy, O.; Little, W. R.; Zhang, Y.; Puech, P.; Boi, F. S.; Luklinska, Z.; Sapelkin, A. V., Synthesis and Structure of Free-Standing

Germanium Quantum Dots and Their Application in Live Cell Imaging. *RSC Adv.* **2015,** 5, 20566–20573.

18. Lee, D. C.; Pietryga, J. M.; Robel, I.; Werder, D. J.; Schaller, R. D.; Klimov, V. I., Colloidal Synthesis of Infrared-Emitting Germanium Nanocrystals. *J. Am. Chem. Soc.* **2009,** 131, 3436–3437.

19. Lu, X. M.; Korgel, B. A.; Johnston, K. P., High Yield of Germanium Nanocrystals Synthesized from Germanium Diiodide in Solution. *Chem. Mater.* **2005,** 17, 6479–6485.

20. Zhang, Y.; Ersoy, O.; Karatutlu, A.; Little, W.; Sapelkin, A., Local Structure of Ge Quantum Dots Determined by Combined Numerical Analysis of EXAFS and XANES Data. *J. Synchrotron Radiat.* **2016,** 23, 253–259.

21. Prabakar, S.; Shiohara, A.; Hanada, S.; Fujioka, K.; Yamamoto, K.; Tilley, R. D., Size Controlled Synthesis of Germanium Nanocrystals by Hydride Reducing Agents and Their Biological Applications. *Chem. Mater.* **2010,** 22, 482–486.

22. Warner, J. H.; Tilley, R. D., Synthesis of Water-Soluble Photoluminescent Germanium Nanocrystals. *Nanotechnology* **2006,** 17, 3745–3749.

23. Cosentino, S.; Torrisi, G.; Raciti, R.; Zimbone, M.; Crupi, I.; Mirabella, S.; Terrasi, A., Growth Kinetics of Colloidal Ge Nanocrystals for Light Harvesters. *RSC Adv.* **2016,** 6, 38454–38462.

24. Ghosh, B.; Ogawara, M.; Sakka, Y.; Shirahata, N., Reductant-Free Colloidal Synthesis of Near-IR Emitting Germanium Nanocrystals: Role of Primary Amine. *J. Nanosci. Nanotechnol.* **2014,** 14, 2204–2210.

25. Shirahata, N., Solution-Processable White-Light-Emitting Germanium Nanocrystals. *J. Solid State Chem.* **2014,** 214, 74–78.

26. Holmes, A. L.; Hutges, J.; Reckmann, A.; Muthuswamy, E.; Meerholz, K.; Kauzlarich, S. M., Probing Electronics as a Function of Size and Surface of Colloidal Germanium Nanocrystals. *J. Phys. Chem. C* **2015,** 119, 5671–5678.

27. Muthuswamy, E.; Iskandar, A. S.; Amador, M. M.; Kauzlarich, S. M., Facile Synthesis of Germanium Nanoparticles with Size Control: Microwave versus Conventional Heating. *Chem. Mater.* **2013,** 25, 1416–1422.

28. Muthuswamy, E.; Zhao, J.; Tabatabaei, K.; Amador, M. M.; Holmes, M. A.; Osterloh, F. E.; Kauzlarich, S. M., Thiol-Capped Germanium Nanocrystals: Preparation and Evidence for Quantum Size Effects. *Chem. Mater.* **2014,** 26, 2138–2146.

29. Vaughn, D. D., II; Bondi, J. F.; Schaak, R. E., Colloidal Synthesis of Air-Stable Crystalline Germanium Nanoparticles with Tunable Sizes and Shapes. *Chem. Mater.* **2010,** 22, 6103–6108.

30. Ruddy, D. A.; Erslev, P. T.; Habas, S. E.; Seabold, J. A.; Neale, N. R., Surface Chemistry Exchange of Alloyed Germanium Nanocrystals: A Pathway Toward Conductive Group IV Nanocrystal Films. *J. Phys. Chem. Lett.* **2013,** 4, 416–421.

31. Armatas, G. S.; Kanatzidis, M. G., Mesoporous Compound Semiconductors from the Reaction of Metal Ions with Deltahedral $[Ge_9]^{4-}$ Clusters. *J. Am. Chem. Soc.* **2008,** 130, 11430–11436.

32. Armatas, G. S.; Kanatzidis, M. G., High-Surface-Area Mesoporous Germanium from Oxidative Polymerization of the Deltahedral $[Ge_9]^{4-}$ Cluster: Electronic Structure Modulation with Donor and Acceptor Molecule. *Adv. Mater.* **2008,** 20, 546–550.

33. Armatas, G. S.; Kanatzidis, M. G., Mesoporous Germanium-Rich Chalcogenido Frameworks with Highly Polarizable Surfaces and Relevance to Gas Separation. *Nat. Mater.* **2009,** 8, 217–222.

34. Armatas, G. S.; Kanatzidis, M. G., Size Dependence in Hexagonal Mesoporous Germanium: Pore Wall Thickness versus Energy Gap and Photoluminescence. *Nano Lett.* **2010,** 2010, 3330–3336.

35. Bag, S.; Trikalitis, P. N.; Chupas, P. J.; Armatas, G. S.; Kanatzidis, M. G., Porous Semiconducting Gels and Aerogels from Chalcogenide Clusters. *Science* **2007,** 317, 490–493.

36. Henderson, E. J.; Hessel, C. M.; Cavell, R. G.; Veinot, J. G. C., How Processing Atmosphere Influences the Evolution of GeO_2-Embedded Germanium Nanocrystals Obtained from the Thermolysis of Phenyl Trichlorogermane-Derived Polymers. *Chem. Mater.* **2010,** 22, 2653–2661.

37. Hoffman, M.; Veinot, J. G. C., Understanding the Formation of Elemental Germanium by Thermolysis of Sol-Gel Derived Organogermanium Oxide Polymers. *Chem. Mater.* **2012,** 24, 1283–1291.

38. Henderson, E. J.; Hessel, C. M.; Veinot, J. G. C., Synthesis and Photoluminescent Properties of Size-Controlled Germanium Nanocrystals from Phenyl Trichlorogermane-Derived Polymers. *J. Am. Chem. Soc.* **2008,** 130, 3624–3632.

39. Henderson, E. J.; Seino, M.; Puzzo, D. P.; Ozin, G. A., Colloidally Stable Germanium Nanocrystals for Photonic Applications. *ACS Nano* **2010,** 4, 7683–7691.

40. Henderson, E. J.; Veinot, J. G. C., Synthesis of Oxide Encapsulated and Freestanding Hydride Surface Terminated $Si_{1-x}Ge_x$ Nanocrystals. *Chem. Mater.* **2007,** 19, 1886–1888.

41. Wu, J.; Sun, Y.; Zou, R.; Song, G.; Chen, Z.; Wang, C.; Hu, J., One-Step Aqueous Solution Synthesis of Ge Nanocrystals from GeO_2 Powders. *CrystEngComm* **2011,** 13, 3674–3677.

42. Purkait, T. K.; Swarnakar, A. K.; De Los Reyes, G. B.; Hegmann, F. A.; Rivard, E.; Veinot, J. G. C., One-pot Synthesis of Functionalized Germanium Nanocrystals from a Single Source Precursor. *Nanoscale* **2015,** 7, 2241–2244.

43. Millo, O.; Balberg, I.; Azulay, D.; Purkait, T. K.; Swarnakar, A. K.; Rivard, E.; Veinot, J. G. C., Direct Evaluation of the Quantum Confinement Effect in Single Isolated Ge Nanocrystals. *J Phys. Chem. Lett.* **2015,** 6, 3396–3402.

44. Kim, C. H.; Im, H. S.; Cho, Y. J.; Jung, C. S.; Jang, D. M.; Myung, Y.; Kim, H. S.; Back, S. H.; Lim, Y. R.; Lee, C.-W.; Park, J., High-Yield Gas-Phase Laser Photolysis Synthesis of Germanium Nanocrystals for High-Performance Photodetectors and Lithium Ion Batteries. *J. Phys. Chem. C* **2012,** 116, 26190–26196.

45. Kim, S.; Walker, B.; Park, S. Y.; Choi, H.; Ko, S.-J.; Jeong, J.; Yun, M. H.; Lee, J. C.; Kim, D. S.; Kim, J. Y., Size Tailoring of Aqueous Germanium Nanoparticle Dispersions. *Nanoscale* **2014,** 6, 10156–10160.

46. Cho, Y. J.; Kim, C. H.; Im, H. S.; Myung, Y.; Kim, H. S.; Back, S. H.; Lim, Y. R.; Jung, C. S.; Jang, D. M.; Park, J., Germanium–Tin Alloy Nanocrystals for High-Performance Lithium Ion Batteries. *Phys. Chem. Chem. Phys.* **2013,** 15, 11691–11695.

47. Shirahata, N.; Hirakawa, D.; Masuda, Y.; Sakka, Y., Size-Dependent Color Tuning of Efficiently Luminescent Germanium Nanoparticles. *Langmuir* **2013,** 29, 7401–7410.

48. Nolan, B. M.; Chan, E. K.; Zhang, X.; Muthuswamy, E.; van Benthem, K.; Kauzlarich, S. M., Sacrificial Silver Nanoparticles: Reducing GeI2 To Form Hollow Germanium Nanoparticles by Electroless Deposition. *ACS Nano* **2016,** 10, 5391–5397.

49. Meng, A. C.; Fenrich, C. S.; Braun, M. R.; McVittie, J. P.; Marshall, A. F.; Harris, J. S.; McIntyre, P. C., Core/Shell Germanium/Germanium-Tin Nanowires Exhibiting Room Temperature Direct-and Indirect-Gap Photoluminescence. *Nano Lett.* **2016,** 16, 7521–7529.

50. Biswas, S.; Doherty, J.; Saladukha, D.; Ramasse, Q.; Majumdar, D.; Upmanyu, M.; Singha, A.; Ochalski, T.; Morris, M. A.; Holmes, J. D., Non-Equilibrium Induction of Tin in Germanium: Towards Direct Bandgap $Ge_{1-x}Sn_x$ Nanowires. *Nat. Commun.* **2016,** 7, 11405-1–11405-12.

51. Stoldt, C. R.; Haag, M. A.; Larsen, B. A., Preparation of Freestanding Germanium Nanocrystals by Ultrasonic Aerosol Pyrolysis. *Appl. Phys. Lett.* **2008,** 93, 043125-1–043125-3.

52. Ma, X.; Wu, F.; Kauzlarich, S. M., Alkyl-Terminated Crystalline Ge Nanoparticles Prepared From NaGe: Synthesis, Functionalization and Optical Properties. *J. Solid State Chem.* **2008,** 181, 1628–1633.

53. Wheeler, L. M.; Levij, L. M.; Kortshagen, U. R., Tunable Band Gap Emission and Surface Passivation of Germanium Nanocrystals Synthesized in the Gas Phase. *J. Phys. Chem. Lett.* **2013,** 4, 3392–3396.

54. Gresback, R.; Holman, Z.; Kortshagen, U., Plasma Synthesis of Highly Monodisperse Ge Nanocrystals and Self-Assembly of Dense Nanocrystal Layers. *Mat. Res. Soc. Symp. Proc.* **2007,** 974, 0974-CC05.

55. Gresback, R.; Holman, Z.; Kortshagen, U., Nonthermal Plasma Synthesis of Size-Controlled, Monodisperse, Freestanding Germanium Nanocrystals. *Appl. Phys. Lett.* **2007,** 91, 093119-1–093119-3.

56. Wheeler, L. M.; Nichols, A. W.; Chernomordik, B. D.; Anderson, N. C.; Beard, M. C.; Neale, N. R., All-Inorganic Germanium Nanocrystal Films by Cationic Ligand Exchange. *Nano Lett.* **2016,** 16, 1949–1954.

57. Warner, J. H., Solution-Phase Synthesis of Germanium Nanoclusters Using Sulfur. *Nanotechnology* **2006,** 19, 5613–5619.

58. Zaitseva, N.; Dai, Z. R.; Grant, C. D.; Harper, J.; Saw, C., Germanium Nanocrystals Synthesized in High-Boiling-Point Organic Solvents. *Chem. Mater.* **2007,** 19, 5174–5178.

59. Ramasamy, K.; Kotula, P. G.; Fidler, A. F.; Brumbach, M. T.; Pietryga, J. M.; Ivanov, S. A., Sn_xGe_{1-x} Alloy Nanocrystals: A First Step toward Solution-Processed Group IV Photovoltaics. *Chem. Mater.* **2015,** 27, 4640–4649.

60. Barth, S.; Seifner, M. S.; Bernardi, J., Microwave-Assisted Solution–Liquid–Solid Growth of $Ge_{1-x}Sn_x$ Nanowires with High Tin Content. *Chem. Commun.* **2015,** 51, 12282–12285.

61. Seifner, M. S.; Biegger, F.; Lugstein, A.; Bernardi, J.; Barth, S., Microwave-Assisted $Ge_{1-x}Sn_x$ Nanowire Synthesis: Precursor Species and Growth Regimes. *Chem. Mater.* **2015,** 27, 6125–6130.

62. Tonkikh, A. A.; Zakharov, N. D.; Suvorova, A. A.; Eisenschmidt, C.; Schilling, J.; Werner, P., Cubic Phase Sn-Rich GeSn Nanocrystals in a Ge Matrix. *Cryst. Growth Des.* **2014,** 14, 1617–1622.

63. Bodnarchuk, M. I.; Kravchyk, K. V.; Krumeich, F.; Wang, S.; Kovalenko, M. V., Colloidal Tin-Germanium Nanorods and Their Li-Ion Storage Properties. *ACS Nano* **2014,** 8, 2360–2368.

64. D'Costa, V. R.; Cook, C. S.; Birdwell, A. G.; Littler, C. L.; Canonico, M.; Zollner, S.; Kouvetakis, J.; Menéndez, J., Optical Critical Points of Thin-Film $Ge_{1-y}Sn_y$ Alloys: A Comparative $Ge_{1-y}Sn_y/Ge_{1-x}Si_x$ Study. *Phys. Rev. B* **2006,** 73, 125207-1–125207-16.

65. Li, S. F.; Bauer, M. R.; Menéndez, J.; Kouvetakis, J., Scaling Law for the Compositional Dependence of Raman Frequencies in SnGe and GeSi Alloys. *Appl. Phys. Lett.* **2004,** 84, 867–869.

66. Dag, Ö.; Henderson, E. J.; Ozin, G. A., Synthesis of Nanoamorphous Germanium and Its Transformation to Nanocrystalline Germanium. *Small* **2012,** 8, 921–929.

67. Robel, I.; Shabaev, A.; Lee, D. C.; Schaller, R. D.; Pietryga, J. M.; Crooker, S. A.; Efros, A. L.; Klimov, V. I., Temperature and Magnetic-Field Dependence of Radiative Decay in Colloidal Germanium Quantum Dots. *Nano Lett.* **2015,** 15, 2685–2692.

68. Du, W.; Ghetmiri, S. A.; Conley, B. R.; Mosleh, A.; Nazzal, A.; Soref, R. A.; Sun, G.; Tolle, J.; Margetis, J.; Naseem, H. A., Competition of Optical Transitions Between Direct and Indirect Bandgaps in $Ge_{1-x}Sn_x$. *Appl. Phys. Lett.* **2014,** 105, 051104.

69. Wirths, S.; Geiger, R.; Von Den Driesch, N.; Mussler, G.; Stoica, T.; Mantl, S.; Ikonic, Z.; Luysberg, M. l.; Chiussi, S.; Hartmann, J. M., Lasing in Direct-Bandgap GeSn Alloy Grown on Si. *Nat. Photon.* **2015,** 9, 88–92.

70. Esteves, R. J. A.; Hafiz, S.; Demchenko, D. O.; Özgür, Ü.; Arachchige, I. U., Ultra-Small $Ge_{1-x}Sn_x$ Quantum Dots with Visible Photoluminescence. *Chem. Commun.* **2016,** 52, 11665–11668.

71. Hafiz, S. A.; Esteves, R. J. A.; Demchenko, D. O.; Arachchige, I. U.; Özgür, U., Energy Gap Tuning and Carrier Dynamics in Colloidal $Ge_{1-x}Sn_x$ Quantum Dots. *J. Phys. Chem. Lett.* **2016,** 7, 3295–3301.

72. Pezzoli, F.; Giorgioni, A.; Patchett, D.; Myronov, M., Temperature-Dependent Photoluminescence Characteristics of GeSn Epitaxial Layers. *ACS Photonics* **2016,** 3, 2004–2009.

73. Chen, Y.; Vela, J.; Htoon, H.; Casson, J. L.; Werder, D. J.; Bussian, D. A.; Klimov, V. I.; Hollingsworth, J. A., “Giant” Multishell CdSe Nanocrystal Quantum Dots With Suppressed Blinking. *J. Am. Chem. Soc.* **2008,** 130, 5026–5027.

74. Tan, R.; Yuan, Y.; Nagaoka, Y.; Eggert, D.; Wang, X.; Thota, S.; Guo, P.; Yang, H.; Zhao, J.; Chen, O., Monodisperse Hexagonal Pyramidal and Bipyramidal Wurtzite CdSe-CdS Core–Shell Nanocrystals. *Chem. Mater.* **2017,** 29, 4097–4108.

75. Sainz, M.; Pérez-Rontomé, C.; Ramos, J.; Mulet, J. M.; James, E. K.; Bhattacharjee, U.; Petrich, J. W.; Becana, M., Plant Hemoglobins May Be Maintained in Functional Form by Reduced Flavins in the Nuclei, and Confer Differential Tolerance to Nitro-Oxidative Stress. *Plant J.* **2013,** 76, 875-887.

76. Olesinski, R. W.; Abbaschian, G. J., The Ge–Sn (Germanium–Tin) System. *Bull. Alloy Phase Diagrams* **1984,** 5, 265–271.

77. Rojas-Lopez, M.; Navarro-Contreras, H.; Desjardins, P.; Gurdal, O.; Taylor, N.; Carlsson, J.; Greene, J., Raman Scattering from Fully Strained $Ge_{1-x}Sn_x$ (x<= 0.22) Alloys Grown on Ge (001) 2x1 by Low-Temperature Molecular Beam Epitaxy. *J. Appl. Phys.* **1998,** 84, 2219–2223.

78. Su, S.; Wang, W.; Cheng, B.; Hu, W.; Zhang, G.; Xue, C.; Zuo, Y.; Wang, Q., The Contributions of Composition and Strain to the Phonon Shift in Alloys. *Solid State Commun.* **2011,** 151, 647–650.

79. Gupta, R.; Xiong, Q.; Mahan, G. D.; Eklund, P. C., Surface Optical Phonons in Gallium Phosphide Nanowires. *Nano Lett.* **2003,** 3, 1745–1750.

80. Tschirner, N.; Lange, H.; Schliwa, A.; Biermann, A.; Thomsen, C.; Lambert, K.; Gomes, R.; Hens, Z., Interfacial Alloying in CdSe/CdS Heteronanocrystals: A Raman Spectroscopy Analysis. *Chem. Mater.* **2012,** 24, 311–318.

81. Lange, H.; Artemyev, M.; Woggon, U.; Thomsen, C., Geometry Dependence of the Phonon Modes in CdSe Nanorods. *Nanotechnology* **2009,** 20, 045705-1–045705-5.

82. Micoulaut, M.; Cormier, L.; Henderson, G. S., The Structure of Amorphous, Crystalline and Liquid GeO_2. *J. Phys.: Condens. Matter* **2006,** 18, R753–R784.

83. Li, J. J.; Wang, Y. A.; Guo, W.; Keay, J. C.; Mishima, T. D.; Johnson, M. B.; Peng, X., Large-Scale Synthesis of Nearly Monodisperse CdSe/CdS Core/Shell Nanocrystals

Using Air-Stable Reagents via Successive Ion Layer Adsorption and Reaction. *J. Am. Chem. Soc.* **2003,** 125, 12567–12575.

84. Lopez, F. J.; Givan, U.; Connell, J. G.; Lauhon, L. J., Silicon Nanowire Polytypes: Identification by Raman Spectroscopy, Generation Mechanism, and Misfit Strain in Homostructures. *ACS Nano* **2011,** 5, 8958–8966.

85. Mélinon, P.; Masenelli, B.; Tournus, F.; Perez, A., Playing With Carbon and Silicon at the Nanoscale. *Nat. Mater.* **2007,** 6, 479–490.

86. Segarra, C.; Rajadell, F.; Climente, J. I.; Planelles, J., Influence of Polytypism on the Electronic Structure of CdSe/CdS and CdSe/CdSe Core/Shell Nanocrystals. *J. Phys. Chem. C* **2017,** 121, 6386–6392.

87. Bertoni, G.; Grillo, V.; Brescia, R.; Ke, X.; Bals, S.; Catellani, A.; Li, H.; Manna, L., Direct Determination of Polarity, Faceting, and Core Location in Colloidal Core/Shell Wurtzite Semiconductor Nanocrystals. *ACS Nano* **2012,** 6, 6453–6461.

88. McBride, J.; Treadway, J.; Feldman, L. C.; Pennycook, S. J.; Rosenthal, S. J., Structural Basis for Near Unity Quantum Yield Core/Shell Nanostructures. *Nano Lett.* **2006,** 6, 1496–1501.

89. Rosenthal, S. J.; McBride, J.; Pennycook, S. J.; Feldman, L. C., Synthesis, Surface Studies, Composition and Structural Characterization of CdSe, Core/Shell and Biologically Active Nanocrystals. *Surf. Sci. Rep.* **2007,** 62, 111–157.

90. Guo, Y.; Marchuk, K.; Sampat, S.; Abraham, R.; Fang, N.; Malko, A. V.; Vela, J., Unique Challenges Accompany Thick-Shell CdSe/nCdS (n> 10) Nanocrystal Synthesis. *J. Phys. Chem. C* **2012,** 116, 2791–2800.

Supporting Information

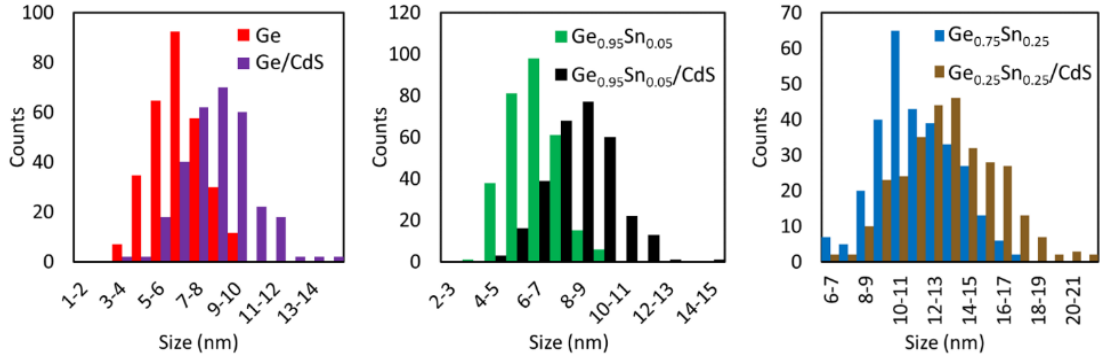

Figure S1. TEM size distribution plots for Ge and $Ge_{1-x}Sn_x$ nanocrystals and core/shell nanocrystals made via overlaying with CdS.

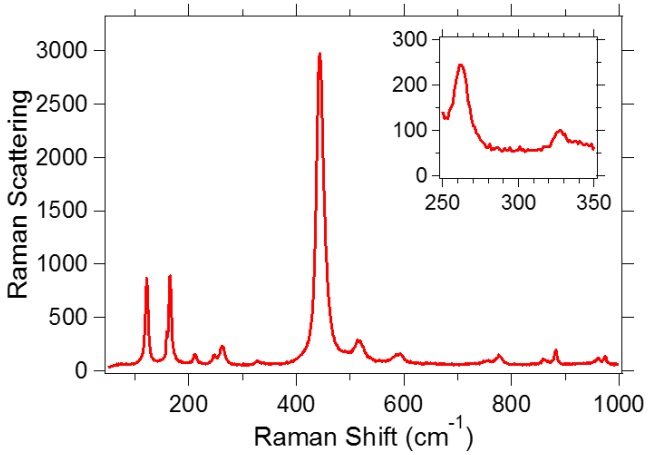

Figure S2. Raman spectrum of solid GeO_2.

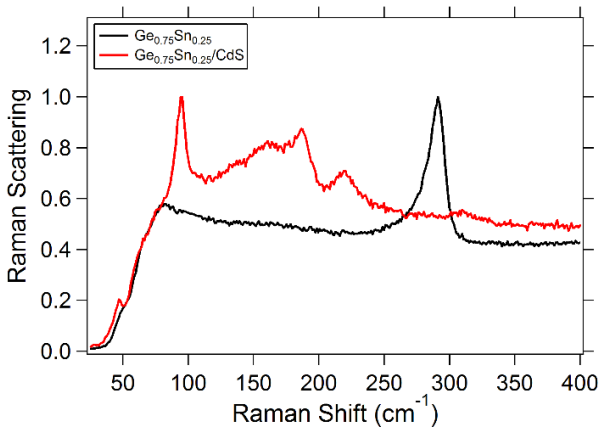

Figure S3. Raman spectrum of the $Ge_{0.75}Sn_{0.25}$ and $Ge_{0.75}Sn_{0.25}$/CdS core/shell nanocrystals made with crude core solution. The core/shell sample show bands that correlate to reported Raman peaks of SnS at ~95, 190, and 220 cm^{-1}.

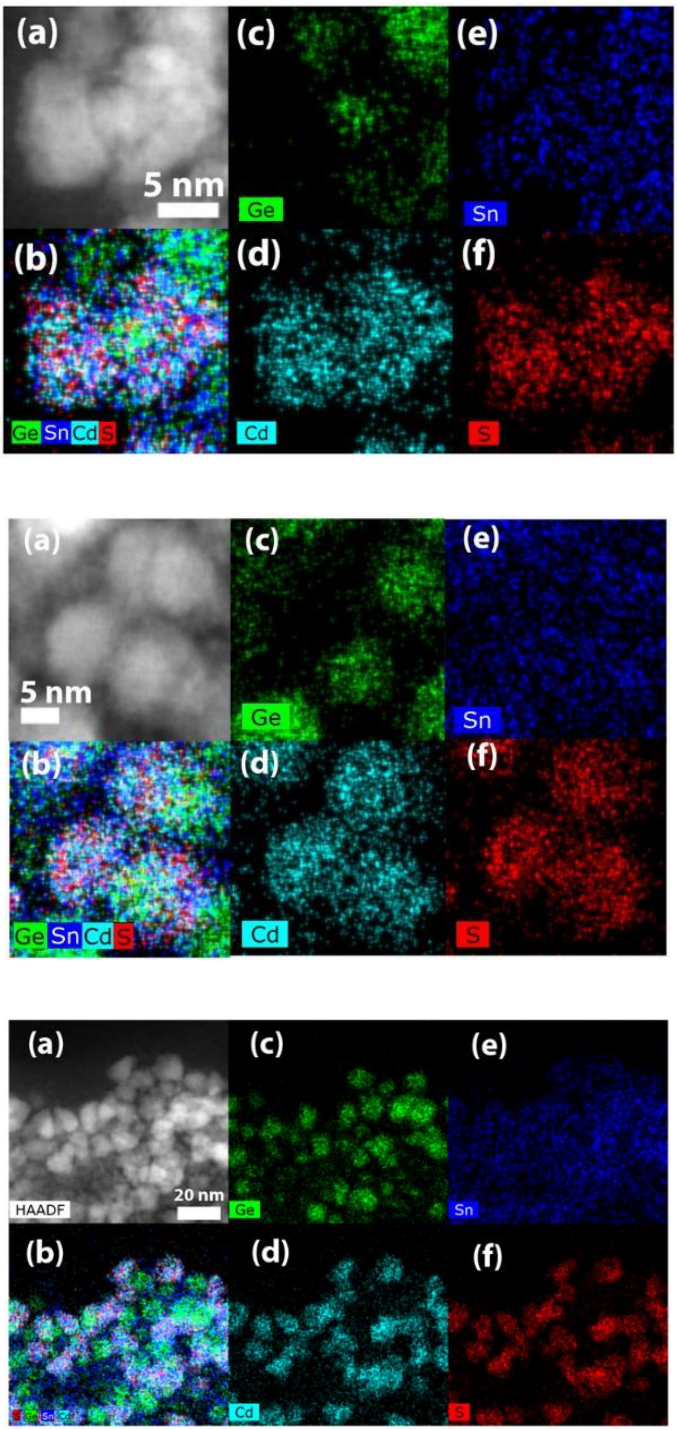

Figure S4. Three representative sets of (a) high-resolution HAADF STEM images of $Ge_{0.75}Sn_{0.25}$/CdS nanocrystals with registered EDX elemental mapping for (b) Ge, Sn, Cd, and S, (c) Ge, (d) Cd, (e) Sn, and (f) S.

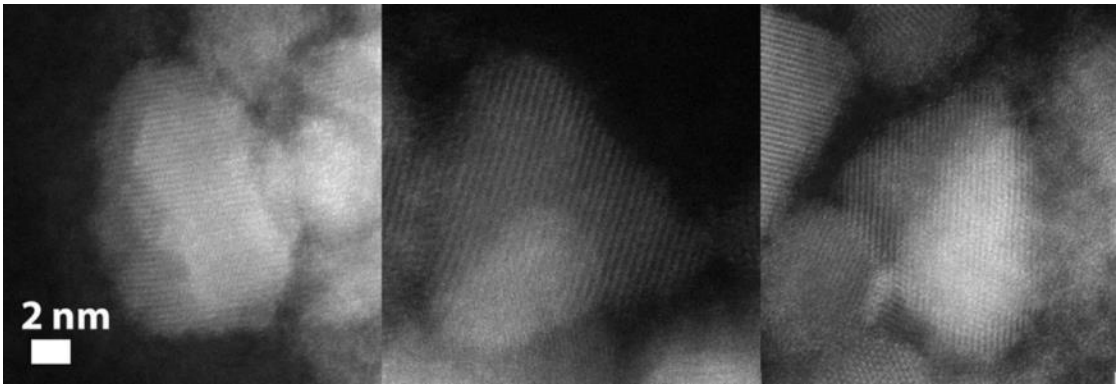

Figure S5. Three sample high resolution high-angle annular dark-field (HAADF) STEM images of a $Ge_{0.75}Sn_{0.25}$/CdS nanocrystals. The average atomic number (Z) of the CdS shell, 32, is similar to that of the Ge core material, 32, making contrast comparisons difficult. However, the presence of continuous lattice fringes throughout each particle is an indication of crystallinity across these core/shell particles.

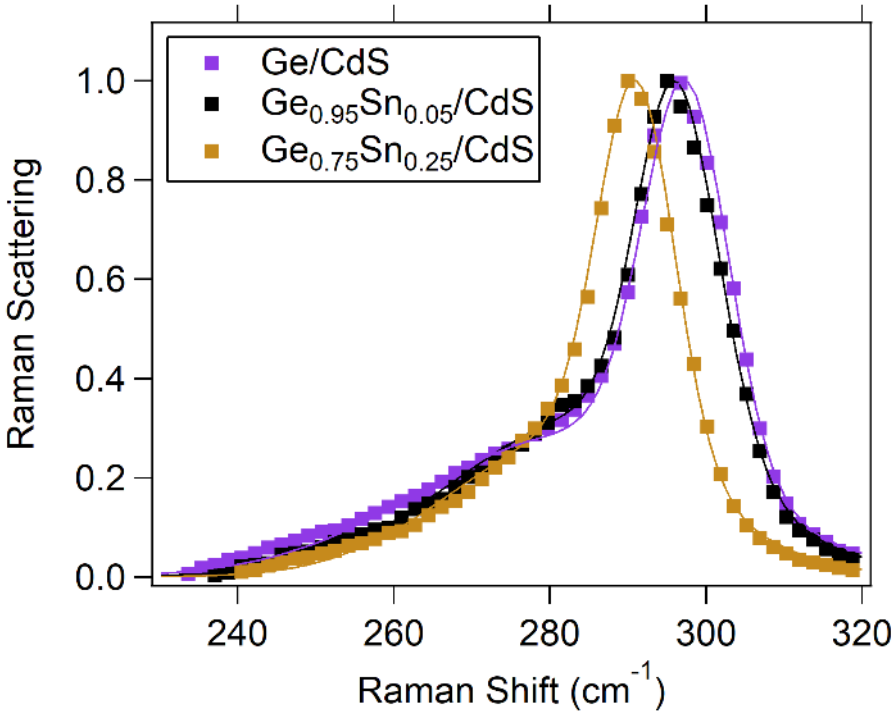

Figure S6. Raman spectra of the $Ge_{1-x}Sn_x$/CdS core/shell nanocrystals.

Table S1. Summary of Raman peak locations of the Ge-Ge LO and SO phonon modes for the Ge and $Ge_{1-x}Sn_x$ nanocrystals and core/shell nanocrystals. Each value is an average of 5 replicate measurements. All 5 replicate spectra were fit to 2-peak Gaussian curves to account for asymmetry due to the SO phonon appearing at lower wavenumbers, and the values were subsequently averaged to produce these data.

Sample	Longitudinal Optical Phonon Mode		Surface Optical Phonon Mode	
	Location (cm^{-1})	FWHM (cm^{-1})	Location (cm^{-1})	FWHM (cm^{-1})
Ge cores	296.4 ± 0.4	11.4 ± 0.6	283.0 ± 0.6	47 ± 4
$Ge_{0.95}Sn_{0.05}$	295.2 ± 0.5	13 ± 3	283 ± 2	60 ± 10
$Ge_{0.75}Sn_{0.25}$	292 ± 1	19 ± 3	280 ± 10	60 ± 10
Ge/CdS	297.5 ± 0.5	12.7 ± 0.5	283 ± 1	47 ± 2
$Ge_{0.95}Sn_{0.05}$/CdS	295 ± 1	10.6 ± 0.9	286 ± 1	36.9 ± 0.6
$Ge_{0.75}Sn_{0.25}$/CdS	291.1 ± 0.5	11.5 ± 0.6	282.8 ± 0.6	36.4 ± 0.7

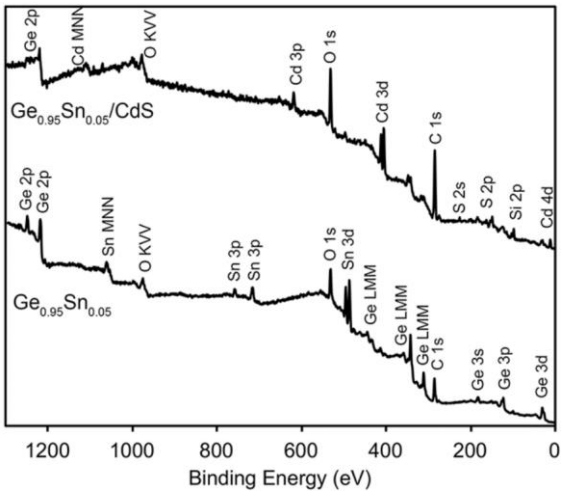

Figure S7. XPS survey spectra for Ge and $Ge_{1-x}Sn_x$ core and core/shell nanocrystals. Samples indicated at the lower left of each trace.

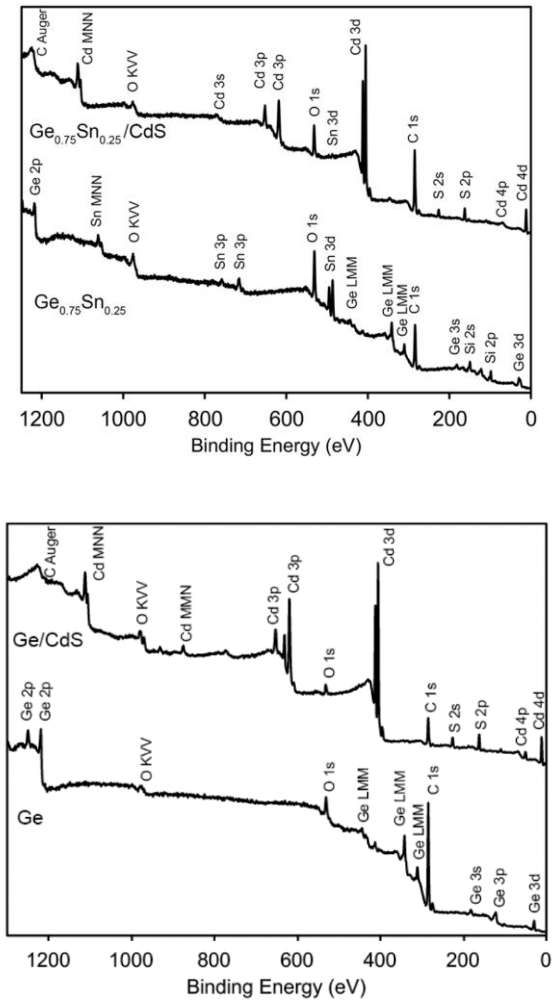

Figure S7. (continued) XPS survey spectra for Ge and $Ge_{1-x}Sn_x$ core and core/shell nanocrystals. Samples indicated at the lower left of each trace.

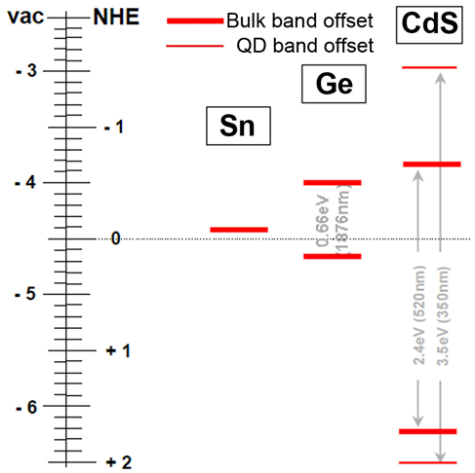

Figure S8. Plot of valence and conduction band offsets for Ge, Sn, and CdS.

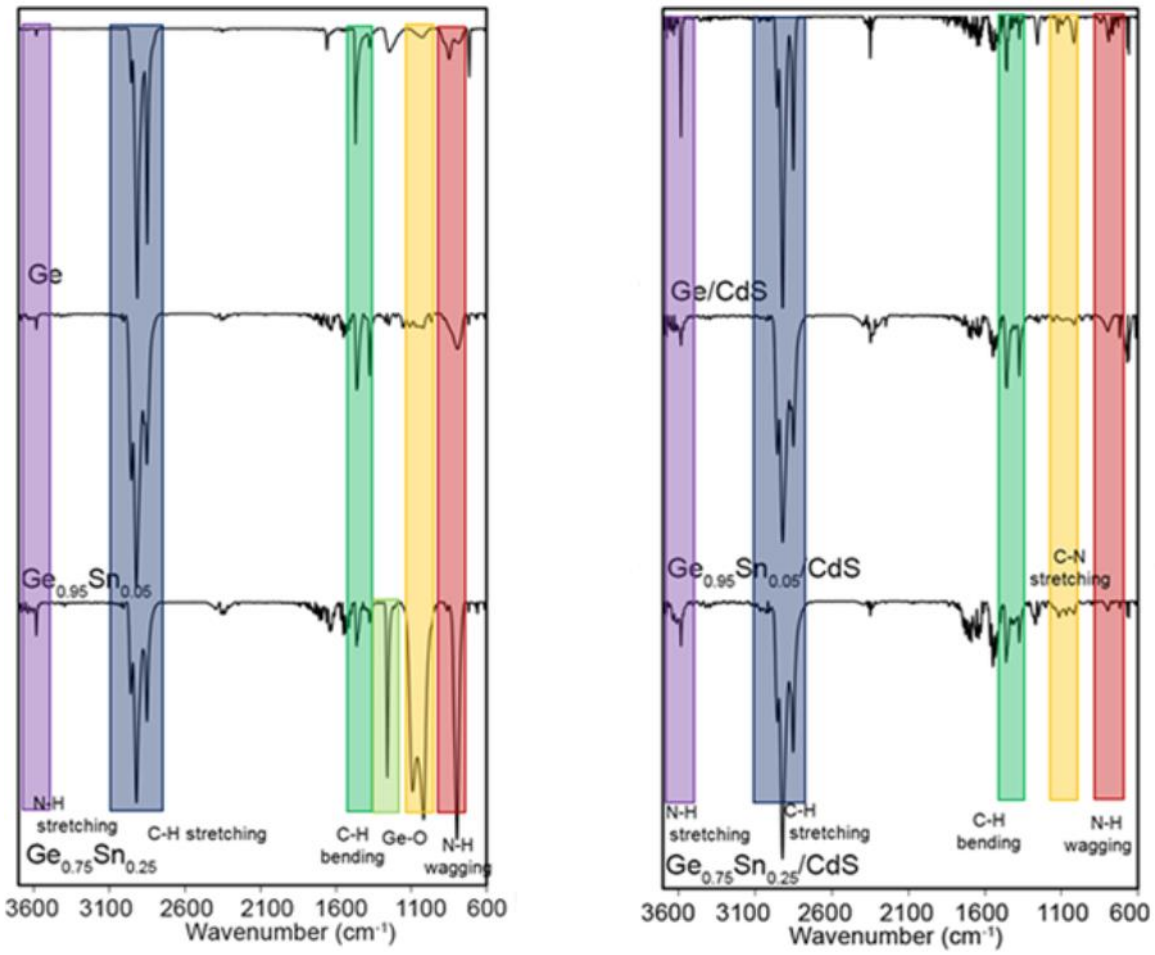

Figure S9. Fourier transform infrared spectra of Ge and $Ge_{1-x}Sn_x$ core (left) and core/shell (right) nanocrystals. Note the intense Ge-O band in the $Ge_{0.75}Sn_{0.25}$ sample, corresponding to increased oxidation in that sample. In another set of experiments no oxidation was measured in the $Ge_{0.75}Sn_{0.25}$ sample as explained in the text.

CHAPTER 6. CONCLUSION

In conclusion, we investigated the different synthetic approaches of halide perovskites and germanium semiconductors. In Chapter 2, we report the synergetic effects of halide and bulky alkylammonium cation incorporation on tuning emission energy of halide perovskites. We also demonstrated the role of excess precursor on photoluminescence stability in nanostructured perovskites. In Chapter 3, we discuss synthesis of perovskite nanocrystals using antimony perovskites as ligands. In Chapter 4, We describe the synthetic approaches of lead-free germanium perovskites and the feasibility of manganese incorporation in germanium perovskites. In addition to perovskite semiconductors, we also discussed the synthesis exploration of $Ge_{1-x}Sn_x$ alloy nanocrystals and $Ge_{1-x}Sn_x$ core/shell nanocrystals with enhanced near infrared photoluminescence in Chapter 5.

We combine composition-control with dimensionality-control of organometal halide perovskite crystals by tuning halide-incorporation and exploiting bulky alkylammonium cations as capping ligands. We demonstrate a systematic synthesis of all the series of mixed halide perovskite polycrystals and their low dimensional analogues. Emission spectra of mixed halide perovskites cover the whole visible light region from 400 nm to 780 nm. The quantum yield of bromide perovskites is up to 44%. Also, we noticed the emission spectrum of perovskite nanocrystals has a reversible photo-induced photoluminescence peak transition. We speculate this PL peak is derived from surface traps. By optimizing synthetic conditions, we are able to inhibit the appearance of a reversible photoinduced PL peak derived from surface traps.

To address the concerns about the heavy element lead in conventional lead perovskites, we successfully synthesized antimony doped lead perovskite nanocrystals employing a surfactant-free method. By adding precursor solution into a non-polar solvent,

$CH_3NH_3PbI_3$-$(CH_3)_3Sb_2I_9$ nanocrystals can be crashed out. By introducing SbI_3 to partially replace PbI_2 in the precursor lead perovskite solution, layered $(CH_3)_3Sb_2I_9$ covers the surface of $CH_3NH_3PbI_3$ and terminates crystal growth during the crash-out process. The hybrid nanocrystals synthesized with $(CH_3)_3Sb_2I_9$ show higher PL quantum yield than bulk $CH_3NH_3PbI_3$. Nanocrystals prepared with only n-octylammonium have a higher PL intensity than those prepared in the presence of both n-octylammonium and $(CH_3)_3Sb_2I_9$. Nanocrystals prepared using $(CH_3)_3Sb_2I_9$ may be idealized in the photo-electronic devices, as no organic ligands are present on the perovskite surface that inhibit charge transport using the Sb film.

We also developed a synthetic approach to germanium perovskites and their nanocrystals. $CsGeI_3$ exhibits a similar bandgap (1.6 eV) and corner-sharing octahedra network as lead perovskites that are potentially promising for photovoltaics. Size control of $CsGeI_3$ perovskite nanocrystals is achieved by using cysteammonium cations as capping ligands. Diffraction peak broadening in powder XRD and TEM images corroborate the successful size control without introducing impurities. Diffuse reflectance measurements also reveal a bandgap blue-shift of 0.05 eV in the nanocrystals. Because the sizes of the nanocrystals are much larger than the Bohr radius, it is unlikely this blue shift is the result of quantum confinement. In addition, we have also doped Mn^{2+} into $CsGeI_3$ lattice. XRD patterns show a lattice expansion with increasing manganese iodide loading, which we believed is caused by the substitution of Ge^{2+} by larger Mn^{2+}. The manganese incorporation percentage is up to 29% according to Vegard's law. EPR analysis also confirms the presence of Mn^{2+} and indicates Mn^{2+} sites are highly distorted, which is in good agreement with Ge^{2+} sites in $CsGeI_3$. We expect these results will extend the arsenal of perovskites, especially the lead-free ones, beyond photovoltaics and to the fields of spintronics and magnetic data storage.

In addition to perovskite semiconductor, we expand our research interest to germanium semiconductor. To get a direct bandgap germanium semiconductor, $Ge_{1-x}Sn_x$ alloy nanocrystals and $Ge_{1-x}Sn_x$ core/shell nanocrystals were prepared *via* solution-based synthesis. Incorporation of Sn was confirmed by XRD and Raman peak shift. Tin itself did not increase the PL intensity in the cores, but core/shell nanocrystals prepared using the Sn-doped cores and CdS shell show up to 15× enhanced PL when compared to Ge/CdS materials. This could be explained by improved epitaxy between the lattice-expanded Sn-doped Ge cores and the structurally similar CdS shell, along with reduced surface oxidation. The combination of scalability and improved PL intensities make these $Ge_{1-x}Sn_x$ core/shell nanocrystals promising alternatives to other near infrared-active materials for use as functional materials in solar cells, LEDs and bio-imaging.

APPENDIX. ROLE OF EXCESS PRECURSOR ON PHOTOLUMINESCENCE STABILITY

Daniel J. Freppon, Ujjal Bhattacharjee, Jacob W. Petrich, Emily A. Smith

PL Lifetime Measurements. PL lifetime measurements were performed with a time-correlated single-photon counting (TCSPC) technique. Here, we used different excitation wavelengths of 500 nm, 570 nm and 638 nm. 500 nm and 570 nm were generated using a supercontinuum laser (Fianium Ltd.) with 10 nm band-pass filters and laser repetition rate of 1 MHz. 638 nm was generated using a pulse diode laser from PicoQuant (model PDL 800-B) using a repetition rate of 5-MHz. A Becker & Hickl photon counting card (model SPC-630) was used with a MCP-PMT detector. With this system, the full width at half-maximum of the instrument response function (IRF) was ~200 ps. A 1 cm path length cuvette was used. Longpass filters or a monochromator were used to collect emission in order to eliminate scattered excitation light and collect the decay for a particular wavelength band. The decay parameters were calculated by fitting the decay to a sum of exponentials after deconvolution of the IRF from the decay. *Time-Resolved PL Emission Measurements*. Time-resolved emission spectra (TRES) were measured with a home built nanosecond setup. A Continuum Surelite II laser (5ns, 20 Hz) was used. A 532 nm or a third-harmonic 355 nm were used as excitation wavelengths. Spectra were collected at different times after the laser pulse with a synchronized ICCD camera coupled with a spectrograph. Samples were measured in toluene solution in 1 cm path length cuvettes. Absorption and photoluminescence spectra were monitored before and after the laser experiment.

Single Particle Fluorescence Microscopy. Single particle fluorescence microscopy was performed using an inverted microscope (Nikon Eclipse TE2000U, Melville, NY, USA). Perovskite solutions (toluene, ~0.3 mM, 50 μL) were sonicated for 60 min before drop casting onto a glass microscope coverslip (Carlson Scientific, Peotone, IL). A mercury

lamp was used for excitation (XCite 120 PC, EXFO Photonic Solutions Inc., Quebec City). Excitation and emission filters were from Omega Optical (Brattleboro, VT, USA), unless noted otherwise. 545-530 nm excitation and 700-775 nm emission filters were used for $CH_3NH_3PbI_3$, 620-650/25 nm excitation and 690-670 nm emission filters $CH_3NH_3Pb(Br_{0.25}I_{0.75})_3$, 500-520 nm excitation and 629/56 nm emission filters (in this case, from Semrock, Inc., Lake Forest, IL, USA) $CH_3NH_3Pb(Br_{0.50}I_{0.50})_3$, and 500-520 nm excitation and 535-530 nm emission filters for $CH_3NH_3Pb(Br_{0.75}I_{0.25})_3$ and $CH_3NH_3PbI_3$. A 100× PlanApo, 1.49 numerical aperture oil-immersion objective was used and PL images were collected using a PhotonMAX 512 EMCCD camera (Princeton Instrument, Trenton, NJ, USA) with a 20 ms exposure time. A gain of 3000 was used for all of the samples, except no gain was used for $CH_3NH_3PbI_3$ perovskites.

Luminescence Microscopy. A lab-built luminescence microscope based on a DM IRBE platform (Leica, Wetzlar, Germany) with a laser excitation of 532 nm for $CH_3NH_3PbI_3$ (Sapphire SF 532 nm, Coherent, Santa Clara, CA, USA) or 488 nm for $CH_3NH_3PbBr_3$ (Argon Ion 488 nm, Uniphase, San Jose, CA) was used. A 100× HCX PL APO, 0.25 numerical aperture oil-immersion objective (Leica) was used to achieve a laser spot with a diameter of 0.28 ± 0.03 μm. The excitation power density at the sample was 1.6×10^5 $W \cdot cm^{-2}$. PL was collected from the epi-direction and focused onto a HoloSpec f/1.8i spectrograph (Kaiser Optical Systems, Ann Arbor, MI, USA), equipped with a broad range grating (HFG-650, Kaiser Optical Systems) then directed to a charged coupled device (CCD) (Newton 940, Andor Technology, Belfast, UK). Collection or binning time was 0.05 s. A series of 2400 spectra were collected every 0.09873 seconds.

Time-resolved photoluminescence decays of low-dimensional (Figure 1) and polycrystalline $CH_3NH_3PbX_3$ crystals demonstrate radiative lifetimes in the range of 5−84

ns with faster emission in bulk crystals. Single halide perovskites also exhibit a longer lifetime than mixed halide perovskites.

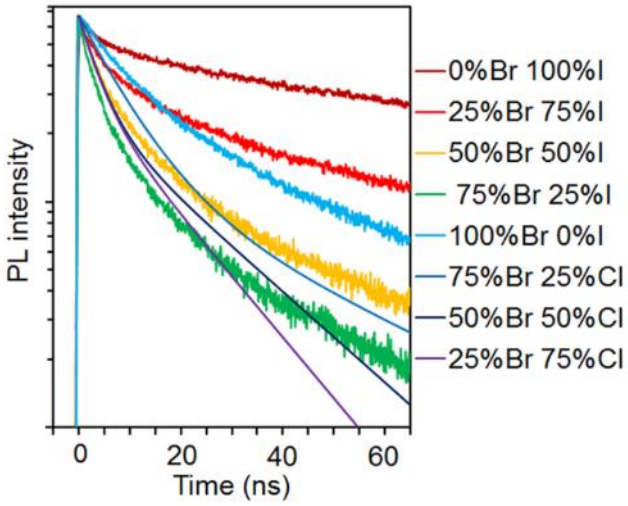

Figure 1. Time-resolved PL decay of low dimensional mixed-halide organolead perovskites (except 100%Cl for its low PL intensity not detectable by our instruments).

Synthesis-Dependent Formation of Reversible Surface Traps: Effect of Excess Halide Precursor. Adding octylammonium may introduce some impurities into the system. For example, 25%Br 75%I shows peaks in addition to the main peak at 646 nm (Figure 2). This red PL peak might come from iodine-enriched domains in the samples or some species produced by the reaction of octylammonium halides and lead halides on the surface of perovskite nanocrystals. It is reported that RNH_3PbI_3 has a smaller bandgap with longer carbon chains in R. The Bohr radii for bromide and iodide perovskites are 2 and 2.2 nm, so no quantum confinement effect should take place in absorption or emission spectra, which further agrees with the results of our optical measurements.

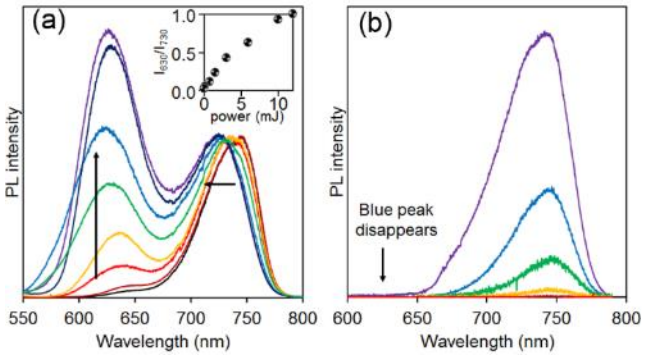

Figure 2. (a) Emission spectra of low-dimensional $CH_3NH_3PbI_3$ as a function of excitation power, normalized at 730 nm; (b) Time resolved emission spectra (TRES) of low-dimensional $CH_3NH_3PbI_3$ taken at a gap of 5 ns. The laser energy is 5 mJ.

In an earlier synthetic method, we used a 1: 6 ratio of lead halide and alkylammonium halides (a: b: c = 1: 3: 3) to fabricate low-dimensional perovskites. The fresh solution shows the characteristic emission peak around 730 nm along with a blue-shifted emission peak around 630 nm. This bluer peak is excitation power-dependent: the intensity increases with higher laser power as shown in Fig. 2a. We collected *in situ* XRD during illumination; however, no additional peaks were observed. These results indicate that this blue PL peak comes from surface trap states. To eliminate this peak, we optimized the synthetic method and successfully fabricated perovskites without the bluer peak. Fig. 7b shows time resolved emission spectra (TRES) of a fresh, low-dimensional $CH_3NH_3PbI_3$ solution made from the optimized synthetic method (a: b: c = 1: 1.5: 1.5). Apparently, no blue peak is observed in this sample, which implies the optimized method can synthesize trap-free organometal mixed-halide perovskites.

To examine the stability of perovskites prepared by the new synthetic method along with the effect of purification, we performed a purification experiment: a batch of 24-hour-aged perovskite toluene solution, prepared by the optimized method, divided into four solutions. Two were precipitated and resuspended in either pure toluene or an alkylammonium halide toluene solution with an alkylammonium halide concentration

equal to the precursor solution, labelled as ‘washed’ and ‘washed with excess RNH_3I’; another sample was given excess RNH_3I to achieve an equal concentration as the precursor solution and was labelled as ‘unwashed with excess RNH_3I’; the last sample was not changed and was labelled ‘unwashed’. As shown in Fig. 3, emission spectra of washed sample are the most stable throughout the experiment, which illustrates purification increase the stability of the sample. Both the sample washed with excess RNH_3I and the unwashed sample show PL decay within 100 seconds; however, their PL maxima do not shift dramatically. As for the unwashed sample with excess RNH_3I, PL maxima shift from 685 nm to 765 nm with increasing PL intensity, which is consistent with previous observations. The blue peak gradually disappears whereas the red peak increases with aging time. $CH_3NH_3PbBr_3$ is more stable compared to $CH_3NH_3PbI_3$ because the maximum PL shift is only 17 nm, from 528 nm to 545 nm (Fig. 3 and 4).

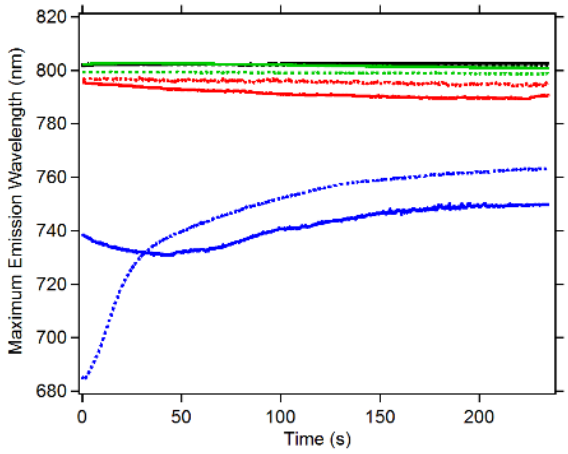

Figure 3. Plots of peak luminescence versus illumination time with a 532 nm laser (1.58×10^5 W/cm^2) for 100%I perovskites synthesized using a 1 PbI_2 : 1.5 CH_3NH_3PbI : 1.5 $C_8H_{17}NH_3I$ precursor ratio. A control experiment where samples are synthesized (black) with and (red) without a final wash step. The (green) washed and (blue) unwashed samples were then exposed to excess precursor. The addition of excess precursor revealed that a PL emission peak near 800 nm is observed unless the samples were unwashed. In the

unwashed sample, the addition of excess precursor leads to a shift in the photoluminescence spectra to maxima of 750 – 765 nm.

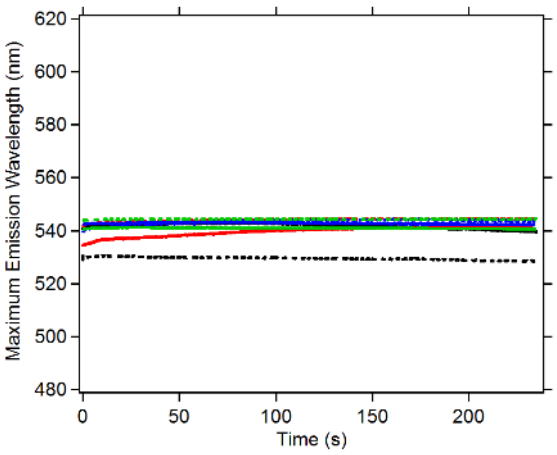

Figure 4. Plots of luminescence versus illumination time with a 488 nm laser (1.58×10^5 W/cm^2) for 100%Br perovskites synthesized using a 1 $PbBr_2$: 1.5 CH_3NH_3PbBr : 1.5 $C_8H_{17}NH_3Br$ precursor ratio. A control experiment where samples are synthesized (black) with and (red) without a final wash step. The (green) washed and (blue) unwashed samples were then exposed to excess precursor. All samples have a PL emission peak was variant between 528 nm to 545 nm.